Flexible 3-Dimensional Hybrid ZnO Nanowire/a-Si:H Thin-Film Solar Cells

by

Minoli Pathirane

A thesis
presented to the University of Waterloo
in fulfillment of the
thesis requirement for the degree of
Doctor of Philosophy
in
Electrical and Computer Engineering

Waterloo, Ontario, Canada, 2016

AUTHOR'S DECLARATION

I hereby declare that I am the sole author of this thesis. This is a true copy of the thesis, including any required final revisions, as accepted by my examiners.

I understand that my thesis may be made electronically available to the public.

Abstract

ZnO nanowires were conformally coated with hydrogenated amorphous Si (a-Si:H) p-i-n thin-film to form three-dimensional (3-D) radial-junction (RJ) nanowire solar cell arrays (NWSCs). These NWSCs are a promising architecture for photovoltaic devices due to their enhanced light absorption and carrier extraction capabilities. However, conformally coating thin-films and the top electrode over ZnO nanowires become difficult with decreased periods by using conventional methods. In this thesis, conformal coatings were achieved by increasing the average spacing between NWSCs while effectively moving the NWSCs physically towards each other via substrate-bending to change the spacing between the NWSCs. Randomly positioned NWSCs were fabricated directly on flexible substrates at < 200ºC. 2 μm/200 nm/2×10^{-8} cm^{-2} height/diameter/density ZnO nanowires were grown hydrothermally on polyethylene naphthalate substrates using a ZnO nanoparticle seed layer. P-i-n a-Si:H thin-film were subsequently deposited over the ZnO nanowires using plasma-enhanced chemical vapor deposition. Finally, a composite layer, composed of Al-doped ZnO thin-film and Ag nanowires, was coated over the 3-D structures to form flexible, conformal, and transparent top electrodes.

A 100% yield of flexible NWSCs about a 3-inch diameter substrate was achieved with highest power conversion efficiencies of 5.5 ± 1%. Mechanically bending the NWSCs concave-up to a radius of curvature of 38 mm decreased the NWSC spacing by 9%, which helped further enhance light absorption by 13% and ΔJ_{SC} by 11% from the cells. Geometric and numerical models were used to assess the effective movement of the NWSCs and mechanical strain when the substrate was bent concave-up and concave-down (away from the incoming light). Stress-induced strain due to the mechanical bending was calculated to be ~ 0.1-1%. Furthermore, a polydimethylsiloxane film coated conformally over these 3-D nanostructures produced effective super-hydrophobic surfaces, which can help maintain clean NWSC arrayed top surfaces without degrading the 3-D device performance.

Acknowledgements

I am extremely grateful to my advisor, Professor William S. Wong, who has over the years become a mentor and friend to me. His vision and belief in me has been invaluable to my success. Thank you so much for all the opportunities you've granted me, Professor Wong. I am also grateful to Professors Irene A. Goldthorpe, Hany Aziz, John Wen, and my external committee member, Professor David Janes for all of your support and encouragement to help me succeed in my research.

Thank you so much to Dr. Czang-Ho Lee and Dr. Michael M. Adachi for being wonderful mentors and trusted friends; I am grateful for having your guidance along the way. Special thanks to Professors Siva Sivoththaman, Bo Cui, Chettypalam Selvakumar, and Andrei Sazonov for their continued mentoring and support. I would like to extend a big thank you to Professor Ting Tsui for entrusting me with a senior position on his FE-SEM system; one that permitted me to use the system frequently and train many new users. Thank you also to Mr. Richard Barber for entrusting me with many key responsibilities in the G2N laboratory.

Thank you to the wonderful colleagues whom I've met along the way for all the numerous intellectual discussions and for many special memories made during my time in graduate school. The collaborations that I had with Dr. Vladislav Jovanov, Professor Dietmar Knipp and his team with generating numerical simulations of my device structures are greatly appreciated. Many thanks to Professor Kai Wang and my colleagues from the Giga-to-nanoelectronics laboratory and the Energy Research Center for the technical support. Special thanks to everyone in the AFET group – your support throughout these past five years has been instrumental to my success.

Last and most importantly, I am indebted to my loving grandpa, Mama, Dada, sister, and Eranga for being the pillars of my success. I am truly grateful to my sister for being the main force behind my motivation for pursuing this PhD work. This dissertation is a tribute to them.

Dedication

This thesis is dedicated from the bottom of my heart to my grandpa, Mama, Dada, sister, Eranga, and little Achelle for always believing in me.

Table of Contents

List of Figures

List of Tables

List of Acronyms

Materials:

a-Si:H: hydrogenated amorphous silicon
AZO: Al-doped ZnO
c-Si: crystalline silicon
Cr: Chromium
HCl: hydrochloric acid
HMTA: hexamethylenetetramine
ITO: indium tin oxide
nc-Si:H: hydrogenated nanocrystalline silicon
NP: nanoparticle
NW: nanowire
NWSC: nanowire solar cell
PDMS: polydimethylsiloxane
PEN: polyethylene naphthalate
PET: polyethylene terephthalate
p-n: p-type/n-type junction
p-i-n: p-type/intrinsic/n-type junction
Si: silicon
SiNW: silicon nanowire
SiN_x: silicon nitride
SiO_x: silicon oxide
SnO_2: tin oxide
TCO: transparent conductive oxide
TiO_x: titanium oxide
ZnO: zinc oxide

Characterization:

ADSA: axisymmetric droplet shape analysis/analyzer
AFM: atomic force microscopy/microscope
AM: air mass
EDX: energy dispersive x-ray spectroscopy
EQE: external quantum efficiency
FTIR: Fourier transform Infrared spectroscopy
SEM: scanning electron microscopy
UV-vis: ultraviolet-visible spectroscopy

Processing:

ALD: atomic layer deposition
CVD: chemical vapor deposition
PECVD: plasma enhanced chemical vapor deposition
RIE: reactive ion etching
RF: radio frequency
VLS: vapor-liquid-solid

Material/Device parameters:

CTE: coefficient of thermal expansion
d: diameter
FF: fill-factor
h: height
J_d: dark current-density in the dark
J_{ph}: photocurrent density in the diode
J_{SC}: short-circuit current density
L_{diff}: Minority carrier diffusion length
L_{drift}: Minority carrier drift length
LRO: long range order
p: period/pitch
PCE: power conversion efficiency
P_{max}: maximum power
RF: roughness factor
R_S: series resistance
R_{SH}: shunt resistance
SCR: space charge region
SRO: short range order
t: p-i-n thickness
$t_{electrical}$: electrical thickness
T_m: melting temperature
$t_{optical}$: optical thickness
V_{OC}: open-circuit voltage

Chapter 1

Introduction

1.1 Thin-film Flexible Solar Cells

Solar energy is a key source of energy that could help achieve demanding energy requirements of an ever increasing human population. Currently, sunshine produces 10,000 times more energy than the daily world's energy consumption needs [1]. Solar cell devices or photovoltaics can convert these incoming photons directly to electricity; research focused in such devices has never been more critical as it is now.

A growing field in photovoltaics has been for niche applications such as consumer electronics, biomedical applications, as well as portable devices due to the dependable source of sunlight. One requirement of these applications is mechanical flexibility, which enables portability, durability, and their use in space-constrained areas, which in-turn would increase the applicability of the devices. To achieve these requirements, thin-film flexible, rollable, and foldable solar cells have been fabricated on flexible and low-melting point plastic and steel foil. However, power conversion efficiencies (PCEs) less than 10% has resulted in limited exposure of the planar a-Si:H thin-film flexible cells on the market thus far. Therefore, improving the performance of such thin-film flexible solar cells is critical to ensure the devices become a competitive alternative power source.

Thus far, highest PCEs achieved in-laboratory for mono-crystalline silicon (c-Si) solar cell devices have been ~ 20 – 25.6%. Reasons for why such cells currently dominate the market for solar cell technology is because Si is abundant in nature (Si can be obtained from sand), can readily form silicon dioxide dielectric films through thermal oxidation, and is a mature material in the microelectronics industry for the fabrication of a vast number of electronic applications. Despite these advantages, c-Si devices fall into the realm of first generation solar cells due to their increased cost of production relative to other solar cell devices fabricated today. Figure 1 presents the cost of production for rigid solar modules as a function of their achievable power efficiencies [2]. The figure indicates that compared to the other generation types of solar cells, c-Si solar cells are the most costly with 4× lower maximum potential device efficiencies. Furthermore, the need for a high thermal budget to fabricate c-Si solar cells disqualifies their fabrication on low melting-point flexible substrates such as plastic. One solution to this problem has been in thinning bulk c-Si to fabricate flexible and lightweight solar cells; however, the high material waste by etching crystalline films and the associated complexity in processing deem the fabrication process inefficient. Thus, the quest to fabricate more efficient flexible solar cells is ongoing.

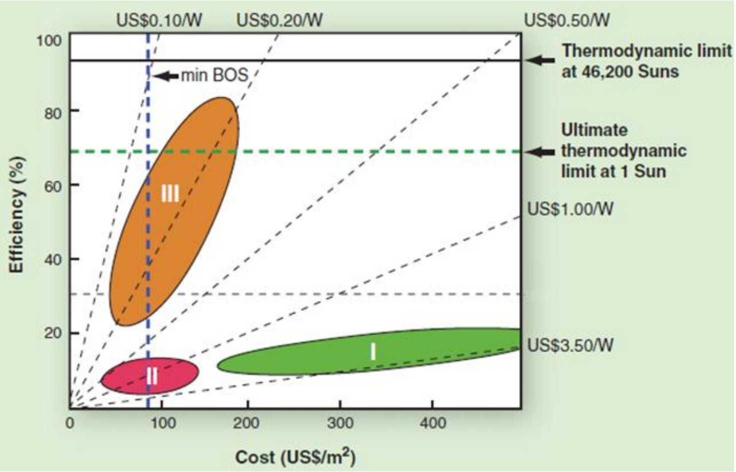

Figure 1. Solar energy efficiency as a function of production costs for a solar module of generations 1, 2, and 3 [2]**.**

Hydrogenated amorphous Si (a-Si:H) thin-film (or planar) solar cells are second generation photovoltaics, which have gained considerable interest due to their relative lower costs of solar cell production than c-Si solar cells and maturity in the microelectronics industry. Additionally, their thin-film usage and low-temperature fabrication process allow for the fabrication of the thin-film solar cells on low melting-point flexible plastic substrates. Furthermore, unlike c-Si, the film consists of a direct bandgap, which only requires the absorption of a photon for charge generation and thus, possesses a greater absorption coefficient than the former material. A-Si:H is also very uniform – ideal for solar cells to ensure consistency in electrical characteristics for batch production. This uniformity, however, stems from the material's high disorder in the atomic scale – unlike c-Si, a-Si:H lacks in crystalline periodicity, and thus, long-range order (LRO) does not exist in the material. The disorder of the atomic structure promotes a greater defect density, which increases the probability of recombination of carriers in the material. Furthermore, the carriers in the film rely on a hopping mechanism for charge transport to occur. Thus, to better manage charge collection, a-Si:H thin-film solar cells limit the film thickness to only 300 nm – 500 nm. However, using such a thin layer in-turn hinders the amount of optical absorption within the cell. These limitations of the a-Si:H thin-film have resulted in planar solar cell PCEs of < 5% on plastic substrates. To push the limits of solar cells of both c-Si and a-Si:H, novel geometries have been explored of which, 3-dimensional (3-D) structures such as radial-junction (RJ) nanowire array solar cells (NWSCs) have garnered significant interest.

1.2 Flexible 3-D Radial-Junction Nanowire Solar Cells

3-D nanowire structures [3]–[7] are a promising architecture for enhancing device performance through electrical [8], [9] and optical [10]–[14] manipulation in energy harvesting solar cells. The increased surface area in a third-generation NWSC array increases the chances of efficiently absorbing incident light while the increased junction area of individual NWSCs helps collect more charge carriers that are generated in the cell. Furthermore, increasing the nanowire densities typically results in improved light scattering with enhanced optical absorption [15], [16] but, continuous conformal thin-film coverage is difficult due to shadowing effects from the non-planar 3-D nanowire structures. Two main methods of fabricating radial-junction periodic and randomly positioned or "disordered” nanowires exist: (1) top-down [6], [8], [17]–[21] and (2) bottom-up [13], [15], [22]–[26] nanowire growth. Hitherto however, the top-down fabrication approach has not been used to fabricate NWSCs directly on flexible substrates due to the difficulty synthesizing vertical nanowire arrays of uniform dimensions on a flexible substrate of high curvature. Instead, the top-down approach has been used to synthesize flexible NWSCs through a two-step process, which includes (1) fabrication of the nanowires on rigid substrates followed by (2) encapsulating the top of the nanowire array with a thick polymer coating such as poly-di-methyl-siloxane (PDMS). Finally, the rigid substrate is removed through chemical-mechanical polishing (CMP) [27], making this process complex and expensive for third generation solar cells.

Bottom-up techniques have been used for similar two-step fabrication processes. One such method to fabricate NWSCs on a flexible substrate had been by (1) fabricating the nanowires on rigid substrates through a vapour-liquid-solid (VLS) technique followed by (2) sonication of the nanowires to disperse them in solution, from which the wires were drop-casted or spin-coated onto the flexible substrate [28]. The process however, results in nanowires dispersed horizontally on the flexible substrate. Another approach to develop vertical NWSCs on flexible substrates has been to encapsulate the top of the nanowire array with a ~3 mm thick elastomeric coating such as PDMS after fabricating the wires through a bottom-up VLS growth technique followed by peeling the PDMS layer off the substrate [20], [29], [30]. Optionally, another layer of PDMS can be coated on the back side of the nanowire array to form a flexible PDMS substrate [17].

As described from these experimental techniques, the two-step transfer process is a popular technique for nanowire device fabrication on flexible substrates. The method however, has a high risk that the nanowires will break during the transfer process [20]. To minimize disintegration of the nanowires, an approach to directly fabricate the 3-D devices on flexible substrates is needed while realizing superior power conversion efficiencies that a radial-junction nanowire array could generate over a thin-film planar solar cell. To enhance the power conversion efficiency of a radial-junction NWSC, increasing the lengths and densities of the nanowires have been assessed as methods to further increase the junction area and thereby, increase the total PCE of a solar cell [31].

Increasing the nanowire aspect ratio and reducing the separation between each wire by increasing the nanowire density have enhanced the optical absorption within the array [11], [31], [32] that would result in an increased carrier generation in the solar cell. Tamang *et al.* have predicted that the current density of a 3-D hybrid ZnO nanowire/a-Si:H p-i-n nanowire array can increase by more than 2× compared to a planar p-i-n a-Si:H solar cell by decreasing the separation distance between nanowires to 600 nm (i.e. by increasing the NWSC density). However, fabricated nanowire arrays of large aspect ratios (> 1.5) and increased densities ($> 10^8$ cm^{-2}) have led to poor electrical performance because conformal deposition of subsequent thin-film layers and formation of the top electrode around each nanowire within the array becomes increasingly difficult. The effect worsens if the nanowires are randomly positioned and tilted to the substrate (i.e. disordered) because the neighbouring nanowires would shadow each other, resulting in areas of poor film coverage over the wires [33].

1.3 Top Electrode Formation and Nanowire Density Control

To minimize the imperfections in depositing the p-i-n thin-film and forming the top electrode on the nanowires, the optimum nanowire density and aspect ratio are restricted to lower densities of $\sim 2\times10^8$ cm^{-2} and ~ 2, respectively. This restriction however limits the point at which light absorption is maximized. Therefore, a practical solution that would help further enhance light absorption while enabling conformal thin-film and top electrode deposition is needed to further improve the optical and electrical device performance of the NWSCs.

This PhD dissertation explores the optical and electrical characteristics of flexible 3-D NWSCs that are fabricated using a hybrid structure consisting of a-Si:H thin-film and ZnO nanowires, which are grown directly on low melting-point flexible poly-ethylene naphthalate (PEN) substrates to enable a simpler fabrication process and greater yield of functional NWSCs compared to the two-step fabrication process discussed in the previous section. Also, a separate approach to change the nanowire density is explored by mechanically bending the flexible substrate concave-up and concave-down. By bending the PEN substrate, the position of the individual nanowires may be manipulated to increase the effective density of nanowires in the array and enhance the optical absorption of the NWSC array. With an increase in optical absorption, the electrical characteristics would also be enhanced. This alternative approach would ease fabrication of the devices by allowing the nanowires to be more dispersed during processing of the 3-D devices, enabling easier conformal deposition of the thin-films and top electrode over each nanowire. In turn, the nanowires would effectively move freely when the substrate bends, and thus, the flexible devices would possess another advantageous role for solar cell applications.

A few groups have reported on the two-step approach of fabricating nanowire structures on flexible platforms [34], [35] in order to enhance the performance of solar cell devices . Kim *et al.* demonstrated enhanced optical absorption with very high-density nanowire structures (> 10^{-9} cm^{-2}) embedded in a polymeric matrix over planar solar cells; however, they reported only 0.5%

change in the optical characteristics when flexed [30]. Fan *et al.* also demonstrated radial-junction single-crystalline nanopillars encapsulated in polydimethylsiloxane (PDMS) but, observed only marginal changes in the electrical characteristics when the PDMS structure was flexed [17]. This PhD dissertation further explores this concept by using randomly positioned and randomly tilted (herein called disordered) 3-D nanowire structures, which were grown *directly* onto flexible PEN substrates and were mechanically bent. The effect of the NWSC motion on the optical and I-V characteristics was studied and compared to reference flexible planar a-Si:H p-i-n solar cells.

The 3-D structured surface were further exploited to enhance their device functionality. Methods to integrate an additional self-cleaning surface on the solar cells were investigated to mitigate accumulation of dust particles and other debris that could block incoming sun-light to the cells and thereby, create a multi-functional 3-D solar cell.

1.3.1 Summary of Flexible Nanowire and NWSC Arrays Published in the Literature

Table 1 summarizes inorganic nanowire and NWSC array characteristics that were fabricated on flexible substrates by other groups in the pursuit of fabricating flexible 3-D NWSC arrays. The table presents the growth characteristics and electrical characteristics of the NWSC arrays fabricated by each author. Under growth characteristics, the nanowire growth method and substrate used are indicated along with the type of nanowires synthesized and their average dimensions. These characteristics affect the corresponding electrical characteristics achieved from the NWSCs.

Table 1. Published reports of inorganic nanowire arrays fabricated on flexible substrates.

		Growth Characteristics			*Electrical Characteristics*			
Year	**Lead Author and Reference**	**NW Growth Method**	**NW Type**	**NW Height/ Diameter [nm/nm]**	**J_{SC} [mA/cm^2]**	**V_{OC} [mV]**	**FF [%]**	**PCE [%]**
2008	RR LaPierre [34]	Bottom-up on CNT film, 1S	GaAs	~ 2 µm/ 20 – 200 nm	-	-	-	**-**
2009	A. Javey [17]	Top-down on PDMS, 2S	CdS/CdTe	~ 2 µm/ 200 nm	21	620	43	**6**
2009	H Atwater, KE Plass [38]	Bottom-up on PDMS, 2S	c-Si	~ 100 µm/ 1.5 – 2 µm	-	-	-	**-**
2010	H. Atwater, N. Lewis [29]	Top-down on PDMS, 2S	c-Si	80 µm/ 1.5 µm	9.6 *(at 80 mWcm^{-2})*	402	35	**1.35**
2010	MM Adachi[39]	Bottom-up stainless steel, 1S	c-Si	~ 1.2 µm/40 nm	-	-	-	**-**
2010	MK Kim [30]	Bottom-up on PDMS, 2S	ZnO	6 µm/ -	-	-	-	**-**
2010	S. Zhang [37]	Top-down on PDMS, 2S	ZnO	5 µm/ 1 µm	-	-	-	**-**
2011	H Atwater, D. Turner-Evans [36]	Top-down on PDMS, 2S	c-Si	15 µm/ ~ 6 µm	~ 10	~505	55	**2.51**
2011	KT Park [21]	Top-down on PDMS, 2S	c-Si	50 µm/ 2 µm	-	-	-	**-**
2012	AJ Standing [40]	Top-down on PDMS, 2S	GaP, InP	10 µm/ 1.5 – 2 µm	-	-	-	**-**
2012	X. Xie [41]	Bottom-up stainless steel, 1S	c-Si	~ 3 µm/ 50 – 200 nm	13.36	370	30	**1.48**
2013	X. Xie [42]	Bottom-up stainless steel, 1S	c-Si	~ 2 µm/ 600 nm*	13.36	620	43	**3.57**

1S: Direct fabrication on flexible substrate
2S: Two-step process to transfer nanowires on flexible substrate
**: Results obtained from scanning electron microscope images published*

As shown in Table 1, the highest PCEs achieved have been for top-down synthesized flexible NWSC arrays using CdS/CdTe. The FFs obtained from the 3-D devices from the two-step process were less than 60%, resulting in average PCEs of ~ 2.8%. An alternative fabrication approach that would generate greater electrical characteristics from flexible NWSC arrays is thus explored.

1.4 PhD Research Goal

The main goal of this PhD research is to understand the optical and electrical characteristics of the 3-D NWSCs fabricated directly on flexible substrates and find ways to further improve their device performance. By achieving this goal, the research conducted strives to fabricate a high performance flexible NWSC that takes advantage of the nanostructure beyond its optical and electrical properties with self-cleaning characteristics.

The following approaches are used to achieve this goal:

I. The direct fabrication and characterization of hybrid NWSCs on low-cost flexible plastic media using a low-temperature and scalable process

II. Demonstration of a flexible, conformal, and transparent top electrode on the 3-D NWSCs

III. Experimentally flexing the fabricated solar cells to assess the optical and electrical effects from planar and NWSC devices

IV. Analytical and numerical modeling of the strain induced to the NWSCs upon mechanical bending

V. Extending NWSC functionality by exploiting its 3-D surface to create self-cleaning super-hydrophobic properties

1.5 Thesis Structure

This PhD dissertation is organized as follows:

The background discussion in Chapter 1 explains the motivation for this PhD work and the approaches taken to reach the research goals therein. Chapter 2 provides a background review of the operation of planar and 3-D solar cells followed by a literature review about the growth techniques for NWSCs including hybrid ZnO nanowire/a-Si:H thin-film solar cells and the device performance of the latter through numerical simulations and analysis. Random growth of ZnO nanowires and thin-film materials characterization are provided in Chapters 3 and 4, respectively. These materials were used to fabricate p-i-n a-Si:H thin-film solar cells as reference devices and hybrid disordered NWSCs, whose optical and electrical characteristics are further analyzed in Chapter 5. Fabrication issues related to poor top contact electrodes are described later in this chapter. An ITO nanoparticle suspended in ethanol was initially used to improve the contact of the top electrode on the disordered NWSC array and further improvements were made by incorporating Ag nanowires (Ag NWs), which is discussed in Chapter 6. Chapter 7 discusses the electrical performance of the modified top contacts when they are mechanically strained. The fabricated planar and NWSCs are subsequently mechanically bent to further enhance the optical properties in the array (by bending the substrate concave-up towards the incident light, effectively increasing the NWSC density and improving the electrical characteristics. The strain induced to the NWSCs and planar solar cells during bending are modeled using COMSOL Multiphysics (ver 5.2) to determine the induced strain and range of motion in the nanowires during bending. Finally, methods to produce super-hydrophobic surfaces on the NWSCs by surface modulation of the nano-structured surface are investigated in Chapter 8. The thesis concludes with the contributions and future outlook of this PhD research in Chapter 9.

Chapter 2

Background Review

2.1 Operation of a Thin-Film Amorphous Silicon Solar Cell

The foundation of a solar cell is a photodiode. In contrast to a c-Si solar cell, which consists of a p-n junction, an a-Si:H solar cell consists of a p-i-n junction. The p-layer is highly doped with boron atoms (acceptor atoms) while the n-layer is doped with phosphine atoms (donor atoms) [43]. Doping the thin-film creates a p-layer (n-layer) constituted of majority hole (electron) carriers. The doped layers also consist of very high defect densities, which greatly limit the minority carrier lifetimes. Thus, an intrinsic layer (i-layer) of a lower defect density is sandwiched between the p- and n-layers, enabling generated electron-hole pairs to transport through a less defective film. A built-in electric field would ideally span the entire i-layer and facilitate extraction of the generated carriers in the region, which is called the space charge region (SCR). This SCR is a key component in a solar cell because, both optical absorption and carrier separation occurs here.

When light irradiates on the diode, photon energy that is larger than the bandgap of the material promotes an electron from the valence band (E_V) to the conduction band (E_C), creating an electron-hole pair, which will move to their respective n- (for electron) or p-side (for hole) by the electric field in the SCR for charge collection. Thus, light that shines on the diode increases the current supplied to an external load (R_{load}) as indicated in the current density-voltage (J-V) curve on Figure 2 (a). Figure 2 (b) shows the equivalent circuit model of a realistic solar cell, taking into account its series resistance (R_{series}) and shunt resistance (R_{shunt}). Physically, R_{series} in a solar cell can be due to the resistance in each of the a-Si:H thin-films within the diode, contact resistance between the metal electrodes and the a-Si:H, as well as the resistance from each of the electrodes. R_{shunt} in a solar cell is primarily due to defects within the a-Si:H film that form alternate pathways from the p-layer to the n-layer for photo-generated charge carriers in the solar cell. This effect reduces the total photocurrent collected from the solar cell, resulting in power losses.

The solar cell may be characterized by its open-circuit voltage (V_{OC}), short-circuit current density (J_{SC}), fill-factor (FF), and power conversion efficiency (PCE). The V_{OC} is the maximum voltage in a solar cell that would arise when the terminals of the device are disconnected while the J_{SC} is the maximum current generated in a solar cell at 0 V. The FF can be found using the maximum power ($P_{MAX} = J_{MAX} \times V_{MAX}$) supplied by the diode as,

$$FF\ [\%] = \frac{P_{MAX}}{J_{SC} \times V_{OC}}. \qquad (1)$$

As suggested from Equation (1), the FF is a percentile indicator of the ideal ‘square’ shape of the I-V curve during illumination of the solar cell; a high FF indicates low R_{series} and high R_{shunt} in the cell. The R_{series} and R_{shunt} can be found through two ways: (1) by taking the slope of the J-V characteristics in light near V_{OC} and J_{SC} for R_{shunt} and R_{series}, respectively, or (2) by taking the slope near 0 V for R_{shunt} and near V_{OC} for R_{series} from the semi-log (J)-V plot in the dark. The slope between these two resistances in the semi-log (J)-V plot denotes the ideality factor, *n*, which is a factor typically ~ 1 – 2 that indicates the amount of recombination in the diode. A lower (greater) amount of recombination within the diode would lead to *n* values nearing 1 (2). All of these solar cell parameters affect the PCE, which is given as,

$$PCE = \frac{J_{SC} \times V_{OC} \times FF}{I}, \qquad (2)$$

where I is the total spectral illumination of one sun of $100\,\frac{\text{mW}}{\text{cm}^2}$ at air mass (AM) 1.5G. This solar spectrum is analogous to light illuminated on the surface of the Earth after it has travelled an average distance through the Earth's atmosphere of 1.5 atmosphere thicknesses

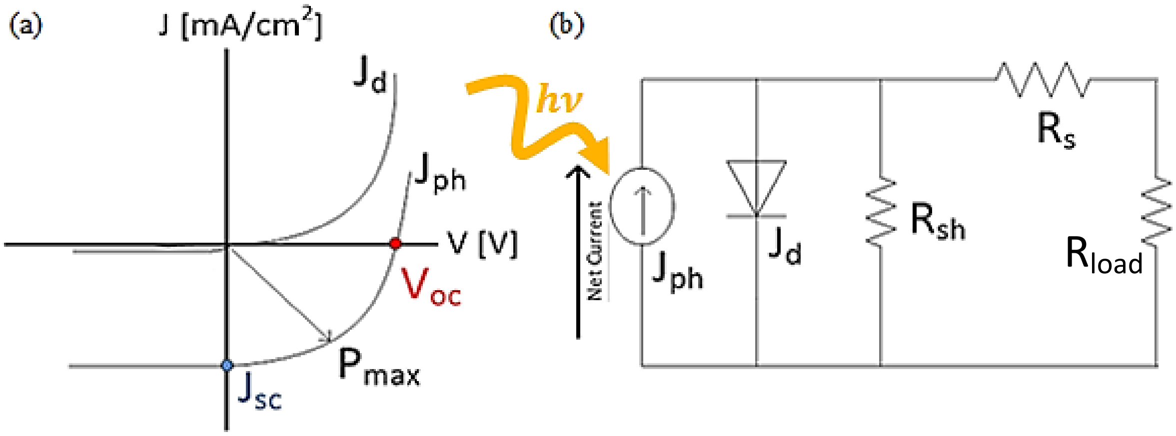

Figure 2. (a) Dark (J_d) and photo (J_{ph}) J-V curves and (b) equivalent circuit model of a solar cell.

A-Si:H p-i-n diodes are drift-based. This process of light absorption to charge collection can be reduced to three main categories and is shown in an energy band diagram in Figure 3 for an a-Si:H p-i-n solar cell:

I. A photon enters the cell through the top transparent contact

II. The photon is absorbed, creating an electron-hole pair, provided the photon energy is greater than that of the semiconductor bandgap of the absorber layer

III. The electron (hole) carrier drifts toward the n (p) side for collection

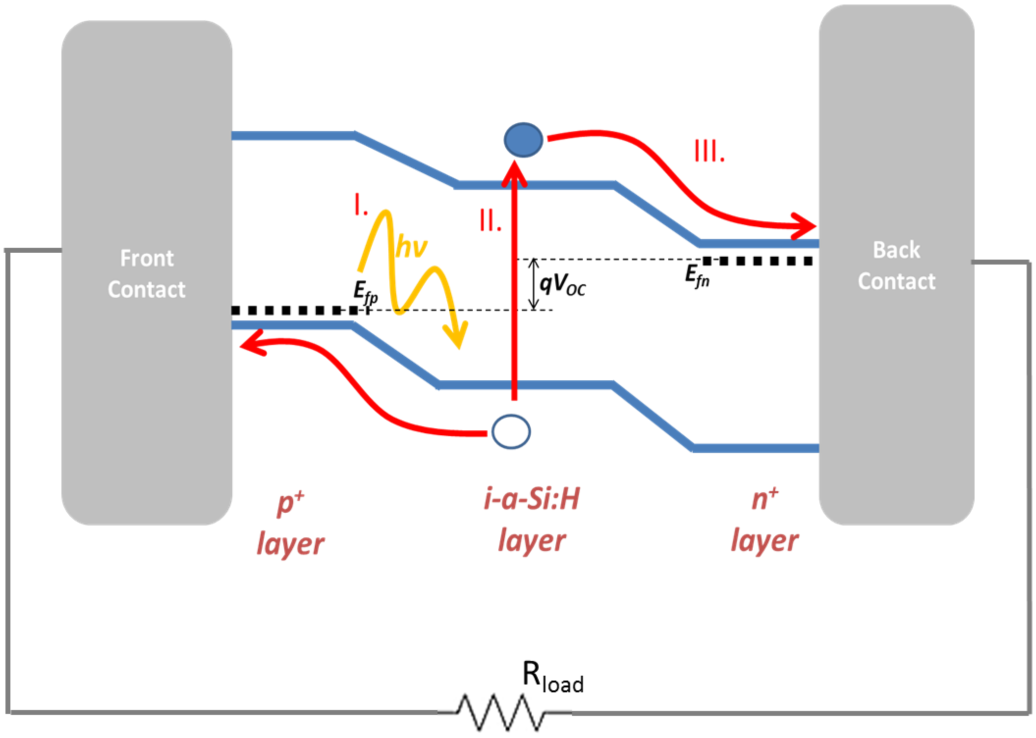

Figure 3. Energy band diagram of a p-i-n solar cell device under solar illumination. The incident photon is absorbed in the i-layer where the SCR exists, forcing the charge carriers to split and travel to their respective majority-carrier thin-film layers of the solar cell.

Today, c-Si solar cells produce a stabilized PCE of 20% [2], [3] while thin-film a-Si:H solar cells can produce PCEs of 6% [4]. The reason behind greater PCEs for c-Si bulk solar cells compared to a-Si:H devices is in the former material's crystalline long-range order (LRO), which enables greater minority carrier lifetimes than in the latter material. Figure 4 (a) illustrates the periodic crystalline network of c-Si where each Si atom (in black) is covalently bonded to another Si atom in the film. Figure 4 (b) illustrates the energy band-diagram of c-Si and its indirect bandgap of 1.12 eV. The LRO of c-Si allows for the use of much thicker films (200 µm for c-Si vs. 300 nm for a-Si:H) in c-Si solar cells to ensure that it would absorb 99% of the incident sunlight. However, the cells require high temperature fabrication processes (~ 950ºC) and refining processes (to at least 99.9999% purity) [44]. All these factors result in a complex fabrication process with limited ability to produce flexible devices.

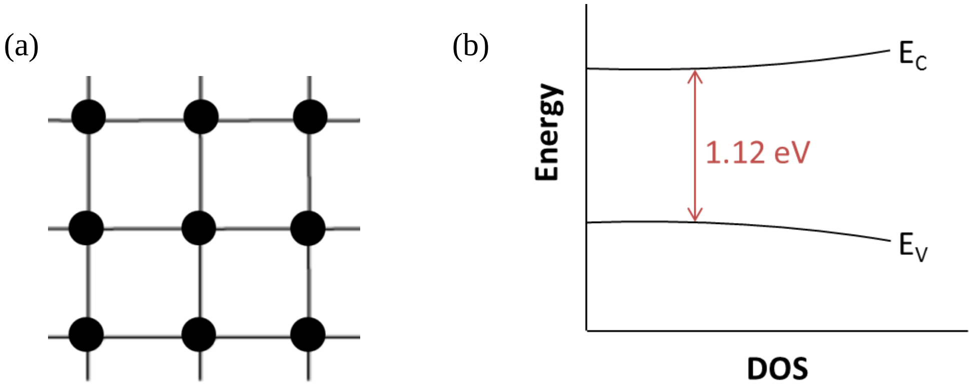

Figure 4. Illustration of the (a) LRO periodic structure of a c-Si film and (b) its equivalent energy band structure.

A-Si:H on the other hand, is a promising material for electronic devices, allowing for a relatively low-cost, low-temperature, and uniform deposition of the film for large-area device applications. Such films can be fabricated at temperatures of less than 300ºC, enabling direct fabrication of the devices on inexpensive arbitrary substrates, which may enhance device functionality. The direct optical bandgap of 1.75 eV of a-Si:H and its increased absorption coefficient compared to c-Si, further empowers more efficient absorption of light, with an absorption depth of 1 μm for 99% of the visible light. These characteristics enable the fabrication of solar cells of increased device functionality such as flexibility.

Although increasing the thickness of the intrinsic a-Si:H can serve to absorb more photons, carriers generated this way are likely to be inefficiently collected in the solar cell as the increased thickness results in increased defects and greater chances of recombination, contributing to a poor electric field within the i-layer. Since a-Si:H is disordered and consists of strained Si-Si covalent bonds, which in the worst case, may break apart, forming localized defect states such as dangling bonds (Figure 5 (a)), charge carriers may easily trap and undergo non-radiative recombination in these locations. Although diffusion of hydrogen may occur during a-Si:H deposition in order to reduce the density of dangling bonds in the film, it is difficult to ensure all of such dangling bonds passivate with hydrogen. The defect density further increases as the deposition temperatures are lowered since the thermal energy may be insufficient to overcome the activation energy needed for Si-H bonding to occur [45]. The band diagram of a-Si:H includes mid-gap defect states, illustrating the density of the dangling bonds in the film. Also, band tails occur near the edges of E_C and E_V due to the strained Si-Si bonds in the film (Figure 5 (b)). These disadvantages in a-Si:H at low temperatures necessitate alternative methods to overcome the challenges; one such method is to change the 2-D device structure into a 3-D cylindrical shape, much like a nanowire in order to improve the optical and electrical characteristics of the solar cell.

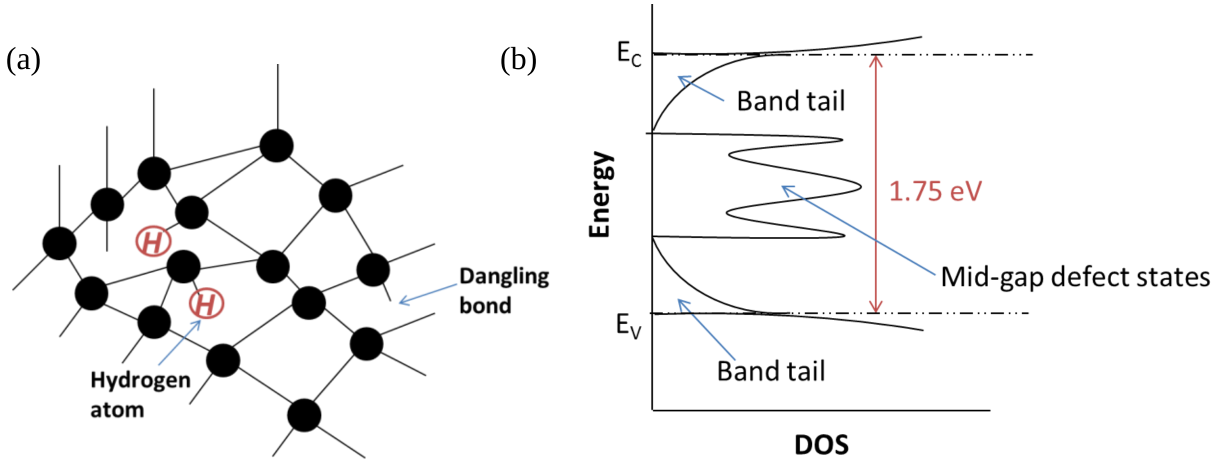

Figure 5. (a) Film structure of a-Si:H and (b) its corresponding band diagram.

2.2 Radial-Junction Nanowire Solar Cell Operation

In a radial-junction NWSC, the optical and electrical characteristics of the cell are decoupled. The SCR exists at the p-n junction or in the i-layer of a p-i-n junction, which surround the nanowire (Figure 6). Thus, the junction area is increased from which a generated minority carrier can more easily sweep through to its contact regardless of where it is generated in the cell, resulting in efficient charge collection. Because of the efficient generation of carriers, increasing the i-layer thickness is no longer required, and in-turn enables the SCR to span the entire i-layer.

Furthermore, light absorption occurs along the axial length of the NWSC. Incorporating an array of such NWSCs could lead to increasing light scattering within the 3-D structures; this would help absorb more light in the array and limit the fraction reflected back to atmosphere [46]. Thus, unlike a 2-D thin-film solar cell where an optimum thickness of the i-layer must be found to balance light absorption and carrier extraction, the NWSC increases the optical path length while decreasing the electrical transport length by means of its 3-D device structure.

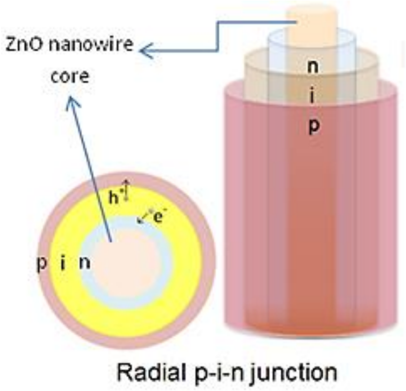

Figure 6. Illustration of a hybrid NWSC, in which the ZnO nanowire is conformally coated with p-i-n a-Si:H thin-film.

2.3 Nanowire Solar Cell Fabrication Processes

Nanowire synthesis can be categorized into two approaches called, top-down or bottom-up. Nanowires synthesized by the top-down approach are typically etched from a planar material [18], [19], [31], [47] while bottom-up nanowires typically grow from a nucleation layer [3], [4], [48], [49]. Sections 2.3.1 and 2.3.2 discuss both nanowire growth approaches to realize the advantages and limitations of these techniques for flexible NWSCs. Sections 2.3.2.1 and 2.3.2.2 discuss the bottom-up fabrication of hybrid ZnO nanowire/a-Si:H thin-film solar cells and their limitations, and numerical modeling of their device performances to assess their optical effectiveness in improving device performance, respectively.

2.3.1 Top-down Approach

Top-down procedures for nanowire synthesis have used a self-assembled nanoparticle (NP) array or patterned films of Ag [50], polystyrene beads [47], [51], or SiO_x [31], [52] that act as masks, which are formed by Langmuir-Blodgett [52], or e-beam lithography [18]. Figure 7 illustrates a reactive-ion-etch (RIE) plasma process used to selectively remove exposed regions and form a nanowire array. The area under the masks are not affected during the etch process while the areas that are exposed to the RIE plasma (or wet etchant) are removed. Depending on the mask pattern and dimension of each NP mask, the nanowire array formed underneath can be controlled in terms of the array periodicity and diameter, seeming to provide a direct way to control the nanowire array dimensions and density.

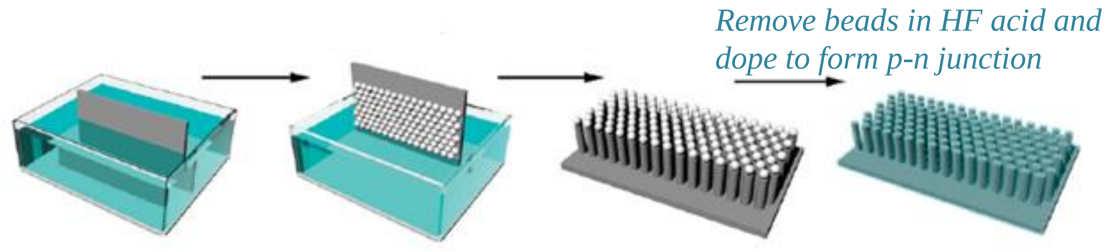

Figure 7. Langmuir-Blodgett top-down RIE process used to synthesize Si nanowires [31]**.**

However, the control of nanowire synthesis in this method is in fact limited. Specifically, some examples of limitations of this technique include uniformly etching nanowires of a specific aspect ratio over large areas (i.e. non-uniformity) [51], bunching of high-density nanowires [53]–[55], existence of residual impurities between nanowires from use of NPs [51] or photoresist used in e-beam lithography, scalability issues with the NPs on large area [51], and cost-effectiveness of expensive lithography processes. Moreover, Bao *et al.*'s numerical simulations have illustrated that the best scenario for light trapping is to incorporate nanowires with random diameter and lengths [56]. Fabrication of such structures at a large scale could be difficult to accomplish using the top-down approach. Furthermore, only rigid substrates (Si, glass) have been used in the top-down approach to date.

2.3.2 Bottom-up Approach

The growth of Si-based nanowires using the bottom-up approach has been demonstrated most commonly using the vapor-liquid-solid (VLS) mechanism [25], [26], [57], [58] where a catalyst, typically formed by sputtering a 2 – 5 nm thick metal film such as Au or a less deleterious element such as Cu [59] is used for nanowire growth on a Si substrate [3], [4]. Source gases are entered into the chemical vapor deposition (CVD) chamber and nanowire growth proceeds at temperatures typically > 850ºC [59]. Eventually, these Au nanoparticles would wet the nanowire sidewalls; thereby, consuming the nanoparticles and terminating nanowire growth.

Street *et al*. have shown that a disordered nanowire array grown using this approach can be useful for light trapping. Approximately 20 c-Si nanowires interact with a photon before being absorbed within a disordered array although, this scattering would decrease as the energy of the photon increases [13]. This optical interaction in the nanowire array improves the chances of successfully absorbing the photon. However, electrical characteristics of such disordered NWSCs have been very poor, achieving ~ 0.2% PCE as depicted in Figure 8 (a) and (b) [7].

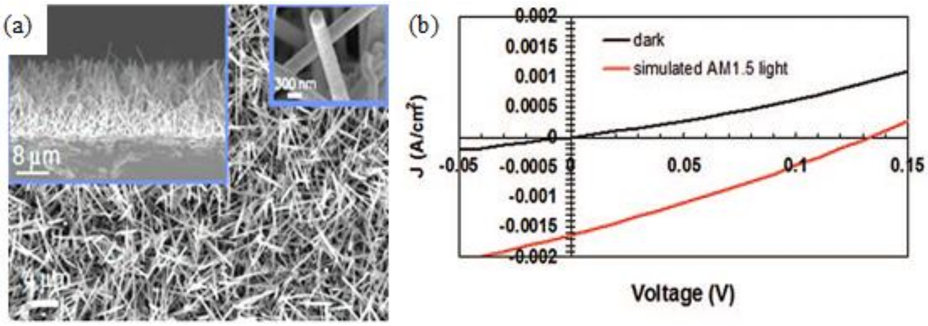

Figure 8. (a) SEM images of disordered Si wires (top right inset shows the Au catalyst tip) and (b) their I-V characteristics [7]**.**

One reason for poor solar cell performance in disordered NWSC arrays [7] is because the disordered nanowires are difficult to coat with thin-film to produce a conformal radial-junction and top electrode on each wire, resulting in poor J_{SC}, V_{OC}, and FF characteristics. High R_{series} is caused by poor deposition of the top contacts over the disordered NWSCs. Deposition of the TCO typically occurs via sputtering [25], [33], [60] but, sputtering is not a conformal deposition technique, which leads to patches of uncoated regions on the nanowire sidewalls. To mitigate the poor deposition of the top contact, a very thick shell is sometimes deposited (Figure 9) to ensure all regions of the nanowire are fully coated and would produce the required radial-junction and top electrode.

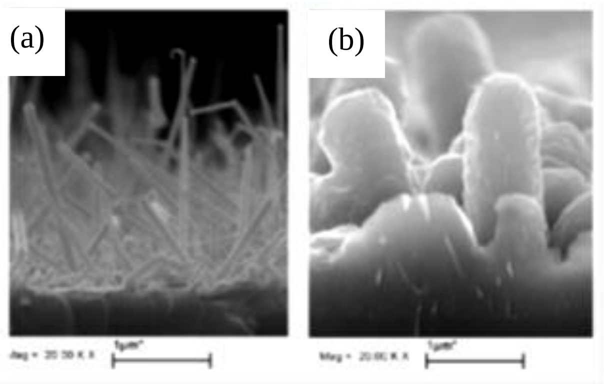

Figure 9. Cross-sectional SEM micrographs of (a) bare Si nanowires and (b) 3-D NWSCs after deposition of the thin-film [48]**.**

However, the NWSCs still suffer from degraded V_{OC} (< 300 mV) [3], [48], ideality factors, ($n > 2$), and low minority carrier diffusion lengths (L_{diff} < 20 nm) [61] due to interface impurities from the use of residual Au in the VLS growth. An acid treatment has been tested to remove the residue on the nanowires prior to device fabrication; yet, the impurities along the nanowire surface even after the acid treatment persist [48], [58], [59], [62]–[65]. In fact, Au atoms can diffuse 77 µm through the Si lattice during the growth stage and thereby, contaminate the entire nanowire structure [63]. Such metal impurities add deep-level trap states in the bandgap of the host semiconductor [66] and thereby, compromise the electronic properties of the semiconductor. This degradation is not only an issue with Au; impurities have been detected on nanowires grown with In [41], Sn [58], Ag [67], and Cu [59]. Therefore, a simpler and more effective method to fabricate NWSC arrays that would not cap the high performance expected from the 3-D devices would facilitate the affinity towards large-scale fabrication and widespread use of the devices.

2.3.2.1 Hybrid ZnO Nanowire/a-Si:H p-i-n Thin-film Solar Cell Arrays

A low temperature bottom-up growth approach that does not require a metal catalyst could eliminate many obstacles – specifically, the ability to grow disordered nanowires of random diameter and length to enhance light trapping, direct nanowire growth on arbitrary substrates, which includes flexible plastic, and evade use of impurity catalysts for minimum nanowire surface contamination are key factors to enhance device functionality and performance.

One approach to eliminate such obstacles is to coat a-Si:H p-i-n thin-film on ZnO nanowires to form a 3-D array of thin-film solar cells. To grow the ZnO nanowires, a low temperature hydrothermal approach can be used on a thin ZnO seed layer. This approach typically grows a high density of disordered nanowires. A hybrid ZnO nanowire/a-Si:H p-i-n thin-film solar cell has generated a PCE of 3.6% in the substrate orientation (Figure 10) [68] while the hybrid device structures used in superstrate configuration generated PCEs of 4.27% [69]. Although the authors term these devices “nanorod” solar cells, their SEM images show a more textured surface (Figure 10), far from the NWSC classification due to the employed low aspect ratios, which can in turn decrease light trapping in the solar cell. Furthermore, the cross-sectional SEM image (Figure 10 (c)) shows poor conformal coating of the a-Si:H p-i-n thin-film at the base of the nanowire array; these effects could lead to high R_{series} and shunting in the solar cell. These results were verified in this research, too; maximum PCEs of 4% (average PCE ~ 2%) were achieved with low yield due to low R_{shunt} and high R_{series} from the cells fabricated.

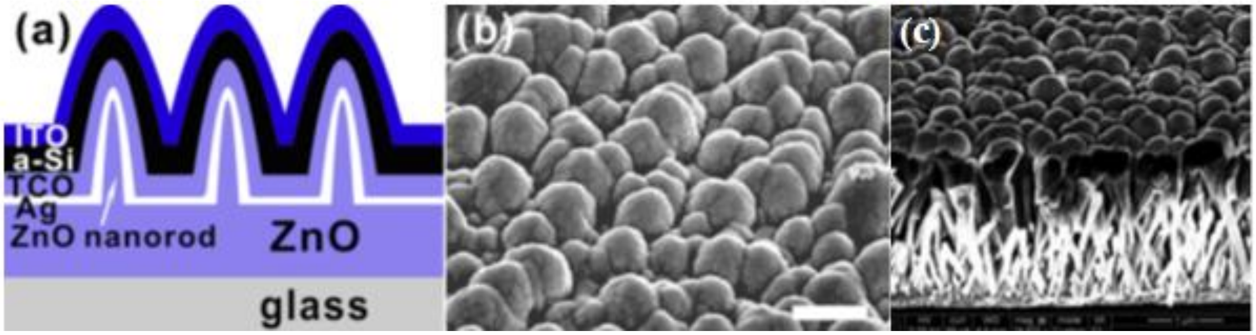

Figure 10. (a) Schematic diagram of fabricated hybrid NWSCs [68]**. (b) Tilted (scale bar: 500 nm)** [68] **and (c) cross-section** [70] **SEM micrographs of the fabricated hybrid NWSCs that incorporated high densities of ZnO nanowires, which were coated with a-Si:H thin-film.**

Thus, a method to deposit a-Si:H p-i-n thin-film conformally over ZnO nanowires is needed to form 3-D solar cells [69], [71]; this coverage depends mainly on the density of the ZnO nanowire array grown. As stated earlier, textured structures are obtained if the density of the nanowire array is too high with poor conformal coatings of the a-Si:H p-i-n thin-film. However, if the nanowire array is sparse enough, then the thin-film deposited over the grown nanowires would be more conformal to fabricate truly 3-D NWSC arrays. This approach had not been explored in the research community at the time of this research and therefore, is likely that the full potential of such hybrid nanowire structures for solar cells has not yet been realized.

Furthermore, the low-temperature fabrication process of the entire NWSC array deems suitable for flexible 3-D solar cell fabrication but, has not been reported yet. The combination of these factors could enable truly conformal hybrid ZnO nanowire/a-Si:H p-i-n thin-film NWSCs on flexible substrates with PCEs greater than 4.27%. To do so, the growth of the ZnO nanowire and the effects of nanowire height and period on overall performance are examined in the following section.

2.3.2.2 Numerical Simulations of Hybrid ZnO Nanowire/a-Si:H p-i-n Solar Cells

This work was a collaboration study with the Dr. D. Knipp, Dr. V. Jovanov, and Mr. A. Tamang who created optical simulations of the nanowire structures and helped analyze the results of the simulations.

An array of hybrid NWSCs allow for the optical characteristics of a solar cell to be enhanced by trapping the incoming light into the device without allowing much of the reflected light back out into the atmosphere. Cui *et al*. have stated that near-complete absorption of light can be achieved with wires that are microns long [1], which was confirmed by Kelzenberg *et al*. [8]. However, arrays of nanowires that are much shorter than that (< 2 µm) have still shown to achieve > 90% of light absorption in the visible spectrum where most of the energy in the solar spectrum exists [33]. With such optical enhancements to generate more charge carriers inside the NWSCs, a more efficient device may be achieved by using these shorter radial-junction hybrid 3-D structures.

This section provides details about the optical and electrical enhancements that could be expected from hybrid ZnO nanowire/a-Si:H thin-film solar cell arrays. To do so, both small- and large-sized periods between ZnO nanowire arrays that lead to textured and NWSC structures, respectively, were optically simulated from which, photocurrent characteristics were extracted. The optical simulations of light confinement in the nanowires were found by using a finite difference time domain (FDTD) algorithm to numerically solve Maxwell's partial differential equations of an incoming light ray. These simulations were performed by Tamang *et al.* from Jacobs University [32].

An array of nanowires could work together to effectively scatter light. By employing a high density of nanowires closely packed together (i.e. small-sized period), similar to that shown in Figure 10 (c), subsequent semiconductor films deposited would embed the nanowires within the films and thereby create a textured solar cell. The textured device would consist of a period, p, as defined in Figure 11, between nanowires of less than that of the p-i-n semiconductor film thickness, t, together with the nanowire diameter, d, as provided in the following expression:

$$p \leq 2t + d. \qquad (3)$$

Figure 11 shows a schematic diagram of a textured solar cell with these parameters labeled.

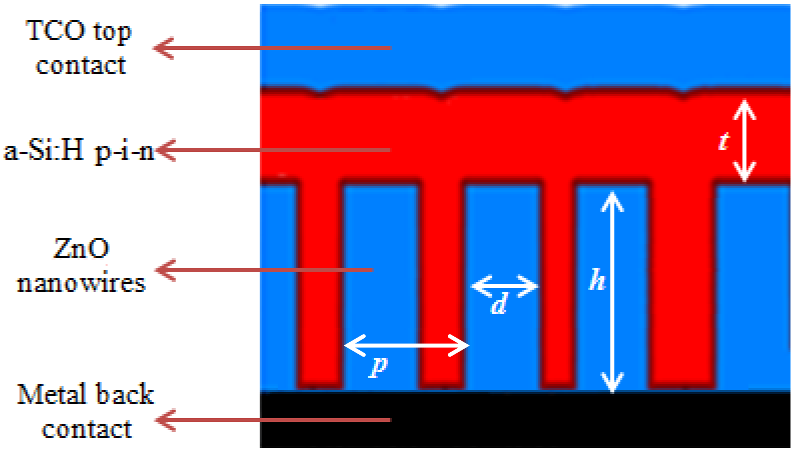

Figure 11. Schematic diagram of hybrid ZnO nanowire/a-Si:H thin-film textured solar cell [32]**.**

In this case, the nanowires are encased in an a-Si:H p-i-n thin-film layer that planarizes the 3-D nanowire structure. Because of this planarization, the minority carrier transport length is longer than a nanowire solar cell and thus, the cell acts essentially as a planar device. The structure limits its absorption of light to only long wavelengths of light due to the embedded nanowires at the bottom of the solar cell, and thereby possesses a limited optical pathway, $t_{optical} \approx t_i$, where t_i is the average thickness of the intrinsic a-Si:H film. Furthermore, the maximum distance a generated carrier must travel before being collected, $t_{electrical}$, in such textured solar cells would include the thickness of the p-i-n thin-film, *t*, as well as the height, *h*, of the nanowire in the form of,

$$t_{electrical} = t + h. \tag{4}$$

In contrast, radial-junction p-i-n solar cells possess larger periods. As depicted in Figure 12, each nanowire is entirely coated with the p-i-n diode and is completely separated from each other, which may allow for more pronounced light scattering to occur at all wavelengths of light. This increased scattering would enhance the optical path of light, $t_{optical}$, by bouncing the incident light rays back and forth in a manner of trapping the light. Such an interaction between light and the coated nanowires would increase chances of light absorption within the a-Si:H thin-film to generate an effective i-layer thickness, which is thicker than the actual deposited i-layer and has been calculated through geometric analysis of the 3-D hybrid structure as,

$$t_{optical} = \left(1 + \frac{\pi H(t_i + 2t_n + D)}{P^2}\right) t_i. \tag{5}$$

Additionally, $t_{electrical}$ would now be reduced due to the conformal deposition of the a-Si:H p-i-n thin-film in the hybrid 3-D NWSCs to,

$$t_{electrical} = t_i. \tag{6}$$

The low $t_{electrical}$ would reduce carrier recombination. To create radial p-i-n NWSCs as shown in Figure 12, the period of the nanowires must be increased from that shown in Figure 11 in order to enable the conformal p-i-n thin-film coatings that surround the ZnO nanowires.

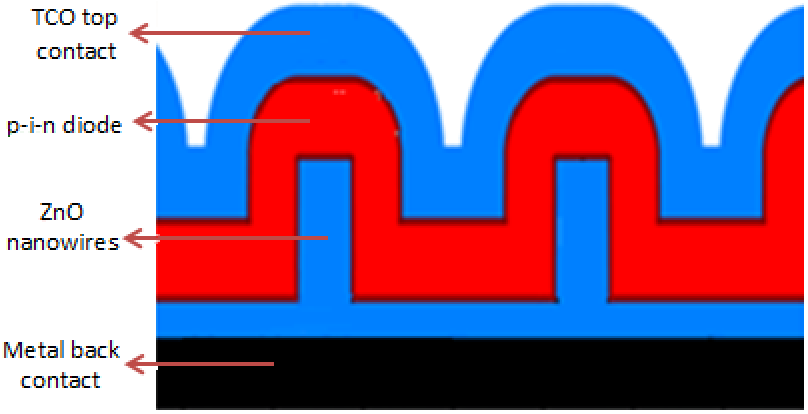

Figure 12. Schematic diagram of an array of hybrid ZnO nanowire/a-Si:H thin-film NWSCs [32]**.**

Analyzing the propagation of light on randomly oriented nanowires is complex. Several groups have shown that randomly oriented structures can be approximated with periodic ones [72]–[75]. To reduce complexity and computation time, the hybrid ZnO nanowire/a-Si:H p-i-n thin-film solar cells have also been simulated using periodic structures and are depicted in Figure 13. Here, light incident on the nanowire enters normal to the structure. The period, height, and diameter of the nanowires are 600 nm, 400 nm, and 120 nm, respectively. The thickness of the AZO TCO is 100 nm and p-i-n layers are 50 nm, 100 nm, and 40 nm, respectively. These p-i-n layers are within the a-Si stack as shown in red in the schematic in Figure 13 (a). Light absorption profiles in terms of power per m^3 were obtained using,

$$Q(x,y,z) = \frac{1}{2} c\epsilon n\alpha |E(x,y,z)|^2 \qquad (7)$$

where *c* is the speed of light, ϵ is the permittivity of the medium, *n* the real part of the refractive index, α the absorption coefficient ($\alpha = 4\pi k/\lambda$, with *k* being the complex part of the refractive index and λ the wavelength), and *E(x,y,z)* the electric field [32].

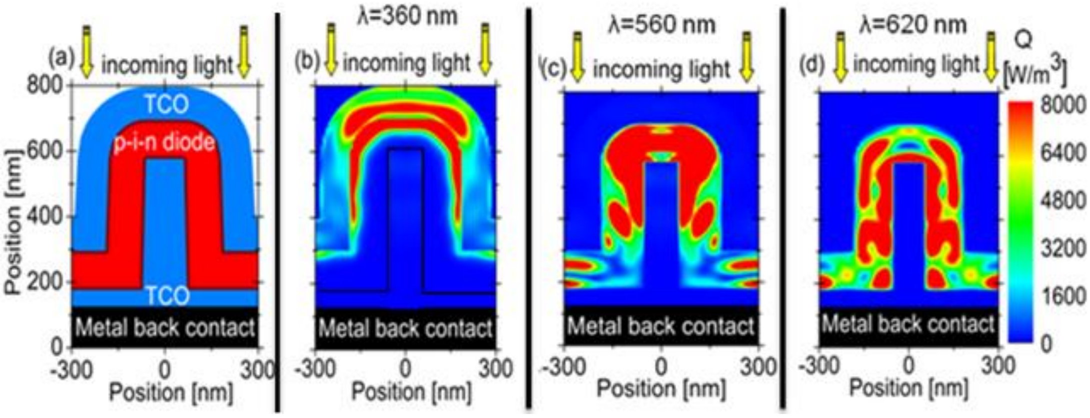

Figure 13. (a) Schematic diagram of the simulated hybrid ZnO nanowire/a-Si:H p-i-n thin-film structure. Light absorption profiles in the hybrid NWSC when light is incident normal to the structure at (b) 360 nm, (c) 560 nm, and (d) 620 nm.

Figure 13 depicts a noticeable change in light absorption within the hybrid 3-D solar cell, depending on the wavelengths of incident light while maintaining all parameters associated to the nanowire itself constant. Incoming light with energy greater than the bandgap of the top contact TCO, (Al-doped ZnO, AZO, with $E_g \approx 3.37$ eV) would be absorbed by this layer. Therefore, at 360 nm, absorption is thicker in the top region of the coated nanowire (Figure 13 (b)). However, when the incoming light is greater than 370 nm, more light absorption is detected around the p-i-n layers, which envelope the ZnO nanowire (Figure 13 (c) and (d)).

The absorption profile can be used to numerically quantify the external quantum efficiency (EQE), which directly correlates light that is incident on the solar cell to charge carriers collected inside the device. The EQE is thus found in the following manner:

$$EQE = \frac{1}{P_{total}} \iiint Q(x,y,z)\, dxdydz \qquad (8)$$

where P_{total} is the total power incident on the unit cell and Q is the absorption profile obtained from Equation 7. EQE assumes that each absorbed photon creates only one electron-hole pair. In turn, the J_{SC} (= $\frac{q}{hc}\int_0^{\lambda_{max}} \lambda EQE(\lambda)S(\lambda)\, d\lambda$ where S is the total irradiance of light under standard AM 1.5G illumination and λ denotes the wavelength of light) can be used to estimate the amount of carriers produced in the hybrid 3-D structures.

The improvement in the EQE of the 3-D solar cell is further enhanced by increasing the height of the structures from 100 nm to 400 nm due to the greater amount of light absorption by the larger 3-D structures. This is shown in Figure 14 alongside a planar solar cell of 300 nm of intrinsic a-Si:H. In the simulated planar a-Si:H solar cell, a J_{SC} of 7.6 mA/cm^2 was obtained while the hybrid 3-D solar cell with a height of 400 nm showed improved carrier collection from 400 nm to 800 nm, generating a J_{SC} of 16.5 mA/cm^2. This enhancement of J_{SC} is more than a factor of 2, which signifies the contribution from the 3-D device structures to create high efficiency solar cells. In comparison, the textured solar cell generated a J_{SC} of 12.8 mA/cm^2. These results provide insight and validation to motivate experimental verification that high performance NWSCs can be achieved from such hybrid 3-D structures.

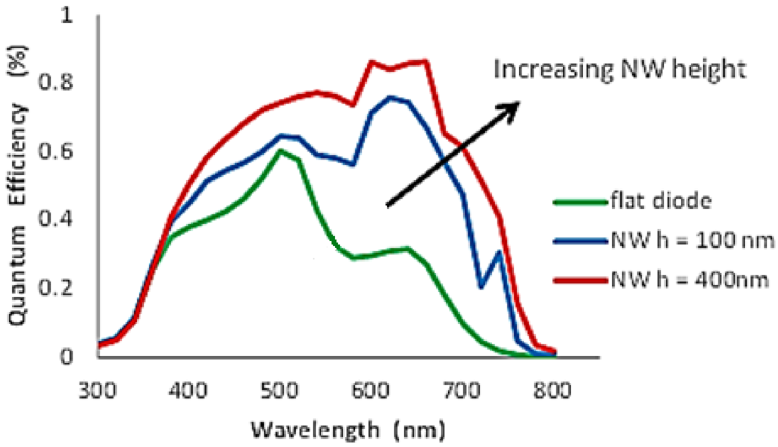

Figure 14. EQE spectra of simulated 3-D NWSCs of *h* = 100 nm and 400 nm and a reference planar (flat) solar cell.

2.3.2.3 Two-Step Fabrication Approach for Flexible Nanowire Solar Cells

The past ~ 7 years has experienced considerable interest in the research of fabricating flexible NWSCs due to the versatility the power sources would provide applications that require high efficiency solar cells that are bendable, portable, and are space-constrained. The most common technique employs a two-step transfer of the array and is illustrated in Figure 15:

(1) Synthesize nanowires on rigid substrates that can endure high temperatures or plasma conditions and,

(2) Transfer grown nanowires onto the flexible substrate.

Both top-down and bottom-up approaches have been used in the first step of synthesizing nanowire arrays. The fabricated nanowire arrays have been either peeled-off from the rigid substrate or the sample would undergo a CMP process to etch the rigid substrate completely and obtain a flexible NWSC array. High density wire arrays that are ~ 50 µm in height have been fabricated using this two-step approach [21]. Moreover, several groups have successfully fabricated flexible NWSC arrays as shown in the SEM and optical micrographs in Figure 16, depicting the high density nanowire growth and high bendability of the flexible nanowire array.

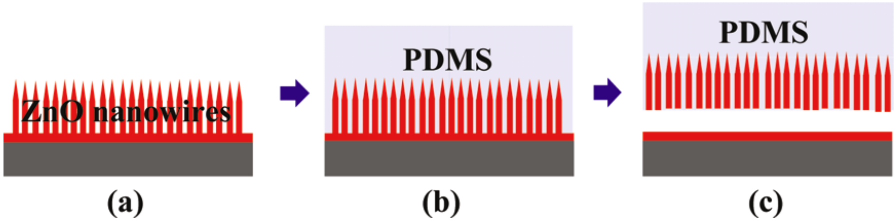

Figure 15. Fabrication flow of a flexible ZnO nanowire array that shows (a) grown ZnO nanowires, which are then (b) encapsulated in PDMS, and (c) removed from the rigid substrate [30]**.**

However, the transfer process requires patience and expertise due to its complexity in successfully breaking apart the nanowire arrays from its native substrate, which is typically Si due to the ability of the substrate to withstand temperatures > 600ºC or plasma conditions, which enable nanowire synthesis. The technique has shown to work most successfully when an additional PDMS coating is used to embed the nanowire array; then, the PDMS can be used to remove the nanowire array out of its native substrate [17]. However, in doing so, the additional PDMS layers may limit the mechanical bendability of the flexible sample and thereby, affect the functionality of the array. Moreover, the greater challenge is to ensure a high success rate and robustness in order for the technology to be compatible with large-area solar cell fabrication. Although the process has shown promising results, fabricating the nanowire diodes directly on the flexible substrate could greatly improve the fabrication yield and allow for all wires to contribute to enhancing the electrical characteristics of the cell.

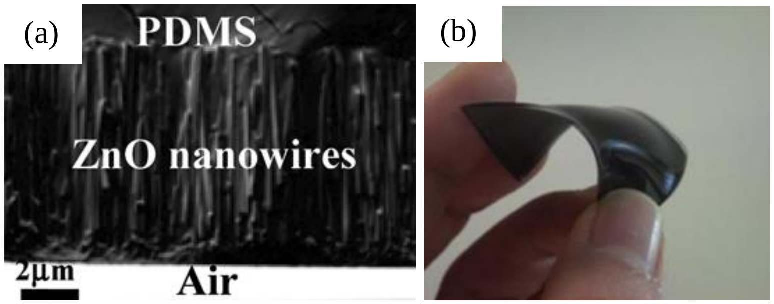

Figure 16. (a) SEM micrograph of the fabricated flexible ZnO nanowire array using the two-step process [30] **and (b) optical image of an array of Si nanowires encapsulated in PDMS** [21]**.**

Furthermore, GaAs nanowires have been grown directly on flexible carbon nanotube (CNT) substrates to withstand temperatures > 550ºC but, high sheet resistances (R_{sheet} ~ 5900 Ω/sq) of the CNT require post-annealing processing of at least 400ºC to lower the R_{sheet} to ~ 68 Ω/sq [34]. Still, poor rectifying behaviour from the fabricated p-n junctions was observed, which the authors suggest may be due to the interface quality between GaAs and CNT.

To this extent, only ZnO nanowire arrays have been grown directly on PDMS [30], PEN and polyethylene terephthalate (PET) [76] substrates but, none have reported on the effects mechanical bending of the substrates would have on the nanowires. Also, NWSC arrays fabricated on these flexible substrates have not been investigated when mechanically bent. Thus, such an investigation could lead to further developments in flexible 3-D solar cells.

Chapter 3

Growth of ZnO Nanowire Arrays

In this chapter, experiments of the ZnO nanowire growth on rigid and flexible substrates are presented. Section 3.1 details the experiments conducted and factors that contributed to the growth of ZnO nanowires. Section 3.2 concludes the chapter with a discussion about the ZnO nanowire growth on arbitrary substrates, including rigid glass and PEN flexible media.

3.1 Growth of ZnO Nanowires

To fabricate hybrid 3-D solar cells, the first step is to synthesize the ZnO nanowires, which act as the backbone pillars and provide the desired 3-D structure. This research uses a hydrothermal approach to grow ZnO nanowires in a bottom-up fashion. Key reasons for adapting this growth technique over others are the low-cost processing requirements, lack of expensive vacuum technology, low toxicity emanating from the process (ZnO is non-toxic), and simplicity in synthesizing nanowires over large area. Furthermore, this growth process for crystalline ZnO nanowires [77], [78] is compatible with current fabrication of thin-film solar cells, easing the integration of the processes to fabricate 3-D hybrid devices. Since the growth method does not require high temperatures, it is especially attractive for the purposes in this research of growing the nanowires directly on low melting-point PEN plastic substrates.

ZnO nanowires that are grown in a hydrothermal solution possess a hexagonal wurtzite crystalline structure, which consists of a polar surface in the [0001] c-axis direction. The polar surface is energetically favorable to growth, enabling the growth of a 1-D cylindrical structure [77]–[80]. The aqueous solution, which provides the required sources of species for ZnO nanowire synthesis, contains 25 mMol equimolar zinc nitrate hexahydrate ($Zn(NO_3)_2.6H_2O$, Sigma Aldrich) and hexamethylenetetramine (HMTA, $C_6H_{12}N_4$, Sigma Aldrich). These salts decompose in the following manner once placed in a thermal ambient to form ZnO:

$$C_6H_{12}N_4 + H_2O \rightarrow 6CH_2O + NH_3 \qquad (1)$$

$$NH_3 + H_2O \rightarrow NH_4^+ + OH^- \qquad (2)$$

$$Zn^{2+} + 2OH^- \rightarrow Zn(OH)_2 \qquad (3)$$

$$Zn(OH)_2 \rightarrow ZnO + H_2O \qquad (4)$$

Due to the controlling parameters that exist in the hydrothermal approach to assist growth, the process can be easily tweaked to synthesize the desired nanostructures. Specifically in this research, temperature, seed layer type and thickness, and sample duration in solution are parameters that were used to control the nanowire growth in terms of nanowire height, diameter, and density.

To control these conditions, the hydrothermal set up consisted of a hotplate, magnetic stir-bar to continually establish a uniform solution, thermometer, Al foil covers to minimize evaporation of the solution, a Teflon sample carrier, and beakers. First, the substrate is thoroughly cleaned using the RCA-1 method, which is discussed in more detail in Section 3.2.1. Next, a ZnO or AZO seed layer is deposited via RF-sputtering or spin-coating nanoparticles on the substrate (discussed in Section 3.1.2). The seeded substrate is then immersed in the hydrothermal solution and is maintained for several hours at 88ºC; reasons for choosing this temperature are discussed in Section 3.1.1. The sample is positioned face-down in solution to allow the homogeneously grown precipitates to fall onto the base of the container instead of on the nanowires that grow on the seeded substrate. At the end of the growth period, the sample is removed from the solution, thoroughly rinsed with de-ionized water and dried with N_2.

When the aqueous bath reaches supersaturation, which is when the amount of solute concentration in the solution exceeds that of the saturated solution, solid particles form, producing a cloudy yellow solution. When the ratio of supersaturation is ~ 1, heterogeneous nucleation on foreign surfaces is promoted [81], [82]. Heterogeneous nucleation is when a nucleation site is used for the formation of nanowire growth while homogeneous nucleation is nucleation that occurs without any preferential nucleation sites. Heterogeneous nucleation of solid phases occurs more easily than homogeneous nucleation due to the lower activation energy barrier involved [82], [83]. Thus, a seed layer is deposited on the substrate to promote heterogeneous nucleation and increase the rate of ZnO nanowire growth in an up-right orientation; this control parameter is further discussed in Section 3.1.2. Section 3.1.3 discusses how sample duration in the solution also increases nanowire length, and the steps taken to further increase the nanowire growth rate.

3.1.1 Thermal Effects on Nanowire Growth

Different temperatures of the growth solution were tested to determine the level at which ZnO nanowire growth occurs most rapidly. The thermal decomposition of zinc nitrate hexahydrate provides the required Zn^{2+} ions while HMTA provides hydroxyl ions at a slow but controlled rate to ensure the supply would not be depleted by precipitation [82]. Although elevated temperatures provide the energy needed for species to dissociate and bond, which ultimately help nanowire growth, continuing to increase the temperatures beyond a certain temperature threshold in anticipation of further increasing the rate of growth is disadvantageous. This disadvantage occurs because the additional energy would now be sufficient enough to homogeneously nucleate species in solution; this condition creates competition for heterogeneous nucleation as the limited supply of species are being used for both types of growth. The optimum point at which homogeneous nucleation is minimal while heterogeneous nucleation is most efficient was assessed by varying the temperatures in several growth experiments. Figure 17 presents SEM micrographs of the nanowire growth at different temperatures. After a period of 1 hour, temperatures less than 75ºC did not show any nanowire growth (Figure 17 (a)). Nanowire growth appeared at a growth rate of ~ 16.7 nm/min at an average temperature of 88ºC. Above 88ºC, the diameters of the nanowires tended to slightly increase and the growth rate decreased to ~ 7 nm/min; at an average of 97ºC, completely disordered nanotubes emerged. Thus, to incorporate the highest nanowire growth rate in this work, an average growth temperature of 88ºC was established.

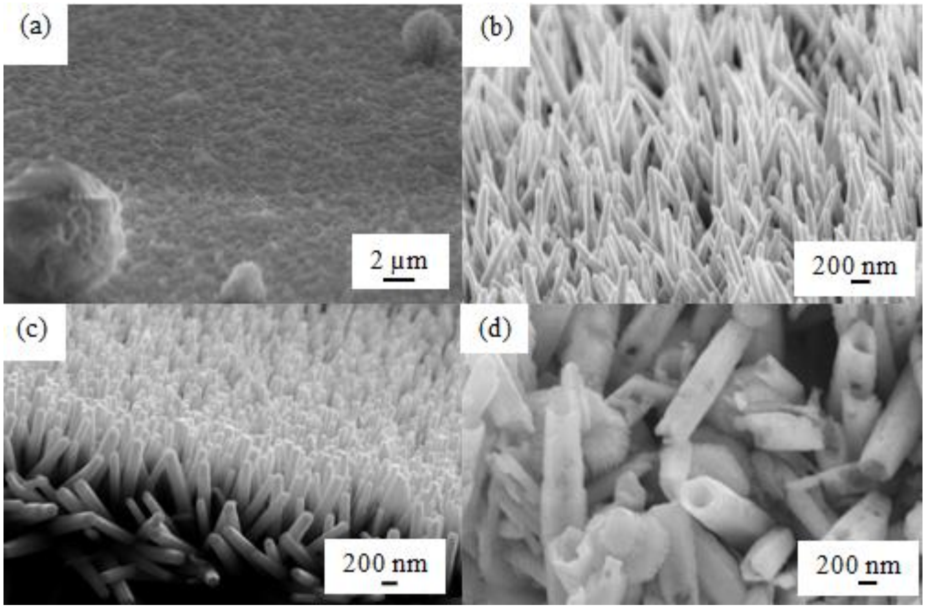

Figure 17 (a). Nano-balls synthesized at < 75ºC, (b) nanowires at 88ºC, (c) nanorods at 90ºC, and (d) nanotubes grown at 97ºC.

3.1.2 Seed Layer Uses for ZnO Nanowire Growth

A ZnO seed layer promotes heterogeneous nucleation on an arbitrary substrate. Moreover, the seed layer helps position the nanowires in specific locations and orient the nanowires upright using its grains as nucleation spots for subsequent nanowire growth, similar to the role of a metal catalyst droplet used in the growth of Si nanowires. Yamabi *et al.* have already verified that upright ZnO nanowires can be grown only if a ZnO crystalline seed layer is used [84]. Two methods have been assessed to act as seed layers for ZnO nanowire growth:

I. RF-sputtered ZnO thin-film in a vacuum chamber

II. ZnO nanoparticles produced from the thermal decomposition of zinc acetate dihydrate salt

Both ZnO thin-film and ZnO nanoparticles can act as seed layers for vertical nanowire growth. In the case of a thin-film seed layer, the grains of the film help position the nanowires in specific locations on the surface and orient the wires in a manner dictated by the c-axis of the ZnO grains. The same process occurs with ZnO nanoparticles where dispersed nanoparticles dictate the location of ZnO nanowire growth.

SEM micrographs revealed different nanowire diameters when the seed layer thicknesses were varied. This correlation between the ZnO seed layer thickness and nanowire diameter are detailed in Section 3.1.2.1. Characterization of the seed layer thickness occurred after patterning the layers and measuring the height profile with a Dektak stylus profilometer; the seed layer morphology and nanowire growth characterization were performed using a Dimension 3100 atomic force microscope (AFM) and a Zeiss LEO field-emission SEM, respectively. Following this discussion, characteristics of the ZnO nanoparticle seed layer are detailed in Section 3.1.2.2.

3.1.2.1 RF-Sputtered ZnO Thin-Film Seed Layers

A ZnO thin-film is RF-sputtered on a substrate as the seed layer (Figure 18 (a)) prior to nanowire growth. The seed layer acts as the template for vertically oriented nanowire growth due to lattice-matching with ZnO nanowires. Grains, which compose the seed layer, assist in subsequent heterogeneous nucleation on the substrate once the sample is placed in solution at an elevated temperature. 1 µm × 1 µm AFM images in Figure 18 (b) and (c) show grains of the ZnO thin-film, which were 27 nm and 200 nm thick, respectively. The average grain sizes of these films were measured to be 25 nm and 53 nm, respectively, indicating that the grain size can be controlled by changing the ZnO thin-film thickness. This change in grain size of the seed layer provides a direct relationship to subsequent diameters of nanowires grown on these seed layers. SEM micrographs that were obtained of the ZnO nanowires grown subsequently on the thin-film seed layers showed average nanowire diameters of 40 nm and 62 nm, respectively (Figure 18 (d) and (e)), corresponding to the AFM images on Figure 18 (b) and (c). Thus, the nanowire diameters can be controlled in this manner by changing the thickness of the seed layer used for growth.

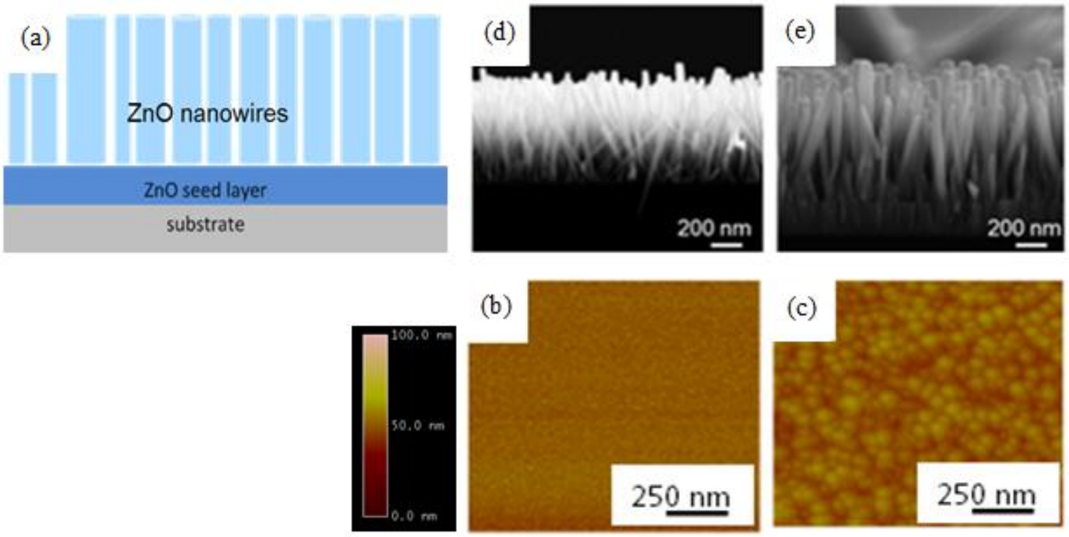

Figure 18. (a) Schematic diagram of ZnO nanowire growth. (b) AFM image of 27 nm ZnO seed layer and (c) 200 nm ZnO seed layer. (d) SEM images of ZnO nanowires grown on the 27 nm ZnO seed layer and (e) ZnO nanowires grown on the 200 nm ZnO seed layer.

Moreover, the seed layer thickness can be used to change the density of the nanowire array. Table 2 presents average ZnO nanowire heights and densities grown on 1.5 nm, 5 nm, and 10 nm thick ZnO thin-film seed layers for 2 hours under the same hydrothermal conditions mentioned above. Although a significant change to the nanowire density grown on seed layers of thickness 5 nm and 10 nm was not detected, the density was visibly less once the seed layer thickness was reduced to 1.5 nm (see Table 2). Decreased nucleation sites reduce the density of nanowires grown on the surface, and thus, results in an increase in the nanowire growth rate due to more efficient use of the species in solution for the remaining nanowires to grow. Thus, nanowires with average heights of 1.1 μm was observed for the 1.5 nm thick seed layer, while the 5 nm and 10 nm thick seed layers had average nanowire heights of 700 nm and 680 nm, respectively.

Table 2. ZnO nanowire array growth characteristics based on seed layer thicknesses used.

Seed Layer Thickness [nm]	Average Nanowire Length [nm]	Nanowire Density [cm^{-2}]
1.5	1100	4×10^{8}
5	700	8×10^{8}
10	680	1×10^{9}

3.1.2.2 ZnO Nanoparticle Seed Layers

To further reduce the density of ZnO nanowires that could be grown on a substrate and to enable greater control of the nanowire density, ZnO nanoparticles were synthesized as an alternative seed layer. ZnO nanoparticles are formed using a well-dispersed aqueous solution of zinc acetate dihydrate ($Zn(CH_3COO)_2 \cdot 2H_2O$, Sigma Aldrich) [76], [85]. Once the solution is drop-casted or spin-coated on the substrate and annealed for several minutes at a low temperature, precipitation of the salt forms 30 – 100 nm diameter sized ZnO nanoparticles (average ~ 76 nm). The following chemical reactions occur during nanoparticle synthesis:

$$\mathrm{Zn(CH_3COO)_2} + \mathrm{H_2O} \rightarrow \mathrm{Zn^{2+}} + 2\mathrm{(CH_3COO)^{-}} \qquad (1)$$

$$\mathrm{Zn^{2+} + 2OH^{-} \rightarrow Zn(OH)_2 \rightarrow ZnO + H_2O} \quad (2)$$

$$\mathrm{Zn(OH)_2 \rightarrow ZnO + H_2O} \quad (3)$$

Upon annealing, the zinc acetate crystallites decompose to form ZnO nanoparticles, which are oriented in the [0001] c-axis direction. Similar to the thin-film seed layer, ZnO nanoparticles help position and orient subsequent nanowires grown on the substrate surface. Figure 19 depicts a 1 µm x 1 µm AFM image of a ZnO nanoparticle seed layer, which was synthesized using 25 mM of aqueous zinc acetate dihydrate. The number of seeds revealed in the image is ~ 66% lower than that obtained from the thin-film seed layers. The density of seeds can be enhanced by increasing the number of layers of nanoparticles spin-coated on the substrate or by drop-casting a high molar concentration of zinc acetate solution.

Comparing the results obtained from both seed layers, an increased density of nanowires helps orient the nanowires towards the surface normal. This effect is due to an increased packing density, which constricts the nanowires to orient in the direction of the surface normal and provide more space for its neighboring nanowires to grow similarly [80]. If the packing density is low, then the nanowires can grow freely depending on the dispersion of the nanoparticles.

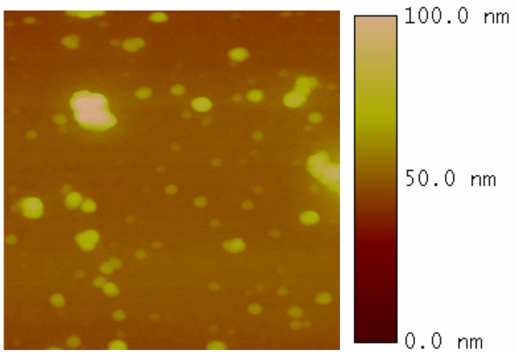

Figure 19. AFM image of ZnO nanoparticles synthesized from 25 mM of zinc acetate solution.

Furthermore, spin-coating layers of nanoparticles has helped further control the density of nanowires grown [76], [86]. Figure 20 depicts SEM micrographs of different densities of nanowires grown after (a) 1 layer (8 × 10^{17} cm^{-2}) and (b) 2 layers (2 × 10^{18} cm^{-2}) of ZnO nanoparticles spun-coated on the substrate.

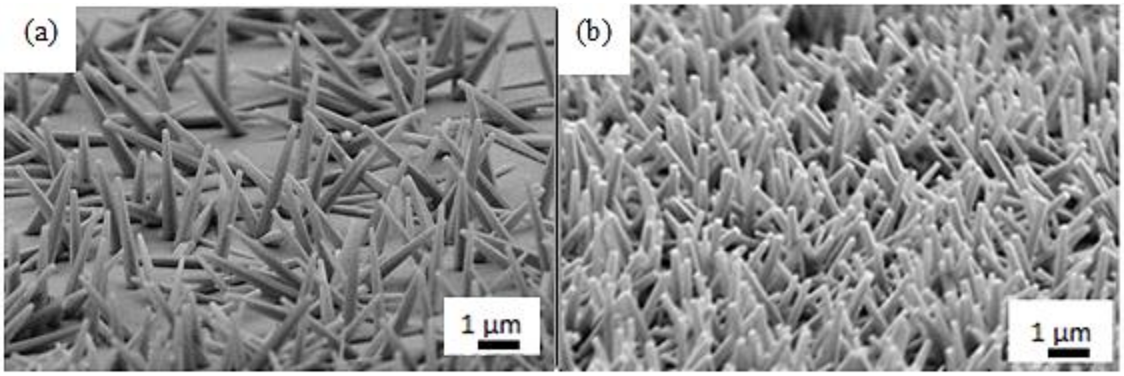

Figure 20. Tilted SEM micrographs of nanowires grown on ZnO nanoparticles that were spin-coated with (a) 1 layer and (b) 2 layers of nanoparticles.

ZnO film and nanoparticle seed layers can grow ZnO nanowire arrays with a surface morphology that is quasi-aligned as seen with the nanowires in Figure 20. Due to the improved control in nanowire density provided by the nanoparticle seed layers, the same process has been used to fabricate NWSCs with an average separation of 1.2 µm in this research and is further discussed in Chapter 4.

3.1.3 Nanowire Growth Enhancement

The duration at which the samples are placed in the aqueous solution is used as a control parameter to lengthen the ZnO nanowires. As the sample duration in solution increases, the growth of the nanowires also gradually increases. Table 3 depicts average dimensions of ZnO nanowires grown in the first two hours where they were placed in solution. Little change to the diameter of the ZnO nanowires was noticed as the sidewalls are nonpolar [81], [87]. Thus, the cylindrical structure is preserved due to the faster morphology changes made at the polar sites of the ZnO nanowire (i.e. increased height via the polar facets of the nanowires).

Table 3. ZnO nanowire growth rates in the first two hours of synthesis. (Regrowth procedure is not used here.)

Seed layer thickness [nm]	Nanowire height after 1 hour [nm]	Nanowire diameter after 1 hour [nm]	Nanowire height after 2 hours [nm]	Nanowire diameter after 2 hours [nm]
Thin-film: 5	800±100	32±15	1100±150	36±15
Thin-film: 10	800±100	32±12	1000±134	32±13
Thin-film: 27	700±50	40±18	1000±127	60±14
NP: 1 layer	1000±100	90±30	1520±100	105±50
NP: 2 layers	1000±200	100±10	1500±50	130±20

By replacing the growth bath with fresh solution, a significant boost to the nanowire growth rate is detected; this concept has been termed “regrowth” in the studies. The regrowth process enables an increased interaction between species in solution to partake in the nanowire growth, ultimately resulting in increased height and slightly increased diameter nanowires. This method eliminates the otherwise linear growth process obtained with a sample submerged in a single bath. After obtaining ~ 1 μm in height nanowires after one hour and running a regrowth procedure, nanowires of nearly 2 μm in height were obtained. An aspect ratio of 1:10 (diameter/height) is on average obtained for nanowires grown using the regrowth method (using the nanoparticle seed layer).

3.2 ZnO Nanowire Growth on Arbitrary Substrates

The above experiments used glass substrates to assess the nanowire growth. Subsequently, PEN plastic substrates were also used to assess the growth characteristics. Section 3.2.1 discusses the cleaning process used for all substrates while Section 3.2.2 discusses the types of substrates used in greater detail and the ZnO nanowire growth characteristics on plastic.

3.2.1 Substrate Cleaning

Prior to nanowire growth, the first step was to ensure clean substrates were used. All glass substrates used for the characterization of film and fabrication of devices are 3” in diameter and 0.5 mm thick. All substrates were thoroughly washed using the Radio Corporation of America (RCA-1) method to remove organic residue and subsequently dried using N_2. The RCA-1 method included heating DI water, aluminum hydroxide, and hydrogen peroxide at a ratio of 5:1:1 up to ~ 80ºC, at which point bubbling of the solution begins and the samples are placed inside for ~ 30 minutes. Once completed, the samples are thoroughly washed with DI water and dried with N_2.

3.2.2 Substrates Used

Rigid substrates used in this research include three-inch Corning Eagle 2000^{TM} glass substrates and lightly doped p-type c-Si substrates. C-Si substrates used in the nanowire growth step were only to assess the ability to grow ZnO nanowires on different substrates. Glass substrates were used as a reference surface when comparing the growth on PEN substrates since it is a rigid and stable surface and the conventional substrate type used in the literature. Furthermore, since the maximum process temperature of 220ºC was well under the melting temperature, T_m, of glass (670ºC) [88] and its surface roughness was < 0.5 nm, glass substrates were used to fabricate reference devices, too.

The PEN plastic is ~ 125 µm thick and is flexible down to a tested radius of curvature of 4 mm. Its T_m is ≈ 263ºC, which allows some freedom for device fabrication at elevated temperatures. To minimize deformation of the substrate, the process temperatures used to fabricate solar cell devices in this research were set to below 230ºC.

Direct integration of nanowires on PEN plastic substrates has been established. PEN plastic was cut into 3” diameter substrates to follow the same nanowire growth conditions as discussed earlier. Once cut into separate substrates, they were washed and cleaned as described in Section 3.2.1 and subsequently processed for nanowire synthesis. Using a ZnO thin-film seed layer, ZnO nanowires were grown hydrothermally and are shown in Figure 21.

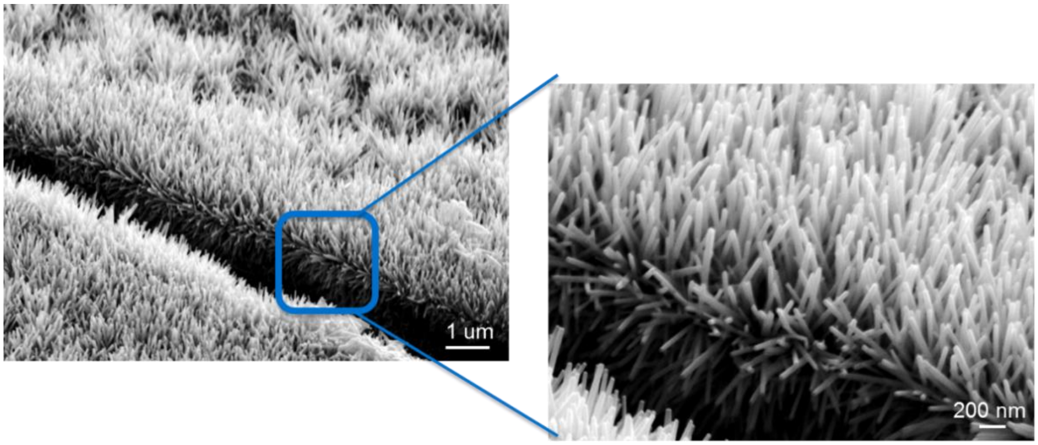

Figure 21. SEM micrograph of ZnO nanowires grown on PEN flexible substrates. Outset: High resolution SEM micrograph of nanowires along a convex bend in the PEN substrate.

As expected, the ZnO nanowires are vertically oriented since a thin-film seed layer was used to assist nucleation. A 2 hour regrowth period in a hydrothermal solution at 88ºC was used for the nanowire growth shown above and resulted in ~ 2 μm in height nanowires with a diameter of 80 nm.

In anticipation of fabricating nanowire diodes on PEN flexible substrates, ZnO nanowires were grown with increased periods. On average, ~ 1 μm in height and 130 nm diameter nanowires with a spacing of ~ 1.2 μm were synthesized using ZnO nanoparticle seed layers as shown in Figure 22. The density of nanowires was purposely reduced from ~ 10^{19} cm^{-2} to ~ 10^{18} cm^{-2} for subsequent diode deposition and is discussed in more detail in Chapter 4.

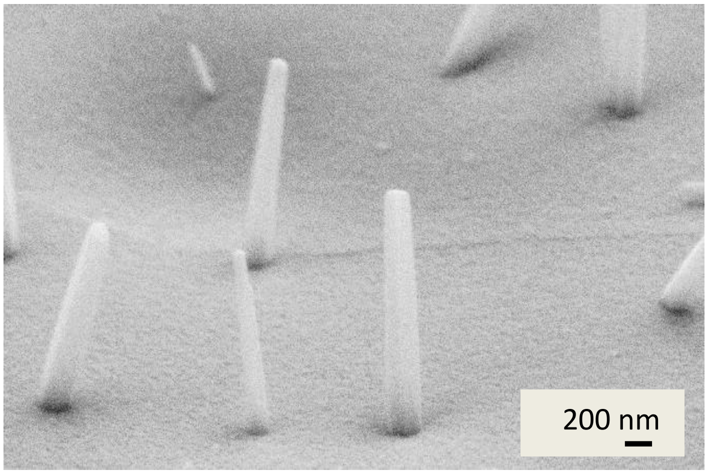

Figure 22. SEM micrographs of ZnO nanowires with increased periods grown on a PEN flexible substrate.

Chapter 4

Thin-film Materials Characterization and Deposition on ZnO Nanowire Arrays for Device Fabrication

This section discusses the thin-film materials used to fabricate the planar and hybrid NWSCs. After a discussion in Section 4.1 about the bottom electrode chosen for this work, the p-i-n a-Si:H thin-films are discussed in Section 4.2. Preliminary studies to deposit the top contact and masks created to pattern the device areas on the substrates are further discussed in Section 4.3. Conductivity calculations shown in each of the sections are from I-V measurements obtained from a Keithley 4200 parameter analyzer while optical band-gap calculations were obtained by using optical transmittance measurements of the films.

Finally, Section 4.4 discusses the integration of the thin-film with ZnO nanowires. Incorporating ZnO nanowires with the p-i-n a-Si:H thin-film resulted in the ability to fabricate textured structures. The chapter concludes with a discussion about conformal thin-film coverage on ZnO nanowires by reducing the ZnO nanowire density and enabling hybrid 3-D solar cell fabrication.

4.1 Selection of Bottom Electrode

Since the devices fabricated were substrate-oriented, the bottom electrode was deposited first using physical vapor deposition (PVD) sputter-coating. The bottom electrode must possess three main characteristics:

1. Compatibility with the hydrothermal nanowire growth process
2. Maintain high conductivity as an electrode of the solar cell
3. Possess superior optical reflectance and low transmittance and absorption
4. Ensure stable composition (i.e. does not interact) during deposition of subsequent materials on top of the electrode

Although ~ 100 nm thick Al had a conductivity of ~ 2.7×10^3 S/cm and is the preferred bottom electrode metal primarily due to its > 90% average optical reflectance achieved in the visible spectrum (Figure 23 (a)), its incorporation during ZnO nanowire growth revealed poor integration. It was observed that the soft Al thin-film disintegrated by the agitation from the elevated temperatures in solution, and thereby peeled-off during the hydrothermal growth phase. Moreover, SEM micrographs showed platelet formation alongside nanowire growth. This scenario produced two entirely different structures, and in doing so, impeded nanowire growth. The decomposition of the Al film contaminated the solution where Al ions entered the hydrothermal solution, changing its pH [89]. The resulting ZnO growth was a mixture of platelets and nanowire growth. To prevent the inter-diffusion of Al, an additional layer of ZnO was sputter-coated before nanowire growth to minimize the Al decomposition. However, the experimental results still revealed platelet formation (Figure 23 (b)) and unstable nanowire growth, which deemed Al unsuitable for the solar cell fabrication process.

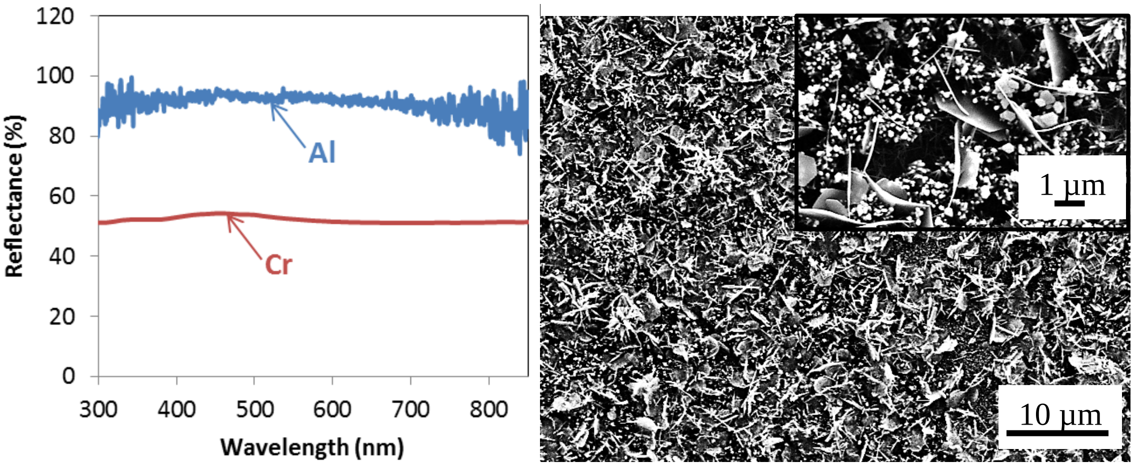

Figure 23. (a) Reflectance measurements of Al and Cr thin-film. Both films were ~ 100 nm thick. (b) SEM micrographs that reveal platelet growth in the nanowire array when using Al thin-film under the ZnO seed layer.

Cr and Ni were deposited and tested for their compatibility with the fabrication process of planar and hybrid 3-D solar cell devices. Both films possessed film conductivity ~ 4.0×10^3 S/cm and average reflectivity of ~ 52% for 100 nm thick film. Although the optical reflectivity of these thin-film metals were lower compared to Al thin-film (Figure 23 (a)) both metals did not decompose during the hydrothermal growth of ZnO nanowires. SEM images did not reveal any change of nanowire growth on Cr or Ni thin-films. Cr was chosen over Ni due to easier accessibility to sputter-coat the film and the capability to deposit the thin film simultaneously on six substrates at a run-time in the PVD sputtering system at the Giga-to-Nanoelectronics laboratory clean-room facility.

4.2 Characteristics of the p-i-n a-Si:H Thin-Film

As discussed in Chapter 2, the n^+, p^+ a-Si:H thin-film layers collectively produce a SCR within the i-layer, which is imperative to efficiently separate excess electron-hole carriers towards their respective electrodes in the solar cell. Deposition of the n^+-i-p^+ a-Si:H thin-film layers was accomplished by using a 13.56 MHz multi-chamber PECVD system at low temperature to ensure deposition compatibility onto flexible substrates. This section discusses the characteristics of each of these Si thin-films for both planar and hybrid NWSC fabrication.

4.2.1 Characteristics of the n^+ Thin-Film

N^+ a-Si:H thin-film was fabricated by introducing phosphine (PH_3) during deposition of the a-Si:H film to increase the concentration of electrons in the thin film. Device fabrication incorporated a combination of $SiH_4/PH_3/H_2$ gases, which flowed at 40/40/200 SCCM at an RF power density of 3 mW/cm^2 at 900 mTorr and 220ºC. The film was uniform about a 3-inch diameter substrate (Figure 24 inset), and was deposited at a growth rate of 5.1 nm/min. An n^+ a-Si:H thin-film thickness of 40 nm was used, with conductivity measurements resulting on average to be 8×10^{-3} S/cm. Raman measurements revealed a peak at 480 cm^{-1} (Figure 24), which confirmed the amorphous property of the n^+ thin-film.

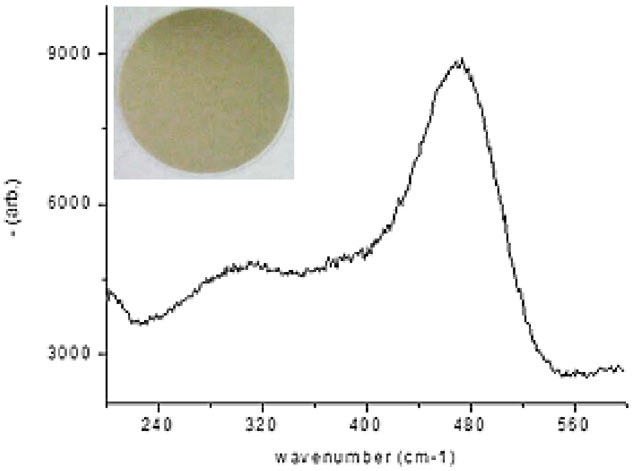

Figure 24. Raman spectrum of the n$^+$ a-Si:H thin-film revealing its amorphous property. Inset: Film uniformity of 44 nm thick n$^+$ a-Si:H thin-film.

4.2.2 Characteristics of the Intrinsic a-Si:H Thin-Film

The intrinsic a-Si:H layer was grown at 220ºC with a SiH_4 flow of 20 SCCM, process pressure of 400 mTorr and power density of 3 mW/cm^2 for approximately 300 nm with good uniformity on a 3-inch diameter substrate (Figure 25). From Fourier Transform Infrared (FTIR) spectroscopy, a large Si-H to Si-H_2 ratio would indicate an increased quality of a-Si:H thin-film deposited. Deconvoluting the measurements (Figure 25 (a)) indeed showed a lower amount of Si-H_2 (at 2100 cm^{-1}) to Si-H (at 2000 cm^{-1}) bonds in the intrinsic film, indicative of a larger concentration of passivated dangling bonds [90]. The low power and pressure used in the deposition process assisted in this process of passivating Si dangling bonds through Si-H passivation. A higher concentration of Si-H_2 bonds, as is the case in a-Si:H deposited through glow discharge at 100ºC, creates a columnar microstructure, which increases the dangling bond content within the thin-film [90].

The material properties of the intrinsic layer were further characterized using UV-Vis spectroscopy for optical characterization and a Keithley 4200-SCS parameter analyzer to probe the electrical characteristics. Using optical transmittance spectra of the thin-film, the band-gap was calculated to be 1.71 eV as depicted in Figure 25 (b), similar to that reported in the literature [91]. Thus, incoming light rays consisting of energies greater than 1.71 eV will be absorbed by the intrinsic layer, and will generate free electron-hole pairs within the solar cell device. Conductivity measurements revealed typical device-grade intrinsic a-Si:H values of ~ 4.25×10^{-9} S/cm and a photo-to-dark current ratio of 5, indicating high photosensitivity of the semiconductor film.

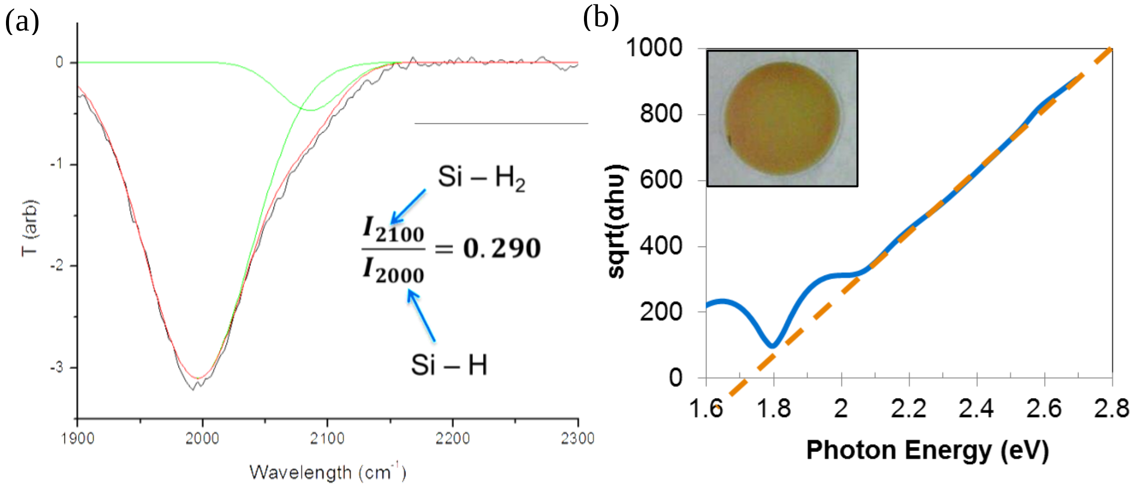

Figure 25. (a) FTIR measurement of the Si-H and Si-H$_2$ molecular concentrations in intrinsic a-Si:H. (b) Bandgap measurement for intrinsic a-Si:H. Inset: Optical photograph of the intrinsic a-Si:H film uniformity.

4.2.3 Characteristics of the p^+ Thin-Film

The p^+ layer is the top-most semiconductor layer of the substrate-oriented solar cells, and is ideally transparent to the incoming light, is highly conductive for efficient charge collection, and should be uniform across the entire device area.

Processing temperature of the p^+ a-Si:H layer was set at 170ºC to minimize dopant diffusion during the p^+ layer deposition into the intrinsic a-Si:H under-layer. The p^+ layer was fabricated by introducing diborane (B_2H_6) during deposition to increase the concentration of holes in the thin film. Device fabrication incorporated a combination of $SiH_4/B_2H_6/H_2$ gases, which flowed at 1/0.5/250 SCCM at an RF power density of 15 mW/cm^2 at 1900 mTorr. Raman measurements revealed a faint peak at 520 cm^{-1} and a bump present at 480 cm^{-1}, indicating that the p^+ thin-film is still a-Si:H, which consisted of an electrical conductivity of 1.69 S/cm. Furthermore, the p^+ layer consistently deposited uniformly about a 3-inch substrate, suggesting reliable deposition of the thin-film and possessed a large band-gap of 2.2 eV, indicating that the deposition process that incorporates a high H dilution passivates band-edge trap states effectively, resulting in a more conductive and slightly larger band-gap.

4.3 Fabrication of the Top Electrode

Also known as the window layer, the top electrode of substrate-oriented solar cells should possess enhanced optical transmittance, electrical conductivity similar to a metal film, and uniform film thickness. Section 4.3.1 discusses the characteristics of the PVD sputter-coated AZO while Section 4.3.2 describes the top metal grid deposited on top of the AZO to maximize the electrical output achieved from the solar cell devices.

4.3.1 AZO Deposition

As the first layer that would interact with incoming photons, it is desirable for the top electrode to possess near 100% optical transmittance such that incoming light would pass through the layer and be absorbed at the intrinsic a-Si:H layer. AZO was chosen due to its theoretically high optical bandgap of 3.37 eV, and a dedicated PVD RF sputter-chamber that already existed in the facility for its deposition in a cluster tool, which permitted thin-film deposition without breaking vacuum during device fabrication. The thin-film was deposited at 150ºC with Ar (15 SCCM) at 5 mTorr and 80 W. Measured conductivity of ~ 80 nm thick AZO thin-film was 1.1×10^3 S/cm, and its optical transmittance and reflectance, as depicted in Figure 26, averaged to 87% and 16%, respectively. The measured optical bandgap was 3.7 eV as depicted in Figure 26 (b), showing the high optical transmittance of the AZO thin-film.

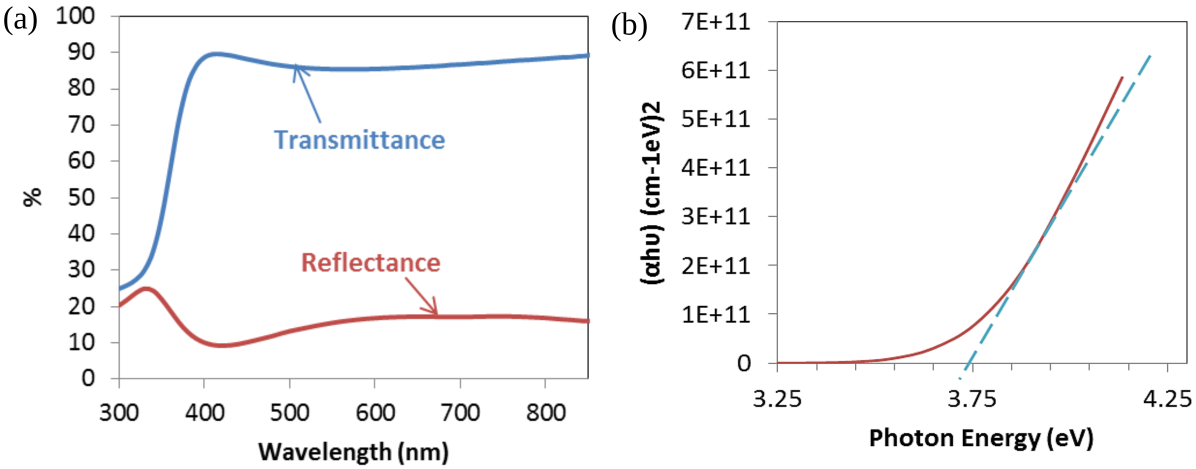

Figure 26. (a) Optical characteristics of 80 nm thick AZO thin-film. (b) Optical band-gap measurement of AZO thin-film.

4.3.2 Top Metal Grid Deposition and Device Patterning

To further enhance the carrier collection from the AZO thin-film, a 50 nm thin Cr top grid was deposited using a shadow mask. This metal grid helped improve the ohmic contact and reduce the series resistance by ~ 10% between the probe tip and the AZO film. The grid was deposited using electron-beam (e-beam) evaporation instead of RF sputter-coating in order to prevent any physical damage via ion bombardment from plasma to occur to the underlying AZO thin-film [92].

Figure 27 illustrates the complete top-down device view on a 3-inch diameter substrate. The crosses depicted in Figure 27 are two bus-bars that intersect each other and are 400 μm in width. The bus-bars vary in size to span an entire device. The smallest devices on the mask did not consist of bus-bars due to exceeding the resolution limit of the laser used to produce the mask.

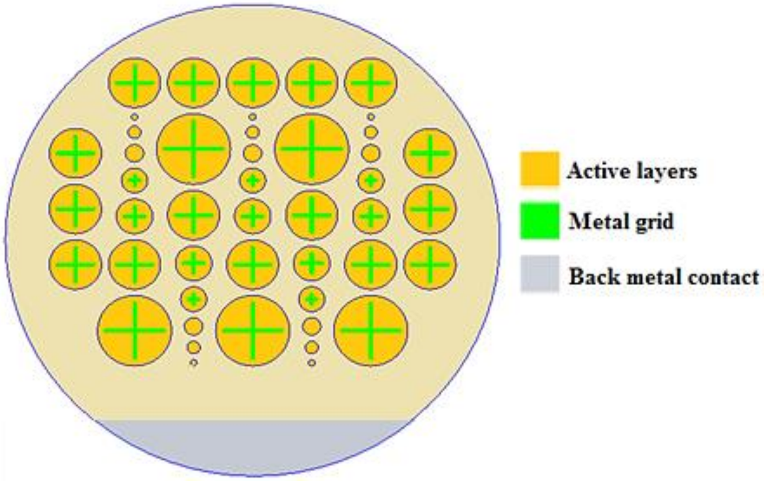

Figure 27. Top-down schematic of planar solar cells of various sizes on a 3-inch diameter substrate.

To fabricate a batch of solar cells, the entire thin-film stack was deposited in the cluster-tool in one vacuum pump. Following the blanket deposition of the films, a Cr mask that consisted of the same pattern as Figure 27 was used to finally pattern each device area through photolithography and thereby, define the active region of the device. Each substrate contained 46 circular shaped devices of various sizes. The largest cell area was 0.95 cm^2 while the smallest cell area was 0.01 cm^2.

4.4 Integration of Thin-Film and ZnO Nanowires

This section presents data that were analyzed to form conformal deposition of p-i-n a-Si:H layers over ZnO nanowires to form hybrid 3-D solar cells. Although a PECVD process is used to conformally deposit thin-film over ZnO nanowires, if a sample of high density grown nanowires is used to fabricate the hybrid 3-D solar cells, then subsequent deposition of the p-i-n thin-film layers and top electrode will coat poorly along the vertical sidewalls of each nanowire as illustrated in Figure 28. Instead, only regions that contain considerable space between nanowires would show conformal coatings of the film deposited.

Figure 28 (a) and (b) are tilted and cross-section images of uncoated ~ 2 µm height and 80 nm diameter ZnO nanowires, respectively, grown using a 27 nm thick ZnO film seed layer. The tilted and cross-section SEM micrographs of the nanowires coated with 430 nm of a-Si:H thin-film are shown in Figure 28 (c) and (d), respectively. Figure 28 (d) shows poor thin-film coverage on the sidewalls of the nanowires although the top surfaces are covered with a-Si:H thin-film. This poor thin-film coverage on the vertical nanowire sidewalls is because the calculated nanowire density is ~1.6×10^{10} cm^{-2}, which is too high for conformal coverage of a-

Si:H thin-film to fabricate truly 3-D NWSCs. The nanowire density was calculated by examining SEM micrographs of the coatings with a post-processing image analyzer (ImageJ) to calculate a percentage of white-to-black pixels covered in the image whose white areas were quantified and divided from the total area of the micrograph to generate a density calculation.

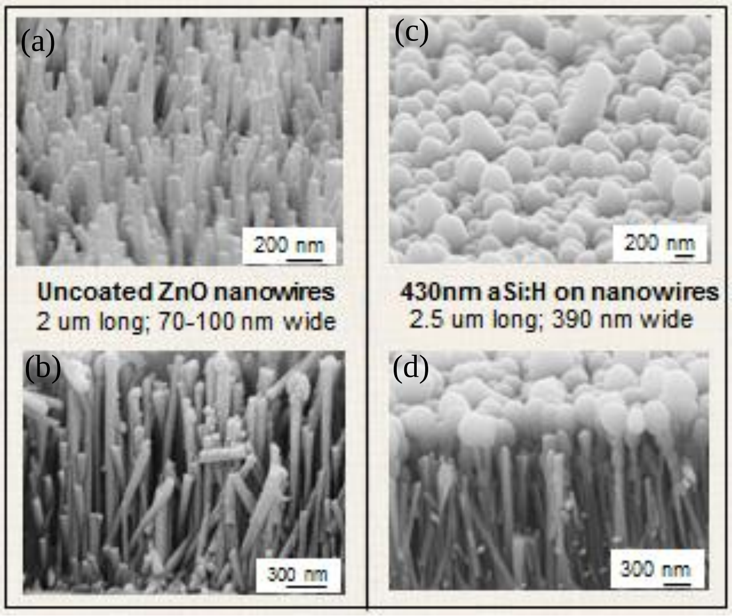

Figure 28. (a) Tilted and (b) cross-section images of uncoated ZnO nanowires; (c) tilted and (d) cross-section SEM images of 430 nm a-Si:H coated on the ZnO nanowires shown in (a) and (b).

4.4.1 Conformal Thin-Film Coverage on ZnO Nanowires

To ensure NWSCs that would produce the optical and electrical enhancements described in Chapter 2 are fabricated, each nanowire must be conformally coated with the thin-film that constitutes a solar cell. For this purpose, since the thin-film stack (that is, p-i-n a-Si:H and AZO thin film) adds to a total thickness of ~ 480 nm, the spacing of the nanowires was increased to ~ 1 µm ± 200 nm by using a ZnO nanoparticle seed layer. Each thin-film was coated separately on the ZnO nanowires to assess the conformity of the films on the 3-D structures.

Figure 29 depicts SEM micrographs of ~ 2 µm ± 220 nm height and 200±100 nm diameter uncoated ZnO nanowires along with 45 nm of n^+ a-Si:H, 300 nm of intrinsic a-Si:H, and 50 nm of p^+ a-Si:H thin-film deposited on the ZnO nanowires, revealing the morphology and thin-film coverage over the 3-D structures.

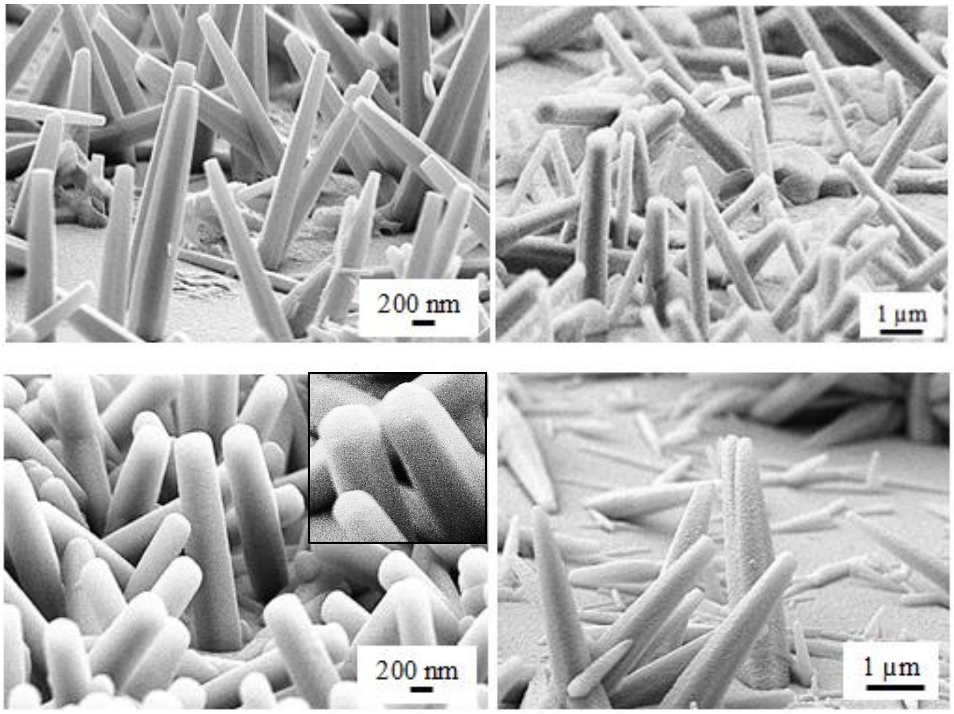

Figure 29. (a) Uncoated ZnO NWs. (b) 40 nm coated n^+ a-Si:H thin-film, and (c) 300 nm intrinsic a-Si:H coated on the NWs; Inset: facets of the ZnO NWs visibly noticed after the a-Si:H coating, and (d) 50 nm p^+ a-Si:H thin-film coated on the ZnO NWs.

The six-fold symmetry of the hexagonal ZnO nanowires was observed along the tops and sidewalls of the a-Si:H layers from SEM micrographs, verifying the conformal nature and 3-D structure of the thin-film on the nanowires. To further verify the conformal thin film coverage over the ZnO nanowires and its uniformity over a 3-inch substrate, the substrate was dipped in hydro-chloric (HCl) acid. Since acidic solutions like HCl selectively etch ZnO compared to a-Si:H, poor coverage of the a-Si:H or pin-holes in the thin film can result in etching of the ZnO and breaking down the 3-D structures. However, SEM micrographs of samples that were submerged in HCl did not show any structural or morphological change to the coated nanowires. Chapter 5 of the thesis discusses the planar and hybrid 3-D solar cells fabricated in this manner.

Chapter 5

Planar and Nanowire Solar Cell Fabrication and Characterization

Section 5.1 of this chapter discusses the fabrication process of planar solar cell devices and 3-D disordered hybrid NWSCs. Section 5.2 analyzes the performance differences of the planar and 3-D NWSCs in terms of their optical and electrical characteristics. The section also explores process limitations when sputter-coating the AZO top electrode on the disordered 3-D devices and provides a potential solution by including ITO nanoparticles to the top electrode. Using the improved device fabrication process, optimum nanowire lengths and densities that led to maximum optical and electrical characteristics from the hybrid NWSCs are studied. The chapter concludes by noting the limitations of the ITO nanoparticle layer specifically, with respect to cracking upon bending.

5.1 Fabrication of Solar Cell Devices

5.1.1 Planar Solar Cell Device Fabrication

RCA1-cleaned glass and flexible substrates were sputter-coated with 100 nm of Cr as the back electrode of the solar cell devices. A 13.56 MHz PECVD cluster system was used to deposit 40 nm of n^+ a-Si:H thin-film at 200°C immediately followed by a 300 nm thick a-Si:H absorber layer deposited at the same temperature and finally, 50 nm of p^+ a-Si:H deposited at 170°C. A final top contact of 80 nm thick AZO thin-film was sputter-coated at 150ºC. The substrate was subsequently patterned using photo-lithography to form active device areas and expose the bottom electrode. A top metal grid consisting of 50 nm of Cr was deposited using e-beam evaporation. Figure 30 depicts a cross-section schematic illustration of the planar a-Si:H thin-film solar cell device.

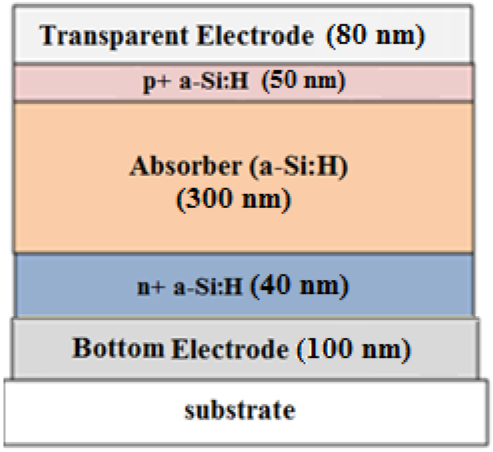

Figure 30. Schematic diagram of the planar a-Si:H thin-film solar cell structures fabricated.

5.1.2 Hybrid Nanowire Solar Cell Device Fabrication

ZnO nanowires were grown on substrates that consisted of a ZnO nanoparticle seed layer, which was synthesized from a 25 mMol zinc acetate dihydrate aqueous solution. The solution was spin-coated on a 100 nm thin Cr-coated substrate, which was placed in a hydrothermal bath for nanowire growth. The hydrothermal bath consisted of 25 mMol equimolar aqueous solution of zinc nitrate hexahydrate and HMTA, and was heated to a bath temperature of 88°C. The synthesis process resulted in the growth of ZnO nanowires with a diameter of 200 ± 100 nm and a height of ~ 2 μm ± 220 nm after a 2-hour regrowth period.

Following the hydrothermal growth process, the ZnO nanowires were photo-lithographically patterned such that the nanowires would exist only in the circular device regions (see Figure 27). This process step occurred as a precaution to minimize the possibility of shunting that may occur to the solar cells with nanowires in areas outside the device region. Positive photo-resist was coated multiple times (2× ≈ 2 μm) to ensure the nanowires in the device regions would be protected from the pattern step and were subsequently wet-etched using HCl acid. Once completed, the photo-resist was removed and the sample was examined using SEM. The remaining nanowires on the substrate showed no change to their morphology. The sample was then placed in a 13.56 MHz PECVD cluster system for the deposition of the n-i-p a-Si:H thin-film layers over the ZnO nanowire structures. The nanowires were conformally coated with ~ 40 nm of n^+ a-Si:H thin-film at 200°C, immediately followed by ~ 300 nm of a-Si:H absorber layer deposited at the same temperature and ~ 50 nm of p^+ a-Si:H at 170°C. Top contact to the 3-D disordered nanowire devices was made with ~ 80 nm of sputter-coated AZO thin-film at 150ºC. Figure 31 (a) illustrates two schematic diagrams of a planar p-i-n solar cell device and a disordered NWSC array. Figure 31 (b) depicts a cross-section SEM micrograph of the ZnO nanowires coated with ~300 nm of a-Si:H thin-film, revealing the disordered nature of the nanowire array.

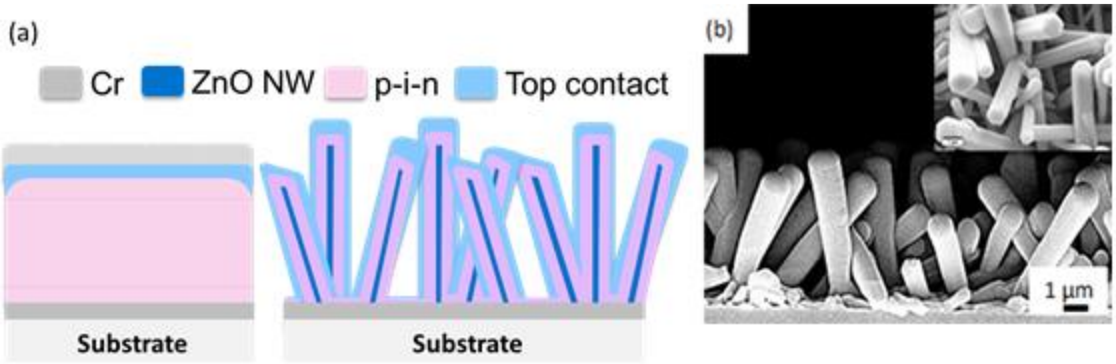

Figure 31. (a) Schematic drawings of the reference planar solar cell and hybrid NWSC structures and (b) Cross-section SEM image of ZnO nanowires coated with 300 nm a-Si:H. Inset: plan-view SEM image of the coated 3-D hybrid structures (SEM image credit to Mr. B. Iheanacho) [33]**.**

5.2 Solar Cell Device Characteristics

This section discusses the performance of the two different solar cell structures fabricated. Optical characteristics of the planar and hybrid nanowire structures were obtained in the visible spectrum using a Lambda 1050 Perkin Elmer UV/visible/NIR spectrophotometer. Current density-voltage (I-V) measurements were performed under standard AM 1.5G illumination conditions at 100 mW/cm^2 (ABET Technologies Sun 2000 solar simulator) and external quantum efficiency (EQE) was measured using a monochromatic light source (PV Measurements) calibrated with a reference silicon solar cell.

5.2.1 Optical Characteristics of Hybrid NWSC Structures and Planar Structures

To determine the optical characteristics of the nanowire network, reflectance (*R*) and transmittance (*T*) measurements were obtained with an integrating sphere in the spectrophotometer to collect scattered light from the samples. From these measurements, the optical absorption (*A*) of the device structures was calculated by $I = T(\lambda) + R(\lambda) + A(\lambda)$ where *I* is the total incoming light. Transmittance measurements from each of the diode structures were ~ 0% due to the thin-film stack and 100 nm thin Cr back contact residing underneath the structures. Therefore, a reduction in reflectance from the device structures indicates an enhancement in the absorption of light within the structure.

Figure 32 depicts the reflectance spectra of a planar solar cell structure alongside the spectrum of a 3-D hybrid NWSC structure. For the planar solar cell device, an average reflectance of ~34% was observed at wavelengths < 550 nm while interference peaks were detected at wavelengths > 570 nm, contributing to a maximum reflectance of ~80%. The hybrid NWSC structure showed an average reflectance of 16% in the measured wavelength spectrum. Suppression in reflectance throughout the broadband visible spectrum was observed compared to the planar solar cell device, suggesting a strong light trapping effect occurs within the 3-D hybrid nanowire device structures that provide greater optical absorption in the 3-D device structures in comparison to the planar device structures.

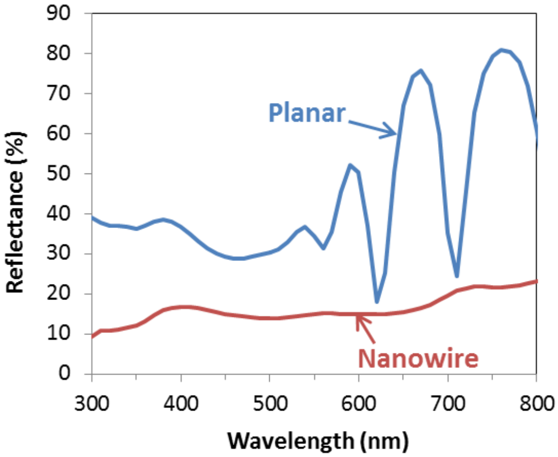

Figure 32. Optical reflectance spectra of planar and 3-D hybrid nanowire solar cell structures.

Furthermore, due to the insulating properties of the ZnO nanowires [93], the light trapped inside the nanowire network is likely absorbed by the 3-D a-Si:H p-i-n solar cell device as was presented in the numerical simulations of the 3-D hybrid NWSC devices in Chapter 2 of this dissertation. Street *et al.* had reported similar behavior with disordered c-SiNWs, noting enhanced absorption in the visible and near infrared (IR) spectrum from c-SiNW structures coated with ~20 nm of a-Si:H thin-film compared to c-SiNW structures without the thin-film coating [13]. An increase in the optical absorption of the 3-D hybrid nanowire device structures indicates that the NWSCs would experience an increase in the generation of charge carriers, which can be quantified through electrical measurements of the devices.

5.2.2 Electrical Characteristics of the Solar Cell Devices

I-V measurements were used to determine the effect of light scattering from the disordered hybrid NWSC array. The hybrid 3-D solar cell generated an average J_{SC} of 11.9 mA/cm^2 compared to 10.6 mA/cm^2 obtained for the planar solar cell device as depicted in Figure

33 and tabulated in Table 4. The 12.3% increase in J_{SC} for the hybrid NWSC array compared to the planar solar cell is attributed to the enhanced light absorption throughout the visible spectrum measured, from 300 nm – 800 nm.

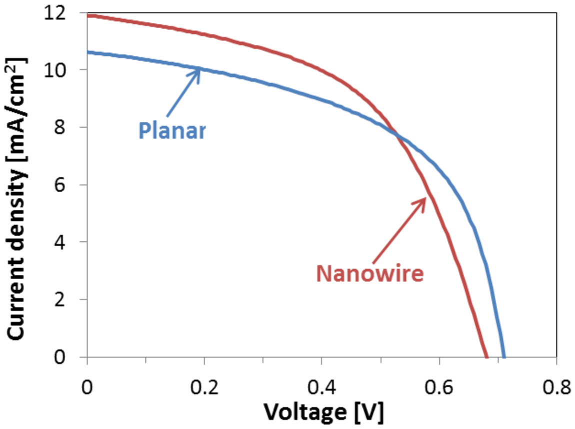

Figure 33. I-V characteristics of planar and 3-D hybrid NWSC devices.

Table 4. Electrical characteristics of planar and hybrid NWSC devices.

	J_{SC} [mA/cm^2]	V_{OC} [mV]	FF [%]	PCE [%]	R_{series} [$\Omega\cdot$cm^2]	R_{shunt} [$\Omega\cdot$cm^2]
Planar solar cell	**10.6**	**708**	**54**	**4.1**	**9.1**	**386**
Hybrid NWSC array	**11.9**	**683**	**52**	**4.3**	**13.9**	**347**

While the hybrid NWSC array showed enhanced optical absorption and higher PCE due to the increase in J_{SC} compared to the planar solar cell, a slight decrease in FF to 52% was detected from the hybrid cell due to a high R_{series} and low R_{shunt} of 13.88 $\Omega\cdot\text{cm}^2$ and 347.3 $\Omega\cdot\text{cm}^2$, respectively. Furthermore, the diodes' dark I-V characteristics at reverse bias were measured from which the ideality factor, *n*, and saturation current density, J_0, were calculated. Extracted *n* was 2.73 for the hybrid NWSC compared to 1.4 for the planar solar cell, while J_0 increased from 1×10^{-15} A/cm^2 for the planar cell to 9×10^{-9} A/cm^2 for the hybrid nanowire device. These non-ideal electrical characteristics achieved from the hybrid NWSC device suggest very high carrier recombination from the 3-D structures. A closer look at SEM micrographs of the hybrid NWSC arrays indicated a potential reason for the limited device performance: non-conformal top electrodes.

Figure 34 shows an SEM micrograph that depicts the discontinuity of the sputter-coated AZO thin-film top electrode on a hybrid NWSC array. Since the sputter-coating method is a PVD process that depends on a line of sight deposition, nanowires that overshadow neighbouring wires may cause the discontinuous sputter-coating of thin-film. Two issues arise from the poor TCO coverage that may contribute to degraded device performance:

1. Exposure of the underlying p^+ a-Si:H semiconductor surface and,
2. Poor charge collection.

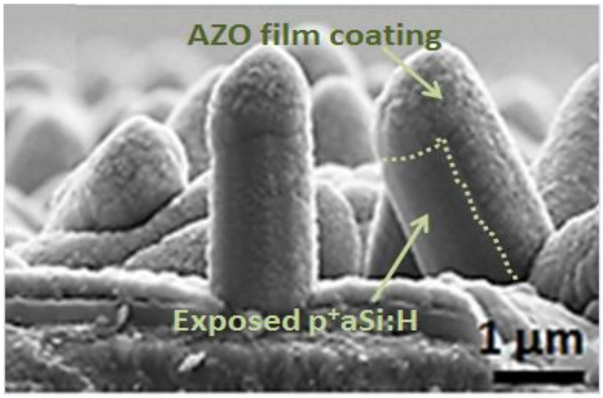

Figure 34. Discontinuity of the top AZO thin-film electrode sputter-coated on the 3-D NWSCs.

By exposing the underlying p^+ a-Si:H surface to air, a native oxide on the p^+ layer may form with time, increasing the number of surface trap states and resulting in increased carrier recombination, which has resulted in the degraded J_0, n, and R_{shunt} calculated from the NWSCs.

Moreover, the discontinuity of the top AZO thin-film results in poor collection of the generated charge carriers within the 3-D nanowire array and therefore, limit J_{SC} and increase

R_{series}, further degrading the FF. With these issues, the optical advantages achieved would be futile for the limited electrical enhancements gained from the 3-D solar cell devices. Thus, it is imperative to determine methods to overcome the current discontinuous deposition of the sputter-coated AZO thin-film top electrode on the 3-D device structures.

Two alternate approaches were investigated to improve the coverage of the top contact onto the disordered hybrid devices. One method deposited 80 nm of ITO thin-film on the hybrid devices via sputter-coating by rotating the substrate during the entire deposition process to minimize the shadowing effect and reach all areas of the disordered nanowire array. Electrical characteristics obtained from the hybrid NWSC arrays whose top contacts were deposited in this way showed reduced R_{series} ($5.59\ \Omega\cdot cm^2$) and n (2.11) compared to TCOs deposited with stationary substrate and target, resulting in an increase in FF (55%), J_{SC} ($13.2\ mA/cm^2$), and PCE (4.6%). However, SEM micrographs of the devices showed top electrode non-uniformity with areas of uncovered regions on the NWSCs.

5.2.3 Addition of ITO nanoparticles as Top Electrode

In order to alleviate the poor thin-film coverage of the sputter-coated TCOs, a composite film was considered, which was fabricated with 80 nm of sputter-coated AZO thin-film followed by spin-coating a suspension of ITO nanoparticles dispersed in ethanol (VP ITO TC8 DE, Evonik) at 500 rpm for 1 minute and curing the layer for 1 hour at 120ºC for a uniform top electrode coverage on the 3-D devices as illustrated in Figure 35.

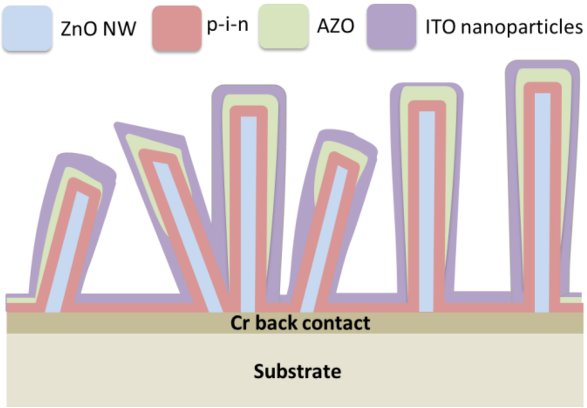

Figure 35. Schematic diagram of the 3-D solar cells with the composite AZO/ITO nanoparticle layer.

The thickness of the composite layer was decreased to maximize the conformal coating on the disordered 3-D nanowire array to retain the 3-D morphology of the solar cell devices. The concentration (by volume) of ITO nanoparticles was decreased by diluting the solution with ethanol. Figure 36 depicts the changes that were observed when the concentration of ITO nanoparticles was decreased from (a) 95% to (b) 80%, (c) 60%, (d) 40%, (e) 20%, and (f) 0% (i.e. all ethanol).

With a concentration of 95% to 60% ITO nanoparticles in ethanol, the film completely embedded the NWSCs with only the tips of the nanowires observed protruding from the layer (Figure 36 (a) to (c)). At 40% ITO nanoparticle concentration, the 3-D structure of the NWSCs was observed, indicating a more conformal coverage (Figure 36 (d)). Decreasing the concentration of ITO nanoparticles to less than 40% showed gaps in the film (Figure 36 (e)), indicating that the electrical contact was too thin for the nanowire array. Furthermore, I-V characterization of the hybrid nanowire devices with the composite film at this concentration showed a 15% decrease in FF due to a lower R_{shunt} and increased R_{series}, indicating poor contact of the top electrode. Therefore, the ITO nanoparticle concentration in ethanol was increased to 40% and a ~ 80 nm thick film was deposited by spin-coating the liquid suspension over the NWSC devices followed by a wet etch and anneal treatment at 120°C for 1 hour to form a blanket transparent electrode whose optical transmittance and reflectance data are presented along with that of AZO and the ITO nanoparticle film alone in Figure 37 (b). The average transmittance between 400 nm and 800 nm were 92.8%, 86.8%, and 87.0% for the ITO nanoparticle layer, AZO, and composite AZO/ITO nanoparticle layer, respectively, with an optical reflectance of up to 10% near 470 nm for the composite film.

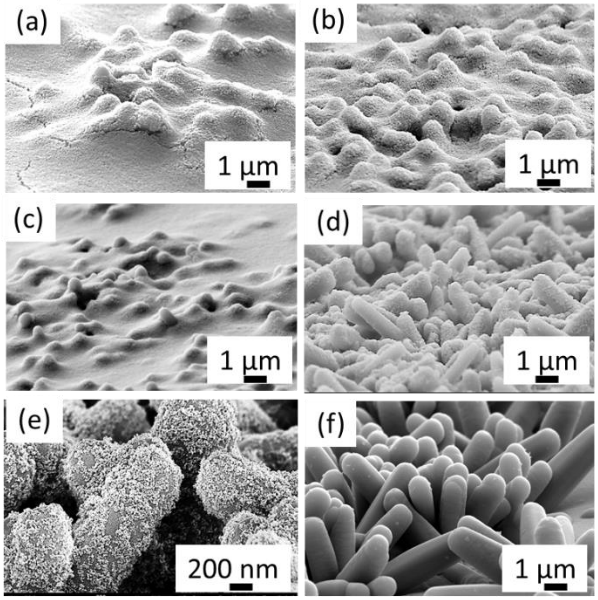

Figure 36. Hybrid nanowire solar cells coated with (a) 95% to (b) 80%, (c) 60%, (d) 40%, (e) 20%, and (f) 0% ITO nanoparticles in ethanol.

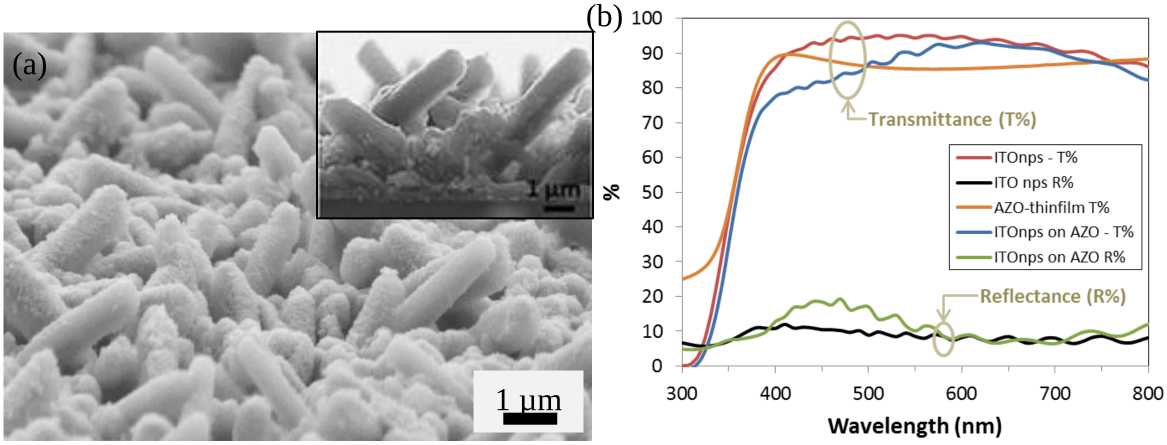

Figure 37. (a) Tilted SEM image of composite AZO/ITO nanoparticle layer showing conformal coverage over the nanowire structures; inset: cross-section SEM image of composite layer coated on NWSCs and (b) optical characteristics of ITO nanoparticle film, AZO film, and composite layer.

5.2.3.1 Device Characteristics with AZO/ITO Nanoparticle Composite Top Electrode

The optical properties of the hybrid 3-D devices with the composite layer were obtained to determine the effect of this layer on the light scattering properties of the nanowire network. Here too was the transmittance measurements from the device structures ~ 0% due to the Cr back electrode deposited under the thin-film structure and thus, a direct correlation between suppressed reflectance and enhanced absorption was measured. Optical reflectance spectra of the hybrid nanowire device structure with sputter-coated AZO thin-film and a similar device structure with the composite film were measured as depicted in Figure 38. For comparison, the reflectance spectrum of a planar reference solar cell structure has also been added. Compared to the planar structure, both hybrid nanowire devices show greatly suppressed reflectance across the visible spectrum. The device structure with the nanoparticle composite film shows more interference peaks than the device structure with only AZO thin-film. This increase in the number of interference peaks is due to the blanket coating of the nanoparticle composite film as observed from the SEM images in Figure 37, which slightly reduces the 3-D morphology of the nanowire network, resulting in some constructive and destructive light interference within the nanowire network.

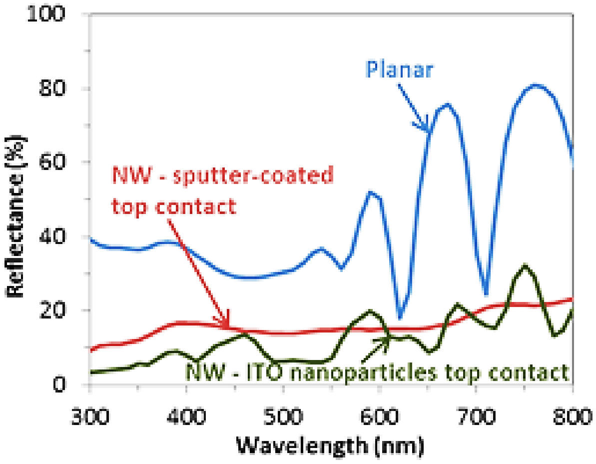

Figure 38. Optical reflectance measurements of planar solar cell and hybrid nanowire/thin-film device structures coated with and without the ITO nanoparticles top contact.

I-V characteristics revealed that improved electrical contact was achieved with the ITO nanoparticle film. The J_{SC} of the 2 µm in height hybrid nanowire devices with the nanoparticle composite electrode increased to 13.7 mA/cm^2; a 15% improvement compared to the hybrid cells with only sputtered thin-film contacts and a 22% improvement compared to the planar cell, resulting in an overall PCE of 6.5% in the best case. Comparing the nanoparticle composite electrode to the sputtered AZO thin-film contacts alone, a drop in series resistance from 13.88 Ω·cm^2 to 1.41 Ω·cm^2 and an increase in the shunt resistance from 347 Ω·cm^2 to 474 Ω·cm^2 were achieved, raising the FF from 52% to 69% as shown in Figure 39 and tabulated in Table 5; the highest electrical characteristics achieved for either planar and nanowire devices. However, a slight degradation in V_{OC} compared to the planar cell persisted in the hybrid cells, where greater carrier recombination is anticipated due to an increased density of interface states along the length of the radial junction hybrid cell compared to the planar cell [31]. Together with a separate set of disordered hybrid NWSCs with average heights of 5 µm indicated that decreasing R_{shunt} results as a function of increasing nanowire height. The dark I-V characteristics obtained at reverse bias of the 5 µm long NWSCs also showed increased current (Figure 40), indicating greater leakage occurring from the longer hybrid NWSC devices. Although the diameter ranges of the ZnO nanowires tend to change by ~ 2× with respect to the seed layer used as shown in Figures 18 and 20 and tabulated in Table 3 (~ 60±14 nm diameter for ZnO nanowires grown on 27 nm thin-film and 130±20 nm diameter of nanowires grown on ZnO nanoparticles), these sets of diameters are still within the same range and thus, a major change to the device performance is not observed. The nanowire separation between neighboring nanowires and height are more important here because these parameters are directly associated to the interface states and thus defect density of the NWSCs fabricated as pointed to above and in Figure 40.

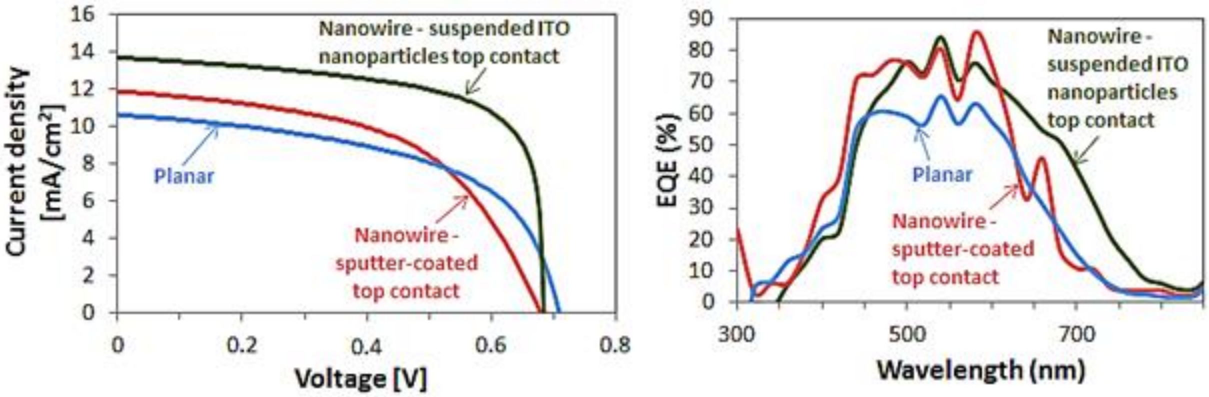

Figure 39. (a) I-V measurements and (b) EQE characteristics obtained of the different solar cell structures [33]**.**

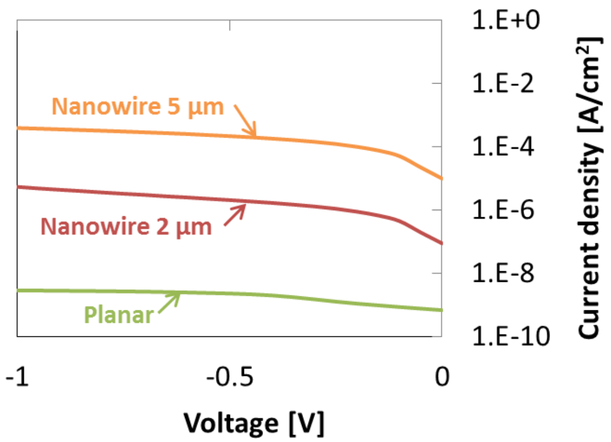

Figure 40. Dark reverse-biased I-V characteristics of the different structured solar cells.

As shown in Figure 37 (b), light transmission through the ITO nanoparticle film over an underlying AZO thin-film layer was attenuated by approximately 6.7% between 400 nm – 620 nm with no attenuation detected in the longer wavelength regime (> 620 nm). This attenuation of higher energy light correlated to a decrease in the EQE response for the nanoparticle-coated hybrid cells compared to the sputter-coated devices with only AZO thin-film or ITO thin-film (Figure 39 (b)). For the longer wavelength light (> 620 nm), improved EQE performance was observed due to increased transmission of the lower energy light through the TCO layer, resulting in increased light scattering and optical absorption by the hybrid nanowire devices.

Table 5. Highest performance characteristics of planar and hybrid nanowire solar cell devices.

	J_{SC} [mA/cm^2]	V_{OC} [mV]	FF [%]	PCE [%]
Planar	**10.6**	**708**	**54**	**4.1**
Nanowire: sputter-coated AZO top electrode	**11.9**	**683**	**52**	**4.3**
Nanowire: AZO/ITO nanoparticle composite top electrode	**13.7**	**683**	**69**	**6.5**

Most of the advantages in light trapping and photo-carrier collection are at the long wavelength light (> 600 nm) by the high density 3-D nanowires while at shorter-wavelengths (< 450 nm), a near-one-to-one relationship exists in enhancement of carrier collection in the nanowire array as observed in the EQE spectra depicted in Figure 39.

5.2.4 Performance Optimization of Hybrid Nanowire Devices

To further enhance the optical and electrical characteristics of the hybrid NWSC devices ZnO nanowire heights and densities were studied. Conditions of these parameters that produced highest optical absorption and highest electrical performance from the NWSC array were considered optimal and used for all subsequent 3-D solar cell fabrication.

5.2.4.1 Performance Changes of NWSCs based on ZnO Nanowire Heights

Numerical simulations of periodic Si NWs have shown that increasing the height of the nanowires can help enhance light absorption within the solar cell device by increasing chances of trapping low energy light rays more efficiently [11]. Figure 41 depicts optical reflectance measurements obtained from arrays of NWSCs that possess average heights between 6 µm and 600 nm. These reflectance spectra indicate that increasing the nanowire heights decreases the optical reflectance due to the increased ability to trap incoming light more effectively. The average reflectance obtained for a 600 nm nanowire array was 22.4%, decreasing to 4.6% for a 6 µm long nanowire array. Because the optical transmittance of the NWSC array is ~ 0%, the results indicate increasing absorption of the incoming light as the nanowires increase in height. As the NWSC height increases, interference peaks are quenched in corresponding reflectance spectra, indicating strong light trapping within the NWSC array.

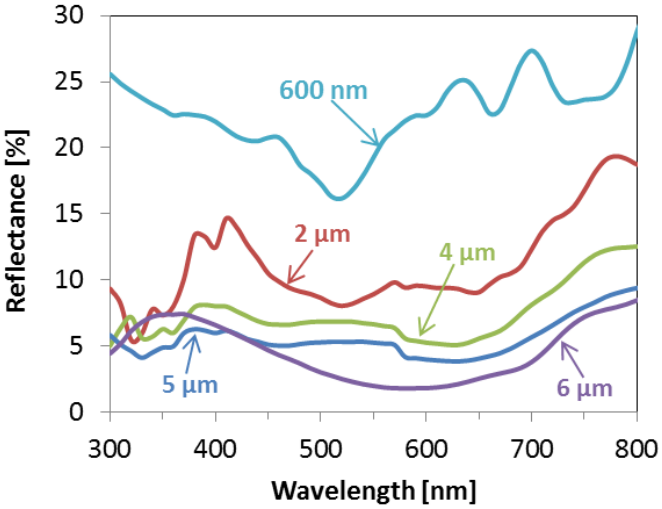

Figure 41. Reflectance measurements of hybrid NWSCs labeled with different average heights.

The NWSC arrays of varied heights were electrically characterized and are depicted in Figure 42. Although the larger height NWSC arrays showed greatly suppressed optical reflectance (Figure 41), their corresponding electrical characteristics had degraded. The V_{OC} and FF of the NWSCs steadily decreased although, up to 2% of an increase in J_{SC} was observed in the 4 µm and 5 µm long NWSC arrays compared to that of the 2 µm long NWSC array. The degraded V_{OC} and FF are caused by the increased interface states that exist in the larger aspect ratio NWSCs (similar to what was observed between the planar cells and the 2 µm height NWSCs). The increased J_{SC} observed initially in the 4 µm and 5 µm height NWSC arrays is due to the improved light trapping that resulted in enhanced carrier generation, which was efficiently collected; however, further increasing the heights to 6 µm, significantly affected the carrier extraction efficiency to also hinder any achievable improvements in J_{SC} from the 6 µm height 3-D NWSCs, which showed greatly degraded V_{OC} and FF to ~ 275 mV and 30%, respectively, and severely degrading the carrier collection efficiency. Thus, although 6 µm long NWSCs showed lowest optical reflectance, their poor electrical characteristics deemed the larger height NWSCs unsuitable for solar cell devices. The 2 µm long NWSCs showed highest PCE values, obtaining 4.5% on average (from 42 devices) with the largest cells achieving PCE ~ 6.5%.

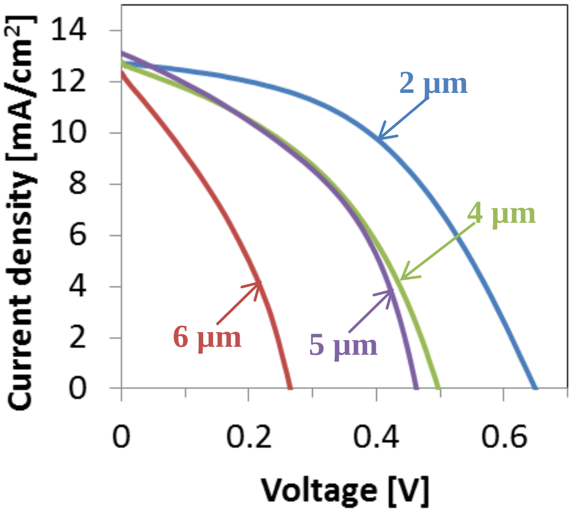

Figure 42. I-V characteristics of NWSCs of varied lengths.

5.2.4.2 Performance Changes of NWSCs based on ZnO Nanowire Density

The density of NWSCs was also altered to assess the optical and electrical effects the parameter would have on the 3-D solar cell characteristics. The NWSC density was altered by adjusting the amount of ZnO nanoparticles spun-coated on the substrate by repeating the spin-coating process to add more nanoparticles. Grown nanowire densities were calculated from SEM micrographs of bare ZnO nanowires using a post-processing image analyzer (ImageJ), which converts the micrographs into white/black-contrast pixelated images (white for the nanowires, black for the background), whose white areas are quantified and divided from the total area of the micrograph to generate a density calculation. Figure 43 (a) depicts the optical reflectance obtained from each of the NWSC arrays with varied densities while Figure 43 (b) depicts corresponding I-V characteristics obtained from the NWSC arrays. Increasing the NWSC densities up to approximately 4×10^8 cm^{-2} showed to further suppress the optical reflectance from ~ 27% to 8% between 300 and 800 nm from the NWSC arrays. However, as the NWSC density increased to 2×10^9 cm^{-2}, the reflectance spectrum moved upward again with increasing long wavelength interference peaks observed, too. At this density, the ZnO nanowires were so dense that the a-Si:H thin-film that was coated over the wires encapsulated the wires and continued to deposit over the wires, similar to the hybrid textured diodes discussed in Chapters 2 and 4. Thus, the incoming light was poorly coupled in the device at the very high nanowire density (2×10^9 cm^{-2}); thus, an optimum ZnO nanowire density exists in suppressing the optical reflectance, which was 4×10^8 cm^{-2} from the disordered NWSCs obtained in these experiments. Despite the suppressed optical reflectance at 4×10^8 cm^{-2}, I-V characteristics of the NWSCs were negatively impacted by the degraded V_{OC}; the increased nanowire density increased the interface states within the array, resulting in increased shunting as shown in Figure 43 (b).

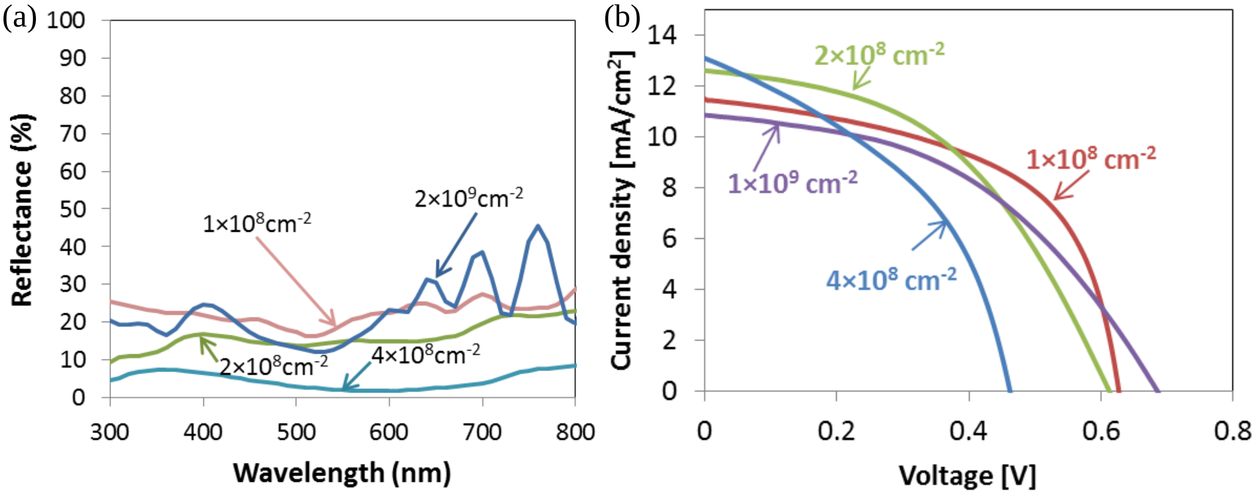

Figure 43. (a) Reflectance spectra and (b) I-V characteristics of hybrid NWSCs with different nanowire densities.

These experimental results indicate that light absorption can be controlled by changing average nanowire heights and densities. By increasing the nanowire height, light absorption was enhanced and led to an increased J_{SC} of up to ~ 14 mA/cm^2 until the device V_{OC} and FF significantly degraded. Increasing the nanowire density in the array also degraded the V_{OC} and FF but, helped to increase optical light absorption within the nanowire array. This increase in light absorption with a dense nanowire array occurred until the 3-D morphology of the NWSCs did not exist (i.e. when a thin-film textured structure formed). Thus, the optimum nanowire height and density under the process conditions used to gain highest optical and electrical characteristics of the hybrid devices were ~ 2 μm and ~2×10^8 cm^{-2}, respectively.

To estimate the *effective* thickness of the intrinsic a-Si:H thin-film, d, that the hybrid NWSC devices (2 μm height and 2×10^8 cm^{-2} density) possess from strong light trapping, their values were calculated and compared with that of the planar cell by fitting experimental I-V characteristics at reverse bias to the Hecht formula [94]:

$$\frac{\mathrm{I_{ph}}}{\mathrm{I_{sat}}}=\left(\frac{\mu\tau \mathrm{V_b}}{\mathrm{d}^2}\right)\left[1\text{-exp}\left(\frac{\text{-}\mathrm{d}^2}{\mu\tau \mathrm{V_b}}\right)\right], \quad (9)$$

where $V_b \approx V + V_{OC}$ where V is the applied bias, $\mathrm{I_{ph}}$ is the photocurrent, $\mathrm{I_{sat}}$ is the saturation current density, d is the absorber layer thickness, and $\mu\tau$ is the mobility-lifetime parameter of a carrier generated in the diode. The Hecht model also helps understand the defect density within the device as the defect density is inversely proportional to $\mu\tau$. Extracted photoconductivity plots in reverse bias are depicted in Figure 44 for the planar and hybrid NWSCs consisting of different thicknesses of intrinsic a-Si:H thin-film. Figure 44 compares the photocurrent obtained for 300 nm thick a-Si:H deposited in a planar solar cell and a NWSC array as well as the photoconductivity of 900 nm a-Si:H film in a planar cell and NWSC array. The Hecht model was fitted to the plots obtained from experimental results of the planar and NWSC devices. By fitting the theoretical plot to the experimental one achieved, values for the parameters such as $\mu\tau$ and an *effective* d for the NWSCs were found. Resulting d from the planar solar cells remained at the deposited values (i.e. 300 nm and 900 nm) while the *effective* d of the intrinsic a-Si:H film from the NWSC array was 1.35 μm despite an actual deposition of 300 nm of a-Si:H over the 3-D devices. This effective thickness of the absorber layer in the NWSCs is due to the enhancement in light trapping that the 3-D array generates, leading to a significant impact on the carriers generated within the cell.

The minority carrier mobility-lifetime product, $\mu\tau$, was also extracted from the Hecht model by fitting the theoretical plot to the experimental one achieved in order to characterize the defect density in the devices. The $\mu\tau$ is inversely proportional to the defect density because a highly defective a-Si:H film consists of dangling bonds, which act as trap states that would lower the carrier mobility and quench the carriers much faster. The $\mu\tau$ achieved for a planar solar cell with 300 nm intrinsic a-Si:H thin-film was 6.2×10^{-9} cm^2/V while that for a 900 nm thick planar a-Si:H solar cell was within the same range of ~ 2.2×10^{-9} cm^2/V. Street *et al.* reported similar $\mu\tau$ values obtained from their low-temperature fabricated planar a-Si:H p-i-n diodes of similar ideality factors of $n = 1.5$ [45]. The hybrid NWSC array with an effective thickness of 1.35 μm a-Si:H, possessed a $\mu\tau \approx 1.2\times10^{-8}$ cm^2/V; however, if the light trapping enhancement factor was not considered in the calculations and the NWSCs were considered as just planar film, $\mu\tau \approx$

6.0×10^{-11} cm^2/V, indicating ~ 2-3 orders of magnitude greater defect density than the 300 nm and 900 nm thick a-Si:H planar solar cells.

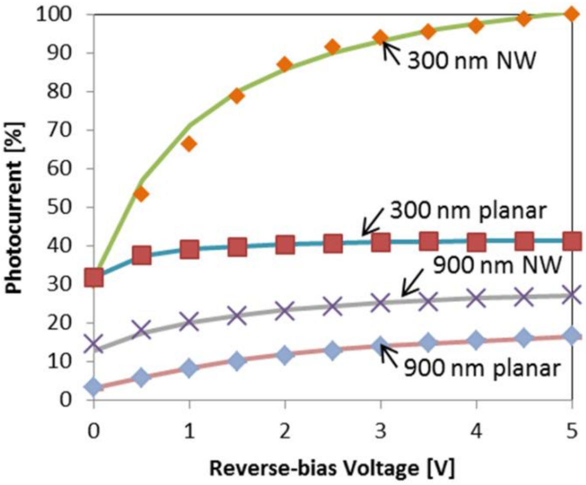

Figure 44. Photocurrent measurements obtained at reverse-bias and fitted to the Hecht formula for NWSCs and planar cells with 300 nm and 900 nm absorber film. The lines of each curve are fitted using the Hecht model and the points along the curves represent experimental measurements.

To further assess the defect density of the a-Si:H thin-film solar cells, transient dark current measurements of the planar cells and NWSCs were obtained at reverse bias. Figure 45 depicts spectra at varying bias conditions for (a) planar solar cell and (b) NWSC devices. In the planar solar cell, the dark current decreases monotonically at low bias. Above 2 V however, the dark current gradually increases with time. The dark current is proportional to the defect density, increasing with bias. Street *et al.* suggest that two mechanisms are responsible for the different behaviour that occurs at different bias conditions: namely, decrease in thermal generation at the deep defect states in the a-Si:H film and injection by tunnelling through the barrier between p^+-i and i-n^+ interfaces [45]. Initially at low bias voltages, the charge carriers trap in localized deep defect states in a highly defective a-Si:H film. By increasing the voltage (in this case > 2 V), the depleted carriers at the deep states are injected back and tunnel through the barrier width. The increased defect density results in a narrower barrier width, making it easier for carriers to be injected and thus, from 2 V to 3 V bias conditions, the change between decreasing and increasing dark current are observed, respectively. This change in the dark current is sometimes noted in the same spectrum but, was not found in the fabricated planar devices. This behaviour in the dark current was observed in the NWSC devices that were biased at 4 V (Figure 45 (b)); initially, the dark current steadily decreased but, after 40s at 4 V bias, a slight increase in current was detected; after this point, even more dark current was measured at the same bias condition, indicating continuous trapping and de-trapping occurring at the defect states in the a-Si:H thin-film.

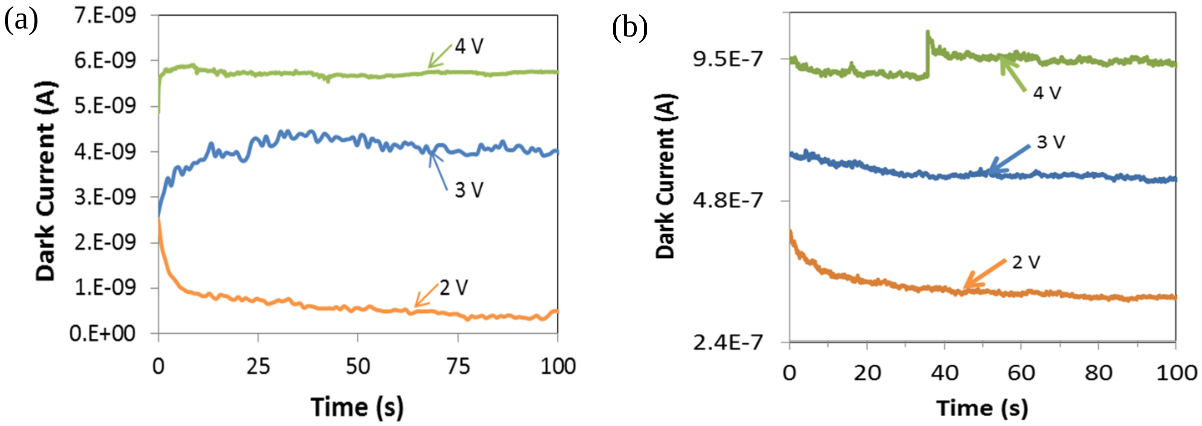

Figure 45. Transient measurements at different reverse bias dark conditions obtained for (a) planar solar cell and (b) NWSC devices.

The thermal dark current at 2V when the i-layer is fully depleted is ~ 3.5×10^{-10} A/cm^2 and ~ 1.8×10^{-6} A/cm^2 for the planar and NWSC devices, respectively. Using these measurements, the defect density was calculated using,

$$J_{th} = \frac{Q_{Dep} kTAd}{\Delta E_F \tau_D}, \qquad (10)$$

where A is the area of the device, d the thickness of the i-layer, τ_D lifetime of the minority carriers, kT the thermal energy at room temperature, and Q_{Dep} the depleted charge from the i-layer ($\frac{Q_{Dep}}{q\Delta E_F} = N(E_F)$; $N(E_F)$ is the density of defect states near E_F). The calculated defect density was ~ 2.0×10^{19} cm^{-3}eV^{-1} and 1.2×10^{22} cm^{-3}eV^{-1} for the planar and NWSC devices, respectively. The large defect density values calculated for these devices are due to the increased thermal dark currents obtained, likely due to the unpassivated nature of the devices. These results indicate that the defect density in the NWSCs is increased by 3 orders of magnitude compared to that of the planar thin-film, resulting in the ~100 mV lower V_{OC} in the NWSCs than the planar cells under AM 1.5G illumination.

Despite these conditions of greater defect density, which have resulted in reducing the V_{OC} of the 3-D devices, the NWSC array have generated greater photocurrent to increase the total J_{SC} from the 3-D devices. This electrical effect is due to the larger surface area of the 3-D devices while maintaining a large drift length ($L_{\text{drift}} = \mu\tau E$; E is the electric field) of ~ 333 nm within the cell; because of the 3-D effect, the amount of charge generated within the NWSC array is much greater than that from a planar cell. Therefore, despite the increased interface states, which result in an increased defect density by 3 orders of magnitude, the contribution of photocurrent obtained from the hybrid NWSCs is still ~ 36% greater than that obtained from the planar a-Si:H solar cells, resulting in a superior optical and electrical performance device structure.

5.2.5 Limitations of ITO nanoparticles for Solar Cell Devices

Although the top AZO/ITO nanoparticle composite layer has shown to provide improved contact to the 3-D nanostructures compared to sputter-coated AZO thin-film alone, the ITO nanoparticle film tended to be similarly brittle as the AZO thin-film. The composite film easily cracked and delaminated from the substrate surface during handling. This poses an issue for flexible electronics as the brittleness of the top electrode would affect the ability to bend the devices without negatively affecting device functionality and performance. Thus, a different top electrode is required for the flexible 3-D solar cells and is discussed in the following chapter.

In summary, disordered ZnO nanowire arrays were conformally coated with a-Si:H p-i-n thin-film to form radial junction 3-D NWSC arrayed devices. The combination of the light scattering enhancement due to the 3-D hybrid structures and an improved conformal coverage of the top transparent contact resulted in a highest PCE of 6.5% on glass substrates. The results reported here demonstrate the feasibility of integrating randomly ordered nanomaterials with amorphous thin-films to form efficient 3-D photovoltaic device structures.

Chapter 6

Hybrid Nanowire Solar Cell Top Electrode Enhancements using Ag Nanowires

Chapter 5 identified key issues related to poor sputter-coating of the top electrode on disordered 3-D NWSCs. Since developing flexible and conformal TCO electrodes is difficult with conventional PVD techniques such as sputtering due to shadowing effects from the neighbouring nanowires, an alternative method was investigated, in which an ITO nanoparticle layer was coated over the discontinuous AZO thin-film to create an AZO/ITO nanoparticle composite layer. However, its limited ability to remain contiguous under mechanical strain has made it difficult to fabricate reliable flexible electrodes.

This chapter furthers the discussion by providing another alternative solution, which uses silver nanowires (Ag NWs) to address the discontinuity with the sputter-coated AZO thin-film and improve the flexibility of the top contact. Section 6.1 introduces Ag NWs that have been used in solar cells as a viable transparent, conductive, and conformal electrode layer by others. After a discussion in Section 6.2 of the materials properties of the Ag NWs used in this research, device characteristics are further analyzed in Section 6.3, which includes both rigid and flexible nanowire solar cell devices.

6.1 Ag NWs as the Top Electrode of 3-D Solar Cell Devices

Ag NWs have gained considerable interest due to their high optical transparency in the visible spectrum, low R_{sheet} (< 40 Ω/sq.), mechanical flexibility, and potential for enabling simple process integration [95]–[99]. They have been seen in the past few years as a viable alternative to conventional ITO thin-films due to the associated increased costs with the latter and the scarcity of indium. Since they possess similar electrical characteristics to sputter-coated ITO thin-films, Ag NWs have already been employed as an alternative electrode in planar organic [95], [99], [100] and inorganic [101], [102] devices. Their application in 3-D device structures, however, has been far more limited. A flexible Ag NW top electrode for 3-D c-Si NWSCs was reported [36] but, only meagre PCEs (2.8%), FF (55.5%), and J_{SC} (4.5 mA/cm^2) were achieved. Due to poor wetting of Ag NWs on the Si, the authors used Ni nanoparticles, which generated R_{series} of 14 $\Omega\cdot\text{cm}^2$.

Additionally, poor contact with the hybrid NWSC devices was observed when Ag NWs were coated directly over the a-Si:H devices without the sputter-coated AZO. Thus, to improve the contact between the top electrode and the NWSCs, sputter-coating AZO thin-film over the 3-D devices was continued with the Ag NWs coated after, as depicted in Figure 46, forming an AZO/Ag NW composite top electrode. The composite layer maintained > 85% optical transparency and similar R_{sheet} when compared to AZO thin-film alone. The composite electrode assists in the collection of carriers that would otherwise trap and recombine in areas that are poorly sputter-coated with AZO thin-film. Given the relatively low melting point of Ag NWs (T_m ~ 190ºC) compared to the bulk (T_m = 960ºC), a low temperature anneal was used to allow the metallic nanowire layer to soften and consequently coat the sidewalls of the disordered 3-D solar cell array more conformally to efficiently collect minority charge carriers generated in the 3-D devices [98].

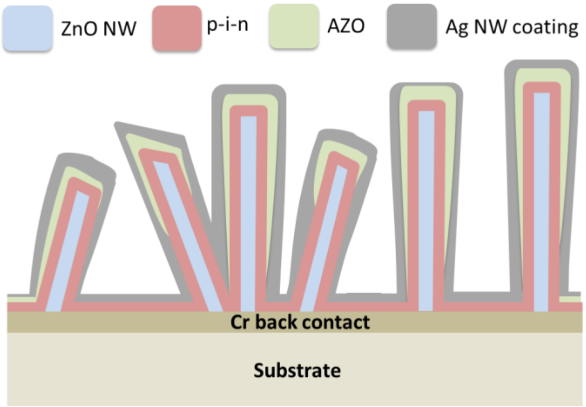

Figure 46. Schematic diagram of the 3-D hybrid NWSCs with Ag NWs.

6.2 Ag NW Material Characteristics

The Ag NWs used were 10 mg/mL (10 µm length, 35 nm diameter) in ethanol (Blue Nano Inc). To control the optical and electrical properties of the material, the Ag NWs were diluted with ethanol to achieve 4 mg/mL concentrated Ag NWs per layer. The Ag NW layers were increased by adding multiple coatings onto the AZO surface using the Mayer rod coating technique [103]–[105]. SEM images revealed that the 3-D device structures remained intact with no observable structural degradation after the coating process. The devices were subsequently annealed for 1 hour between 120ºC to 240ºC. Here, NWSCs with an 80 nm thick sputter-coated AZO top electrode only (i.e. without Ag NWs) were used as reference cells.

In order to improve the coverage of the top electrode, multiple coatings of Ag NWs were applied on the surface. However, to also maintain high transparency, an optimal amount of Ag NW coatings is required. Thus, the coatings were dispersed on separate glass substrates, annealed at 200ºC for 1 hour and subsequently measured for both optical transmittance and R_{sheet} prior to coating the 3-D devices. Figure 47 shows the optical transmittance from 390 nm to 800 nm for multiple coatings of Ag NWs, and an 80 nm thick AZO film. The amount of Ag NWs that covered the surface after each coating cycle was calculated by examining top-down SEM micrographs of the coatings with a post-processing image analyzer (ImageJ) to calculate a percentage of white-to-black pixels covered in the image (Table 6). A 3× increase in Ag NW coverage resulted in an approximately 10% drop in optical transmission and more than 10× decrease in R_{sheet}. Here, a figure of merit, σ_{DC}/σ_{op}, [103] [96], [106] is used to directly compare the Ag NW samples in terms of their optical and electrical characteristics. A high σ_{DC}/σ_{op} corresponds to a condition where the incoming light is minimally obstructed before reaching the underlying layer while also possessing a low R_{sheet}. σ_{DC}/σ_{op} is derived from the Beer-Lambert law, $I_T/I_0 = exp(-\alpha/t)$, where I_T is the transmitted light, I_0 the incident light, α the absorption coefficient and t the thickness of the TCO thin-film in combination with $R_{sheet} = \rho/t$, where ρ is the resistivity of the TCO thin-film. The average optical transmission in the visible spectrum is represented as:

$$T(\lambda_{av}) = \left(1 + \frac{188.5}{R_s}\frac{\sigma_{op}(\lambda_{av})}{\sigma_{DC}}\right)^{-2}. \qquad (11)$$

The σ_{DC}/σ_{op} of the Ag NWs is shown as a function of the number of Ag NW coatings in the inset of Figure 47. The maximum σ_{DC}/σ_{op} was obtained for a Ag NW surface coverage of 23% (i.e. Ag NWs coated 2× on the substrate). Figure 47 depicts the transmittance spectrum of this resulting AZO/Ag NW composite film, which achieved an average transmittance of ~ 85% between 393 nm – 800 nm.

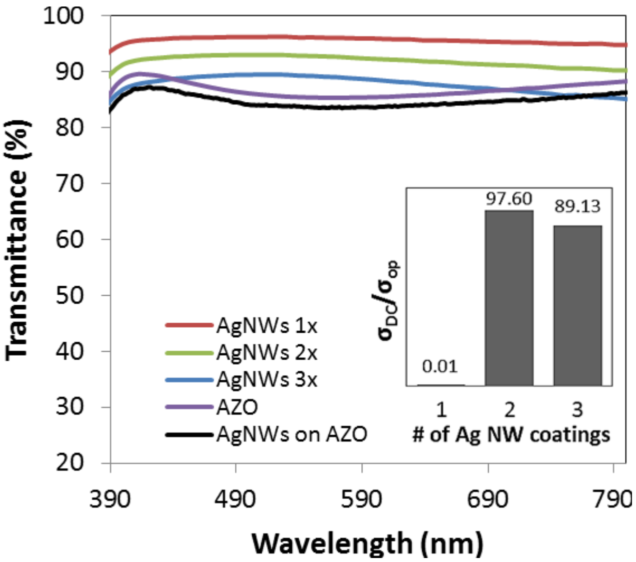

Figure 47. A comparison of the transmittance spectra of Ag NWs with various coating layers, sputter-coated AZO thin-film, and the composite AZO/Ag NW film with Ag NWs coated 2×. Inset: figure of merit of the Ag NWs.

Table 6. Characteristics of the Ag NW coatings, AZO film, and composite film. R_{sheet} was obtained after annealing the samples at 200°C for 1 hr in N_2.

Material	$T_{average}$ [%]	Areal Coverage [%]	R_{sheet} [Ω/sq]
AZO thin-film	87	N/A	25
Ag NWs 1×	95	13	560k
Ag NWs 2×	91	23	40
Ag NWs 3×	86	44	27

When the Ag NWs were coated on the 3-D NWSCs at room temperature, SEM micrographs revealed that the Ag NWs were rigidly positioned on the tips of the 3-D devices. Given the relatively low melting-point temperature (T_m = 190ºC) of the Ag NWs, a low-temperature anneal is expected to soften them, allowing the nanowires to conform to a non-planar and high aspect ratio structure. SEM micrographs in Figure 48 depict the morphological changes of the Ag NWs over the 3-D structures as a function of temperature. At 120ºC, the Ag NWs still appeared as rigid structures spanning only the tips of the NWSC structures. By increasing the temperature to 140ºC, the formerly rigid Ag NWs began to soften and droop allowing the Ag NWs to contact the sidewalls and top surfaces of the NWSC structures. At 200ºC, 10ºC above the melting point temperature, the Ag NW mesh had improved wetting the surface, and formed a conformal Ag thin-film coating over the surface of the 3-D NWSCs. Further increasing the temperature to 240ºC showed the Ag NWs to dewet and agglomerate into small clusters of well-separated islands (inset of Figure 48 (d)) because, the high surface energies of the Ag metal facilitate atomic diffusion with a limited kinetic motion for reconstruction [107], [108]. As a result, disconnected droplets emerged, similar to that observed by Lee *et al*. [95].

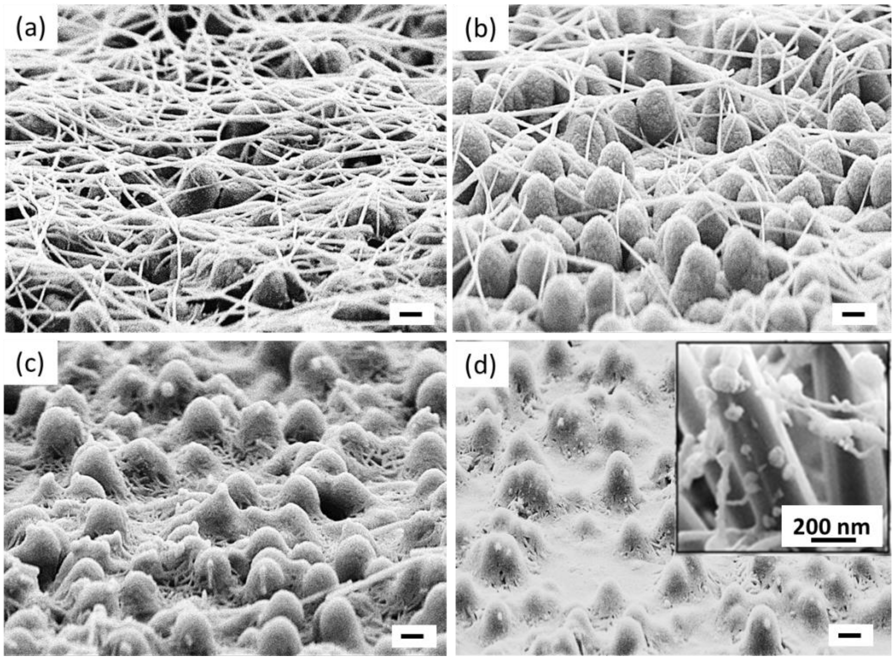

Figure 48. SEM images of Ag NWs coated on 3-D hybrid NWSCs using the same Ag NW coating density (2×) at anneal temperatures of (a) 120ºC, (b) 140ºC, (c) 200ºC, and (d) 240ºC. Inset of (d) shows a magnified SEM image of disconnected droplets of Ag on the sidewall of a 3-D nanowire after the anneal. Unlabeled scale bars are 1 µm.

Changing the morphology by annealing the composite film at different temperatures also affected the film's electrical (contact) performance. The R_{sheet} of the AZO/Ag NW composite film and the corresponding R_{series} from the 3-D NWSC devices with the composite top electrode at each of the anneal temperatures have been plotted in Figure 49. R_{sheet} decreased as a function of increasing temperature with a minimum of 48 Ω/sq. at 200ºC, correlating to the improved coverage on the contacts to increased electrical contact between the nanowires and the AZO film to the underlying NWSC device. The drop in R_{sheet} at elevated temperatures is also due to a sintering process, which reduces junction resistance by improved wetting between overlapping Ag NWs. Both competing phenomena may be cause for the reduced resistance. At 200 ºC, the observed Ag NWs begin to thin their diameter, fragment, and coalesce into separate islands. As the Ag contact dewets from the NWSCs' surface, an increase in R_{sheet} to ~ 250 Ω/sq. at 240ºC is observed.

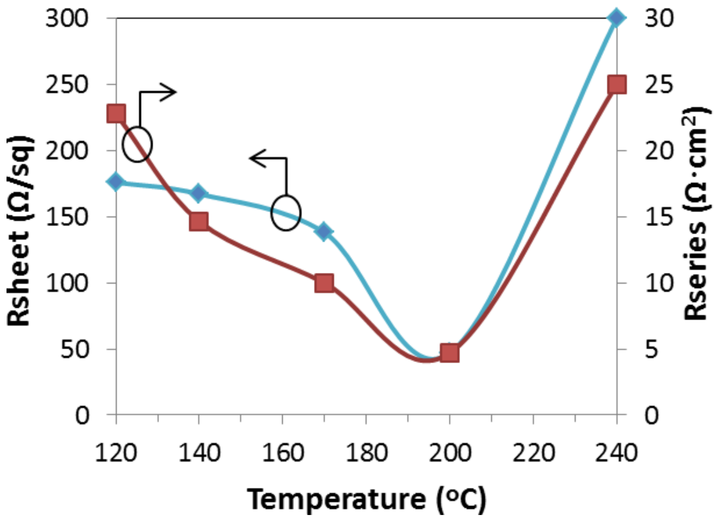

Figure 49. R_{sheet} of the annealed composite AZO/Ag NWs layer and series resistance values of the corresponding 3-D NWSCs with the AZO/Ag NW composite top electrode annealed at different temperatures.

To quantify the enhancements to the performance with the composite layer electrode after annealing, the R_{series} from each of the NWSC devices was extracted after each anneal. The R_{series} of the NWSCs showed similar dependence to the anneal temperature as the R_{sheet} of the composite electrode. A high R_{series} of 22.8 $\Omega\cdot cm^2$ was measured at 120ºC, correlating to the poor R_{sheet} measurements due to the poor physical contact to the 3-D NWSCs. At 140ºC, the R_{series} decreased to 14.6 $\Omega\cdot cm^2$ as a result of the improved conformal coverage of the Ag NWs. At 170ºC, the R_{series} further decreased to 10 $\Omega\cdot cm^2$, as the Ag NWs further wetted onto the NWSCs. R_{series} of 4.7 $\Omega\cdot cm^2$ was achieved at 200ºC due to complete wetting onto the NWSC sidewalls, as shown in Figure 48 (c), covering the regions that may have been uncoated by the sputtered AZO. At 240ºC, the R_{series} increased again to 25 $\Omega\cdot cm^2$, due to the dewetting of the Ag from the NWSC surface, resulting in discontinuous Ag island formation (inset of Figure 48 (d)). Therefore, a post-process thermal anneal at 200ºC was used after coating the Ag NWs over the 3-D NWSCs to form a low-resistance top electrode.

6.3 Hybrid Nanowire Solar Cell Characteristics with AZO/Ag NW Composite Top Electrodes

To ensure that the composite layer has a minimal effect on how the incoming light interacts with the 3-D NWSCs, optical reflectivity measurements were obtained from the devices. Reflectivity spectra are depicted in Figure 50 (a) for each 3-D NWSC structure along with a planar solar cell fabricated with the same p-i-n diode structure and thin-film thicknesses with sputter-coated AZO as the top electrode for comparison. Light absorption within the devices is calculated as $A(\lambda) = I(\lambda) - T(\lambda) - R(\lambda)$ where $A(\lambda)$, $I(\lambda)$, $T(\lambda)$, and $R(\lambda)$ denote total absorption, incoming illumination, transmittance, and reflectance as a function of wavelength, respectively. Since $T(\lambda)$ through the solar cell is negligible due to a 100 nm back Cr electrode deposited under the thin-film layers, measured $R(\lambda)$ indicates a direct loss in light absorption from the device structures. $R(\lambda)$ was suppressed by 4-8% up to 650 nm and again near 850 nm for the NWSCs with the composite top electrode compared to the NWSCs with only AZO top electrodes. This reduction is because the incoming light is scattered by the Ag in the composite electrode as it penetrates through to the 3-D structures and is further scattered by the NWSCs, increasing its path-length for enhanced light absorption in the region.

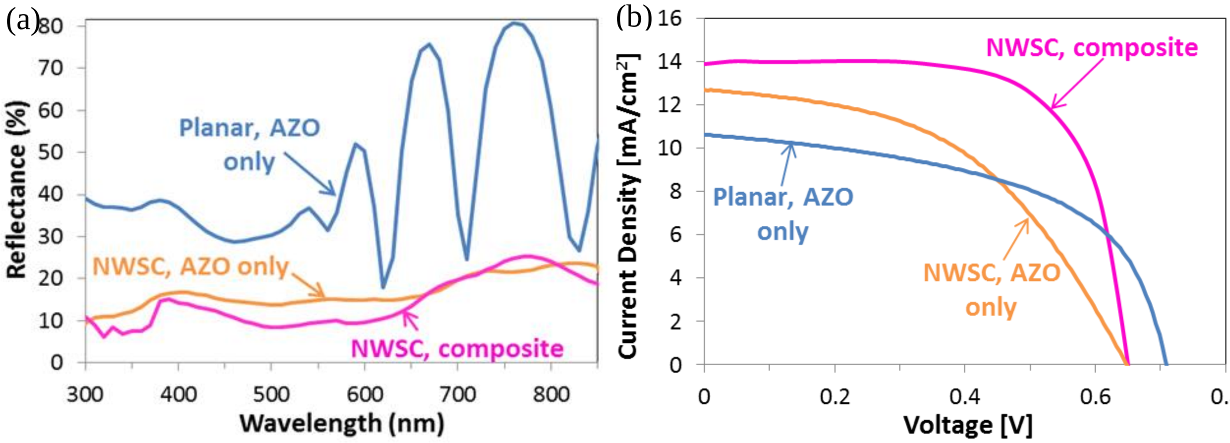

Figure 50. (a) Optical measurements obtained from the device structures on glass substrates. (b) I-V characteristics obtained of each of the devices on glass substrates.

Corresponding to the enhancements measured in the optical absorption from the 3-D devices, the electrical characteristics of the NWSCs with the composite layer showed a gain in the total PCE measured (Figure 50 (b)). Largest total PCE calculated for the NWSCs with the composite top electrode was 6.3% while that for the AZO-only NWSCs was 3.9%, resulting in a PCE enhancement of 62%. To understand the electrical enhancements measured from the devices, the R_{series} and R_{shunt} values were found and are tabulated in Table 7. In comparison, the planar devices and the NWSCs with only AZO top electrodes showed a 48.5% and 74.4% greater R_{series}, respectively, than the NWSCs with the composite top electrode. A similar trend was measured for R_{shunt}, which was 65% and 69% lower for the planar and AZO-only top electrode 3-D devices, respectively, compared to the NWSCs with the composite top electrode. The change is attributed to improved generation and collection of minority charge carriers from the disordered 3-D NWSC structures that are reflected from the higher J_{SC} and FF values.

Table 7. Device characteristics of the NWSC with and without the AZO/Ag NW composite top electrode. Planar device characteristics are also shown for comparison.

	J_{SC} [mA/cm^2]	V_{OC} [mV]	FF [%]	R_{series} [Ω·cm^2]	R_{shunt} [Ω·cm^2]	PCE [%]
Planar – AZO only	**10.6**	**708**	**54**	**9.2**	**386**	**4.1**
NWSC – AZO only	**12.7**	**653**	**47**	**18.4**	**347**	**3.9**
NWSC - composite film	**13.9**	**653**	**69**	**4.7**	**1117**	**6.3**

Comparing device characteristics of the NWSCs fabricated with AZO/ITO nanoparticle top electrodes to the NWSCs fabricated with an AZO/Ag NW composite top electrode, an improvement in the J_{SC} is noted and can be inferred that the enhanced conformal coating of the latter improves the efficiency in collecting charge carriers than the former. Although the FF and highest PCE gained were similar to both NWSC device structures, their R_{series} and R_{shunt} were different. The improved R_{shunt} in the NWSC with AZO/Ag NW top electrode is attributed to the conformal coating, which led to coverage of the 3-D semiconductor structures. The AZO/ITO nanoparticle layer is more rigid than the AZO/Ag NW layer, making it more difficult for the former to reach regions of the disordered NWSC sidewalls that are closer to the substrate base. However, the ~ 50 nm increased thickness of the AZO/ITO nanoparticle layer helped in decreasing its R_{sheet}, which resulted in a lower overall R_{series} of the device. The ~ 30 mV lower V_{OC} in the NWSC with AZO/Ag NW top electrode than of that with the AZO/ITO nanoparticle layer is related to the individual differences in the p-i-n a-Si:H NWSCs between the sampled devices.

6.4 NWSC Characteristics with AZO/Ag NW Composite Electrodes on Flexible Substrates

The conformal and transparent AZO/Ag NW composite electrode was used to fabricate 3-D NWSCs on flexible PEN substrates as depicted in the schematic diagram in Figure 51 (a). A cross-sectional SEM micrograph of the 3-D devices is presented in Figure 51 (b).

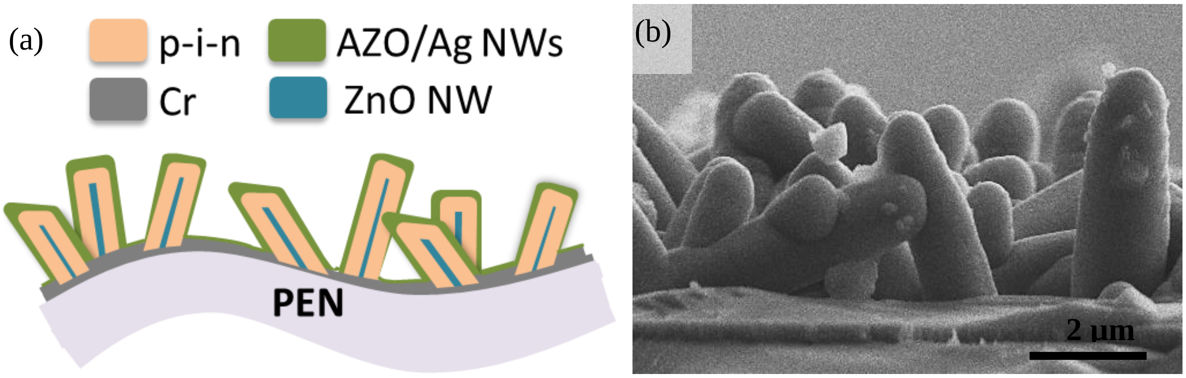

Figure 51. (a) Schematic diagram of NWSCs fabricated directly on PEN substrate and (b) Cross-section SEM image of the NWSCs.

The flexible 3-D device characteristics with AZO/Ag NW top electrodes were compared to the 3-D NWSCs fabricated with the AZO thin-film top electrode and is depicted in Figure 52. Devices that achieved the highest PCE of 5.5% showed J_{SC} values of approximately 13.1 mA/cm^2, similar to that obtained from the NWSCs on glass (Table 8). It is worth noting that these results obtained from the disordered hybrid NWSCs are greater than some of the earlier reports that fabricated crystalline Si NWSCs on flexible substrates [20], [29], [36]. The I-V characteristics presented here of the flexible NWSCs with the AZO/Ag NW composite top electrodes show the feasibility of fabricating 3-D NWSCs on arbitrary substrates.

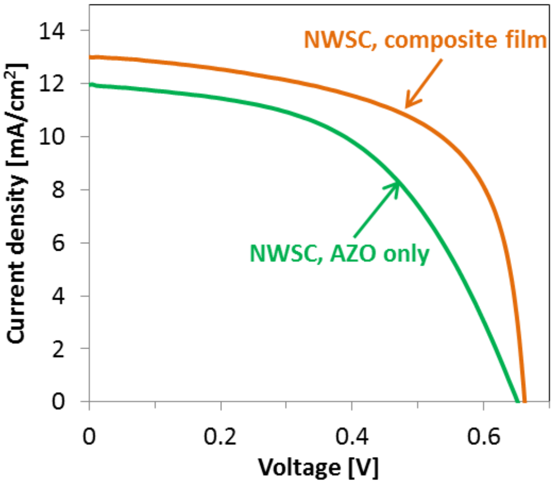

Figure 52. I-V characteristics of flexible 3-D NWSCs with AZO/Ag NW composite top electrode and AZO thin-film only as top electrode.

Table 8. Electrical characteristics of flexible 3-D NWSCs with the AZO/Ag NW composite film electrode and AZO thin-film electrode.

	Jsc [mA/cm^2]	**Voc [mV]**	**FF [%]**	**PCE [%]**
NWSC – AZO only on PEN	12.0	656	51	4.0
NWSC – composite film on PEN	13.1	662	63	5.5

To summarize, a conformal and transparent AZO/Ag NW top electrode was used to improve electrical contact for 3-D NWSCs while maintaining 85% optical transmission. The efficacy of the Ag NW contact was found to be a function of the annealing temperature. An annealing temperature of 200ºC was found to be optimal to conformally coat the 3-D structures and minimize R_{sheet}. Table 9 summarizes the average performance of planar and nanostructured solar cells fabricated to this point.

Table 9. Summary of average performance of 2-D and 3-D thin-film solar cells fabricated.

Solar Cell Type	Substrate	ZnO Nanowire Dimensions [µm]	p/i/n a-Si:H Layer Thicknesses [nm]	J_{SC} [mA/cm^2]	V_{OC} [mV]	FF [%]	PCE [%]
Planar	Glass	N/A	50/300/40	7.0±3	708±100	50±5	2.1±2
Planar	PEN	N/A	50/300/40	6.5±5	700±53	50±3	2.0±1.7
Textured	Glass	Height: 0.5±0.1 Diameter: 0.06±0.01	50/300/40	7.2±2.8	680±68	50±8	2.0±2.3
NWSC - sputtered AZO top electrode	Glass	Height: 2±0.22 Diameter: 0.2±0.1	50/300/40 on each NW side	8.5±3.4	600±33	48±10	2.7±1.2
NWSC – with AZO/ITO NP composite	Glass	Height: 2±0.22 Diameter: 0.2±0.1	50/300/40 on each NW side	11.4±2.3	670±30	57±12	4.7±1.8
NWSC – with AZO/Ag NW composite	Glass	Height: 2±0.22 Diameter: 0.2±0.1	50/300/40 on each NW side	11.6±2.7	664±35	55±16	4.5±2
NWSC – with AZO/Ag NW composite	PEN	Height: 2±0.22 Diameter: 0.2±0.1	50/300/40 on each NW side	11.3±2.2	650±50	50±15	4.5±1

The composite top electrode from the NWSCs fabricated on glass substrates helped improve the total PCE to 6.3% compared to 3.9% from the NWSCs that only used AZO electrodes. The 3-D devices on PEN substrates showed PCE improvements to 5.5% with the top composite film compared to 4.0% with only AZO electrodes. The increased PCE values achieved is attributed to the increased absorption that occurred by enhanced light scattering from the Ag NWs and more efficient carrier collection by the composite electrode.

Chapter 7

3-D Nanowire Solar Cell Characteristics under Applied Mechanical Bending

Now that disordered radial-junction hybrid NWSCs have been successfully fabricated onto flexible PEN substrates, the devices can be mechanically strained to assess the performance of these flexible 3-D devices under bending. After introducing the thin-film mechanics involved when bending the structures in Section 7.1, changes observed when the top electrodes were mechanically strained under bending are described in Section 7.2. The section also presents results obtained from the flexible hybrid NWSCs, which were mechanically bent and are compared to planar solar cell devices to understand what may be causing the changes observed in the optical and electrical characteristics. A geometric model is also presented to understand the physical movement and separation distance between neighbouring NWSCs and is used to determine its effect on the number of light scattering events in the nanowire array. The chapter ends by discussing the influence that the mechanical strain may have on the electrical characteristics of the NWSCs when the devices are bent through numerical simulations and attempts to solve the issues related to bending.

Experimental optical characteristics of the thin-film and device structures were obtained using a Lambda 1050 Perkin Elmer UV/visible/NIR spectrometer. Thin-film thickness measurements were completed with a Dektak stylus profilometer while structural characterization of the NWSCs was performed using a Zeiss LEO field-emission SEM. Electrical characterization of the NWSCs was performed under standard AM 1.5G illumination conditions (ABET Technologies Sun 2000 solar simulator).

7.1 Mechanics of Bending Thin-film Structures

Consider a rectangular thin-film with dimensions ℓ, W, and t_f for length, width, and thin-film thickness, respectively, as shown in Figure 53.

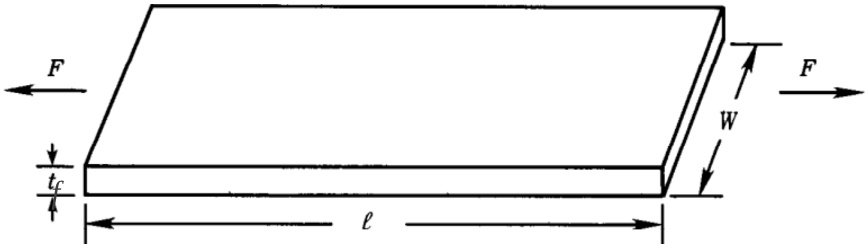

Figure 53. A thin-film under applied tension.

If a force is applied to either side of the thin-film along its cross-sectional area, $A\ (= W * t_f)$, then the thin-film would stretch in both directions, causing internal stress. Since this film is thin, the stress can be assumed to be uniform across the thickness of the film. This stress is defined as,

$$\sigma = \frac{F}{A} = E\varepsilon_H \quad (12)$$

$$\varepsilon_H = \frac{\Delta\ell}{\ell} \quad (13)$$

where E is Young's modulus, and ε_H is the induced strain, which is the change in length over the original length of the substrate. Equation (12) is referred to as Hooke's law. Young's modulus is an indicator of how elastic a material is. For example, glass possesses a very high Young's modulus (~72 GPa) compared to that of a rubber band (~7 MPa). Together with Young's modulus, the other parameter that characterizes the elastic behavior of a film is called, Poisson's ratio and can be related as,

$$-\frac{\Delta t_f}{t_f} = -\frac{\Delta W}{W} = \nu \frac{\Delta \ell}{\ell} \qquad (14)$$

where ν is Poisson's ratio of the material. A negative sign in this relationship indicates a reduction in size in both t_f and W directions as the film is stretched along ℓ. In other words, Poisson's ratio is the ratio between the transverse and longitudinal strains when a material is elastically stretched.

During the fabrication phase, thin-film that is deposited on a thick substrate, t_s, (i.e. t_f « t_s), may cause internal stress on the film-substrate pair. To ensure the net force acting on the thin-film is zero and mechanical equilibrium in the duo is reached, the film may cause the duo to warp, if the substrate is compliant (typically true for flexible substrates) as shown in Figure 54. This is known as the built-in stress of thin-film and has been discussed by several others [109]–[112]. The built-in stress of thin-film in this study is negligible as major warping effects were not found after device fabrication and is thus outside the scope of this study. However, in the same manner, thin-film on a substrate surface can be strained by externally applied bending of the substrate. In Figure 54 (a), the film-substrate duo is bent concave-down, causing tensile stress on the thin-film while Figure 54 (b) presents a schematic diagram of the thin-film under compression when the duo is bent concave-up. When moving along the z-axis of this film-substrate duo, a plane exists where the system changes in orientation from being in tension to being compressed. This plane is called the neutral axis, which is typically near the mid-point of the duo (or middle of the substrate if $t_f \ll t_s$) and is ideally where a thin-film should reside to face zero strain from mechanical bending.

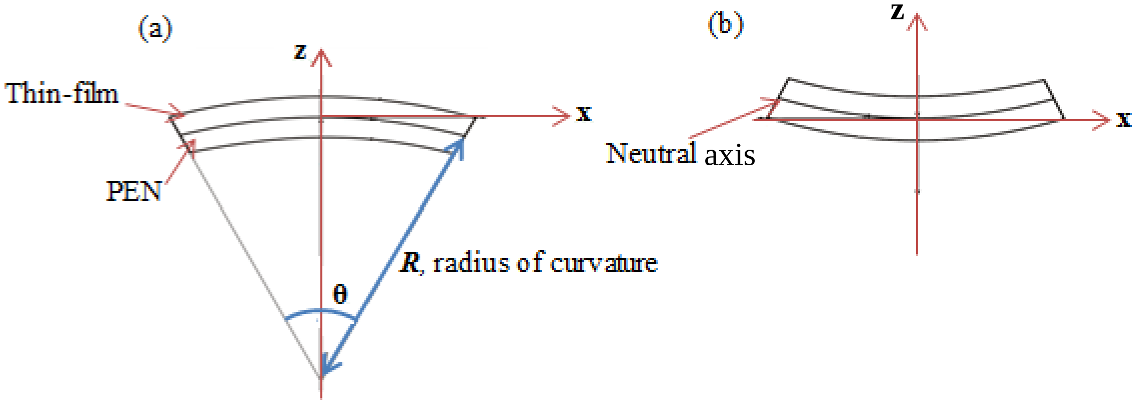

Figure 54. Mechanical bending of a thin-film on a PEN flexible substrate in a (a) concave-down (under tension) and (b) concave-up (under compression) orientation.

The lateral strain caused in the thin-film by mechanically bending the substrate to a known radius of curvature, R, can be directly calculated if R is known as,

$$\varepsilon_H = \frac{t_s}{2R}. \quad (15)$$

To determine the amount of energy that is involved along this uniform film that would produce strain, which is denoted as strain energy (E_{st}), the following equation can be used:

$$E_{st} = \int \sigma \, d\varepsilon = \frac{1}{2} E \varepsilon^2 = \frac{\sigma^2}{2E}. \quad (16)$$

Strain energy is important in cases where solid films are near equilibrium because, at equilibrium the forces acting on the film are balanced but, a small additional force (e.g.: by physically bending the film) can tilt the balance and remove the film from equilibrium, providing insight about how much external force the material can bear before mechanical failure. At equilibrium, the moment, M_f, produced by the stress in the thin-film must be equal to that obtained in the substrate, M_s. This moment produced by the linear stress in the substrate is,

$$M_s = \frac{EWt_s^3}{12R} \quad (17)$$

By equating M_s with M_f, the Stoney formula can be achieved:

$$\sigma = \frac{E{t_s}^2}{6(1-\nu)t_f R}\,. \quad (18)$$

The Stoney formula can be used to calculate the average thin-film stress that occurs from the measured R in Figure 54, with only the film-substrate properties, assuming t_f is much smaller than t_s (as is the case in this work).

7.2 Bending Characteristics of the NWSCs

7.2.1 Flexible Top Electrodes

Ag NWs were coated on the samples with the help of Mr. H. Hosseinzadeh-Kaligh. Dr. I. A. Goldthorpe and Mr. H. Hosseinzadeh-Kaligh assisted in the analysis of the data collected from the samples pertaining to the use of Ag NWs.

Since the ceramic nature of many TCO films such as ITO and AZO lead to fracture of the thin-film under mechanical strain, a property that is undesirable for flexible electronics [113], [114], a vacuum exists to help create more mechanically flexible film electrodes for flexible devices [36], [115]. Due to the enhanced charge collection and conformal coating achieved from the AZO/Ag NW composite layer on the 3-D devices, the layer's flexibility upon mechanical bending was also assessed in order to use them for flexible 3-D NWSCs. The samples were mechanically strained by attaching the structures with an adhesive onto curved static test fixtures in concave-up and concave-down orientations. The radii of curvature, *R*, tested using the fixtures were 38 mm, 32 mm, 16 mm, 6 mm, and 4 mm.

R_{sheet} of the AZO/Ag NW composite layer was measured and compared to that of AZO thin-film while flat and under mechanical bending on PEN flexible substrates. Ag pads were coated on two opposite sides of each sample to probe the films of a known surface area using a Keithley 4200-SCS parameter analyzer while four-point probe and profilometry measurements were used to determine the conductivity and thickness of the AZO thin-film, respectively.

The results of R_{sheet} from the two electrodes under mechanical strain are depicted in Figure 55. Before and after SEM micrographs revealed that the AZO thin-film had fractured due to the strain-induced cracking at R = 16 mm. Assuming the substrate thickness is 125 µm, a lateral strain of 1% was found in the AZO film electrode using Equation (15) at R = 32 mm while that in the composite electrode at R = 6 mm was 0.195%. Given the Young's modulus, E, of the films (E_{AgNW} ~ 2.64 GPa [116]; E_{AZO} ~ 106.7 GPa), the strain energy per unit volume was found using Equation (16). These strain energies for crack formation in the Ag NWs and AZO thin-film were calculated to be 5.9 MJ/m^3 and 0.2 MJ/m^3, respectively. The ~ 29× more strain energy for crack formation in the composite layer than the AZO film is due to the multi-layers in the composite film, which patches areas that may be strained in the AZO. This stress-induced cracking resulted in an increase in R_{sheet} of up to 1.1 kΩ/sq. at *R* = 6 mm in the composite film when it was mechanically bent. Despite potential damage to the AZO under-layer, the regions covered with the Ag NWs in the composite layer provide carrier pathways throughout the electrode. Flexing the samples further to *R* = 4 mm resulted in a significant increase in R_{sheet} to 12.5 kΩ/sq in the AZO thin-film while that for the composite film remained constant at ~ 1.2 kΩ/sq. The lower R_{sheet} when the composite film was flexed is likely due to the wetted Ag NWs being well-attached to the AZO, enabling a conductive path as the substrate was flexed, indicative of a ductile material while the crack-generation in the sample containing only AZO thin-film increased as *R* decreased.

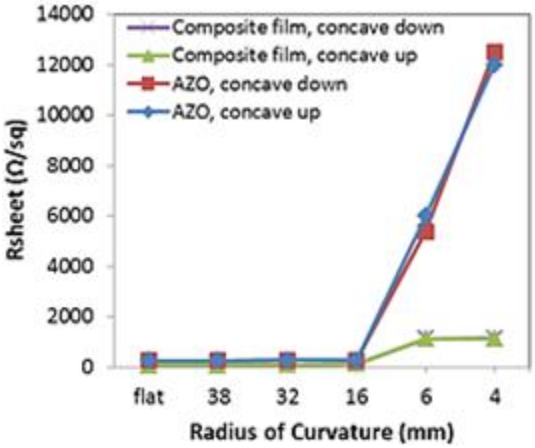

Figure 55. R_{sheet} values for the samples when flat and under different *R* for each orientation. The films were attached onto the test fixtures using a double-sided adhesive.

7.2.2 NWSC Device Performance with Mechanical Bending

The unbent NWSCs used in the mechanical bending experiments achieved on average a J_{SC} of ~ 14.2 mA/cm^2, V_{OC} of ~ 603 mV, FF of ~ 47%, and PCE of ~ 4% under AM 1.5G illumination. The devices were flexed into a concave-up and concave-down orientation to the incoming light (Figure 56) by mounting the cells on fixed sample holders of various radii of curvature, *R*, from 38 mm to 6 mm.

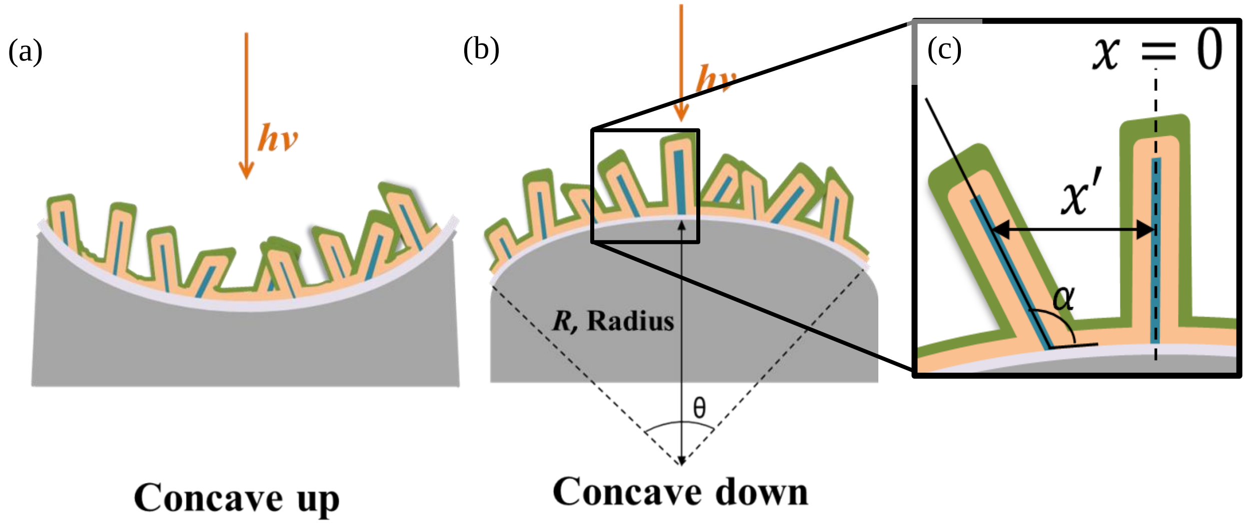

Figure 56. Schematic diagram of the bent NWSCs in (a) concave-up and (b) concave-down orientations; Θ shown is the degree of curvature from bending the substrate and (c) close-up illustration of the NWSCs and their orientation to the flexible substrate.

Figure 57 presents the electrical characteristics achieved of the NWSCs under different bending conditions. Device characteristics under flat and flexed to different *R* are plotted as a function of each device parameter in three separate plots. The plots show that a trend exists with increasing J_{SC} and PCE as the NWSCs are bent concave-up to reducing *R* from their unbent state while the opposite is true when the NWSCs are bent concave-down. The V_{OC} and FF slightly degrade as *R* decreases. R_{series} and R_{shunt} values degrade at decreasing *R* too, due to the increasing stress within the films and is the reason as to why the PCE does not increase at the same rate as the J_{SC}.

Concave-Up:

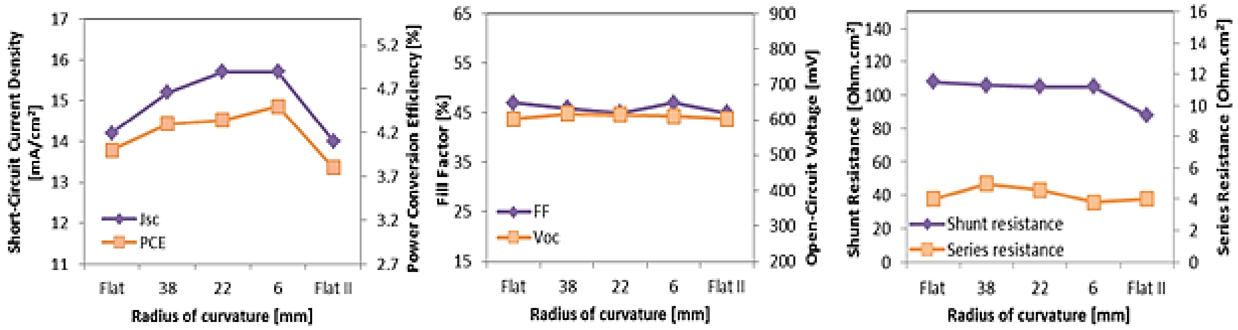

Concave-Down:

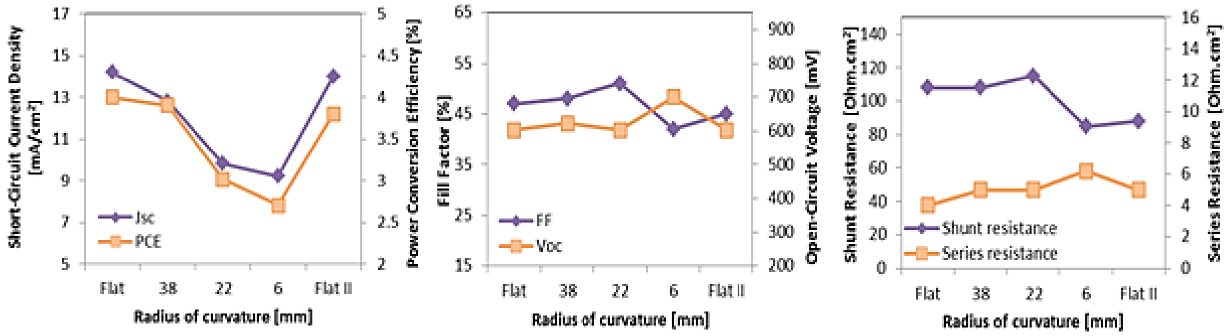

Figure 57. Electrical characteristics of the NWSCs measured while flat, mechanically bent to different *R*, and flat again.

Specifically, the J_{SC} of the NWSCs showed to increase by 15% when the substrates were oriented concave-up to the incident light at an R = 38 mm, while a decrease of 12% in J_{SC} was observed when the nanowire array was oriented concave-down at the same R (Figure 58). This change in device performance resulted in an increase (decrease) in PCE by +7.3% (-7.9%) for the concave-up (concave-down) orientation. In contrast, the J_{SC} did not change with bending in the reference flexible planar solar cells (inset of Figure 58), similar to results reported by Ng *et al.* [34]. This observation suggests the variations in J_{SC} may be from changes in light scattering due to the effective changes in the nanowire position during applied bending and will be discussed in more detail in the following section.

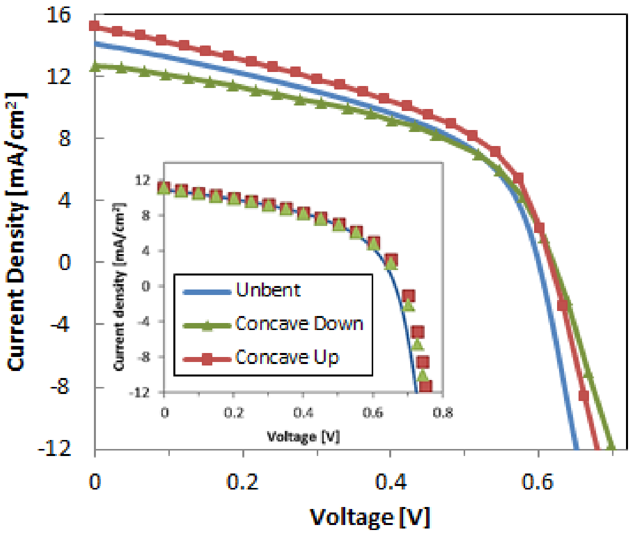

Figure 58. Electrical characteristics upon bending the NWSCs to *R* = 38 mm. Inset shows I-V characteristics of mechanically bent and unbent planar a-Si:H solar cells.

7.2.3 Light Trapping Analysis and its Correlation to NWSC Electrical Behavior

To test if the variations in J_{SC} are from changes in light scattering due to the effective changes in the nanowire position during applied bending, the optical reflectance of the nanowire mat was measured as a function of bending. Figure 59 (a) compares the total reflectance of the NWSC structures under flat (or unbent), concave-up, and concave-down orientations with *R* = 38 mm. For these optical measurements, an integrating sphere was used to collect the light reflected from the NWSC structures where a Cr back contact deposited on the PEN substrate prevented optical transmission, allowing direct measurement of the reflectivity of the structures. The average reflectivity was measured to be ~11% when flat and dropped to ~8.3% when the substrate was concave-up, while increasing to ~12% when the substrate was concave-down at wavelengths > 400 nm. For wavelengths < 400 nm, attenuation of the incoming light was dominated by the top TCO and p^+ layers [49] and was observed for all bending orientations.

The observations may be due to the effective motion of the NWSCs when the PEN substrate is flexed. The spacing between the nanowire structures decreases such that non-overlapping neighbouring nanowires begin to cross during bending in the concave-up orientation, increasing the effective density of the nanowire mat. This movement of the NWSCs towards each other also increases the disorder within the nanowire array, enhancing the light scattering and consequently, J_{SC}. For the concave-down orientation, the nanowires move further apart, which decreases the light trapping effect in the NWSCs, and thus, decreasing J_{SC}. Further bending of the PEN substrate in the concave-up (concave-down) orientation showed increasing (decreasing) J_{SC} as a function of *R*. This change in J_{SC} can be compared to the optical effect from the NWSCs using the average spectral absorption ($Ab_{sp}\%$), which was calculated for each wavelength of light as follows:

$$Ab_{sp}\% = \frac{\int_{300\,nm}^{850\,nm} \lambda A(\lambda) I(\lambda) d\lambda}{\int_{300\,nm}^{850\,nm} \lambda I(\lambda) d\lambda} \qquad (19)$$

Here, $I(\lambda)$ is the solar spectrum at AM 1.5G illumination and $A(\lambda)$ is the absorption gained from the NWSCs at each wavelength, calculated from the reflectance measurements. Figure 59 (b) depicts the change in J_{SC} from the NWSCs while flat and under mechanical bending and compares the behavior to the average optical gain in terms of the average spectral absorption.

Tamang *et al.* reported that an ~ 8.7% increase in J_{SC} may be obtained by decreasing the separation distance between radial-junction NWSCs by ~ 12.5% for nanowire mats with periods of ~ 1 µm and less [32]. For the hybrid nanowires on PEN, the effective change in distance between two neighbouring nanowires can be determined by considering the mechanical manipulation of the substrate. This displacement was found geometrically using parameters such as average NWSC height, diameter, and period in the unbent case, extracted from SEM micrographs of the NWSCs (see Appendix II for details). The tilt of the nanowire due to bending, β, can be found as a function of the distance of the nanowire from its original position, x, (where x = 0 is the substrate center, Figure 56 (c)) and *R* as,

$$\beta = \sin^{-1}\left(\frac{x}{R}\right). \qquad (20)$$

Maintaining a pivot at the center of the substrate, the effective distance of each nanowire from the substrate center after bending, x', can be calculated as,

$$x'_{up} = x - hsin(\beta + \gamma); \text{ concave up} \qquad (21)$$

$$x'_{down} = x + hsin(\beta - \gamma); \text{ concave down} \qquad (22)$$

where h is the nanowire height and $\gamma = 90 - \alpha$, where α is the original angle between the nanowire and the substrate (see Figure 56 (c)). The geometric relationships can be used to determine the effective changes to the separation distance between two adjacent nanowires under substrate bending; for example, a decrease of ~ 98 nm was calculated at *R* = 38 mm for a NWSC with α = 72° while a ~ 3 nm decrease was calculated for a NWSC normal to the substrate. These results were confirmed through numerical simulations (COMSOL Multiphysics 5.2) for a range of *R*. For the reported devices, SEM micrographs showed adjacent disordered nanowires with α ≈ 72° to be ~ 1 µm apart and during bending at *R* = 38 mm, a ~ 10% change in the separation correlates well to the predicted J_{SC} enhancement of ~ 9% by Tamang *et al.* Numerical computations that simulated the mechanical bending of the NWSCs at decreasing R showed that the NWSCs steadily decreased in separation (Figure 59 (d)), further confirming the effect that mechanical bending of the NWSCs could have on the nanowire network. The trend and values obtained for the pitch distance were very similar for the numerically simulated array and analytically calculated NWSC array. To further improve the mechanical flexibility of the devices, using a thinner substrate will ensure that the substrate-film interface reaches the neutral axis where minimum stress would be exerted on the film.

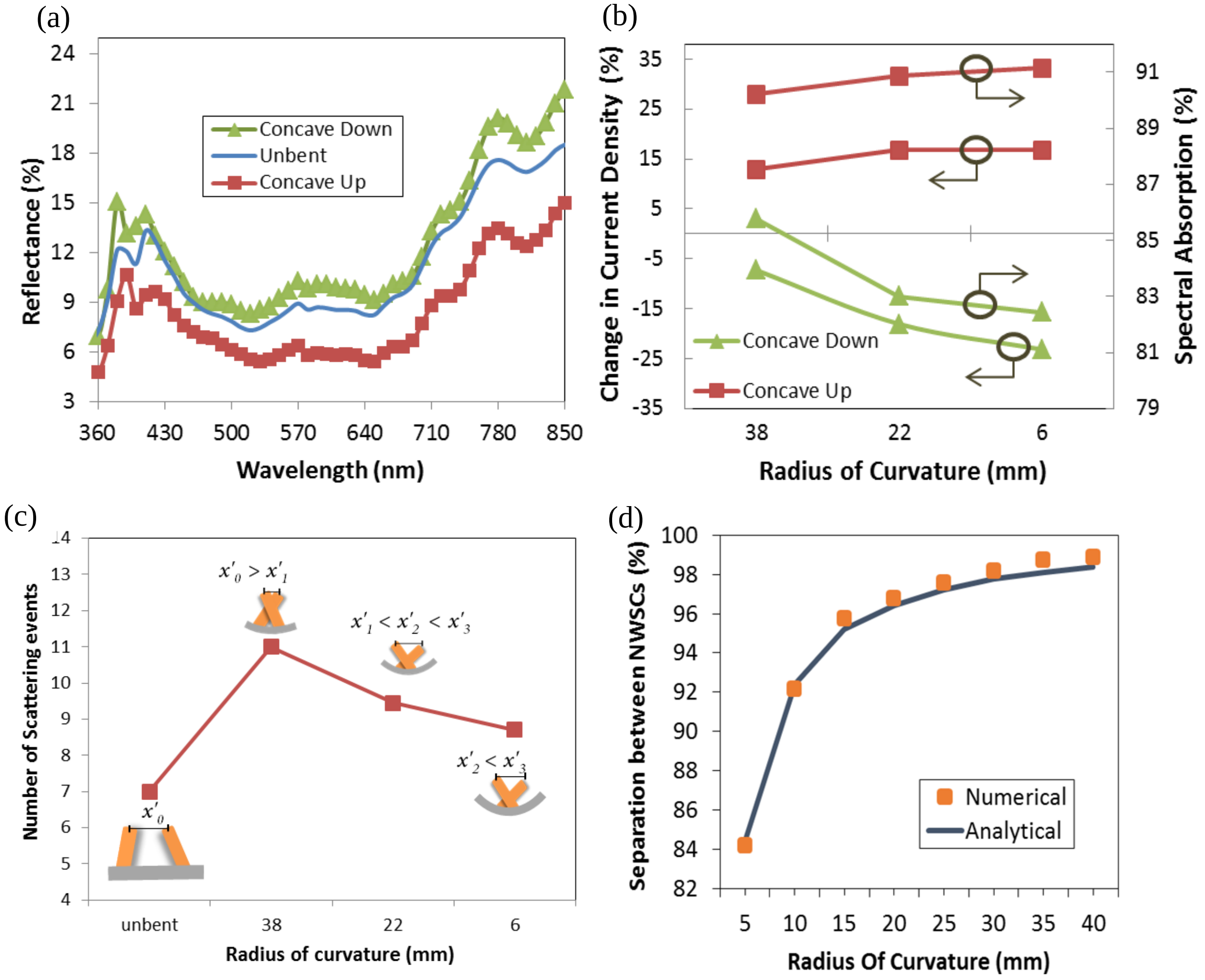

Figure 59. (a) Optical measurements of the bent and unbent NWSC to *R* = 38 mm; (b). Change in current density of the nanowire cells as a function of the radius of curvature. The secondary axis shows the spectral absorption in the NWSC for each bending case; (c). Calculated scattering events in the NWSC array as a function of radius of curvature; x'_0, x'_1, x'_2, *and* x'_3 denote *x'* for NWSCs unbent, and under *R*= 38 mm, 22 mm, and 6 mm, respectively; (d) Numerical simulations and analytical calculations of periodic NWSCs normal to the surface decreasing in NWSC separation as *R* decreases.

Furthermore, Figure 59 (b) shows that the J_{SC} begins to saturate with decreasing radii for both bending orientations, suggesting a gradual decrease in the optical scattering as *R* decreases. The effect may be explained by considering the number of scattering events as a function of the density of the nanowire mat as first presented by Street *et al.* [13], [49] where the effective absorption depth of the nanowire array can be calculated from,

$$1 = R(\lambda) + A(\lambda) \qquad (23)$$

$$R(\lambda) = 1 - \exp(-\alpha L), \qquad (24)$$

where $R(\lambda)$ is the reflectance of photons at each wavelength, $A(\lambda)$ is the absorption of photons from the a-Si:H thin-film, α is the absorption coefficient of a-Si:H, and L is the total thickness of the thin-film a photon encounters before it scatters out of the film. Given that the NWSCs possess a diameter of ~ 600 nm of coated a-Si:H film, ~ 7 scattering events were calculated before an incoming light ray was reflected for the unbent orientation. As the separation distance between the NWSCs (i.e. x') is reduced due to bending, more scattering events are expected. At R = 38 mm, the number of scattering events increases to 11 for the concave-up orientation compared to 6 when the structure is concave-down. As R in the concave-up orientation decreases, the nanowires begin to separate in the opposite direction and x' increases due to the NWSCs crossing and moving further apart from each other (Figure 59 (c)), reducing the effective density of nanowires. As a result, the number of scattering events reduced to ~ 9 and the effect of bending on the light absorption is reduced.

7.2.4 Mechanical Strain on NWSC Device Characteristics

The numerical simulations were generated with the assistance of Mr. P. Gavirneni.

While the out-of-plane nanowires dominate the electrical and optical characteristics of the solar cell, the in-plane thin-film layer of the a-Si:H parallel to the PEN surface should be also considered. Numerical simulations (COMSOL Multiphysics 5.2) of 2 μm in height ZnO nanowires coated with 300 nm thick a-Si:H were created. An assumption made to simplify the numerical models and provide a general understanding of the 3-D network when mechanically bent was that the NWSCs are periodic and normal to the substrate. The models have shown that the a-Si:H thin-film had strained in regions parallel to the substrate in the orientation that the substrate was bent while the out-of-plane thin-film, that is, along the nanowire sidewalls and top surfaces, showed no strain (Figure 60).

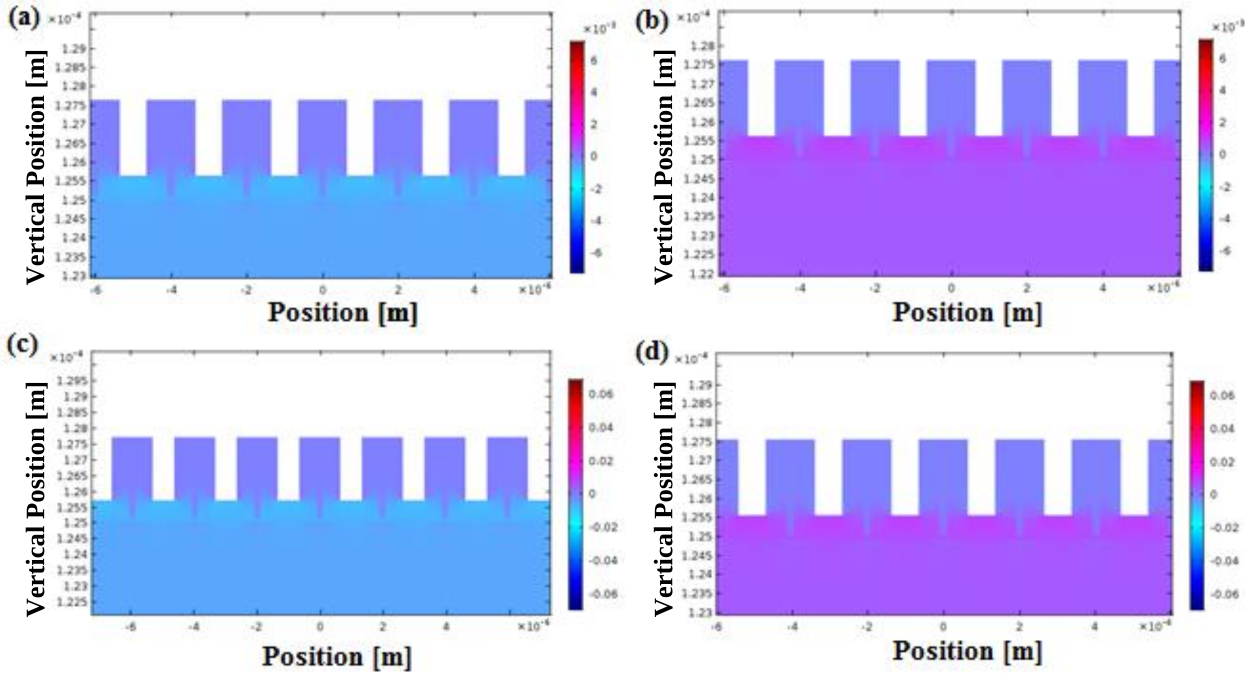

Figure 60. Numerical simulations of periodic NWSCs that were bent (a) *R* = 38 mm concave-up, (b) *R* = 38 mm concave-down, (c) *R* = 4 mm concave-up, and (d) *R* = 4 mm concave-down.

The simulations indicate a compressive strain of 0.1% when the substrate is bent concave-up to *R* = 38 mm while increasing to 1% at *R* = 4 mm (Figure 60 (a)). When bent concave-down, a tensile strain of the same values (0.1% and 1%) were observed for both *R* = 38 mm and *R* = 4 mm (Figure 60 (b) and (d)). This bending-induced strain in the planar thin-film could lead to electrical changes in the NWSC. Experimental results indicated a ΔV_{OC} of ~20 mV in both the NWSC and the planar solar cell samples at R = 38 mm (Figure 58) and has been attributed to this horizontal strain, which increases with decreasing R (Equation (15)). The effect of this strain may induce bond breaking of weak Si-Si bonds in the planar a-Si:H regions during bending [118]. For R = 38 mm, a ε_H of 0.132% was calculated using Equation (15) while a $\varepsilon_H = 1.25\%$ was calculated at R = 4 mm where the NWSCs failed under mechanical strain, corresponding to the values obtained from the numerical simulations (Figure 60) and similar to that reported by Gleskova *et al.* for planar flexible a-Si:H p-i-n devices [109]. In contrast, Fan *et al.* calculated the out-of-plane strain in the nanowires embedded in PDMS to be ~ 0.01% when the PDMS carrier was strained to 8%. This motion should not affect the surface recombination of the NWSC structures since it is outside of the plane of bending. The results suggest that the absolute density of the hybrid nanowire devices could play an additional role in the design of the flexible hybrid NWSCs. Assuming that the ZnO nanowires would be conformally coated with an increased nanowire density, increasing the nanowire density would decrease the planar regions between the nanowires. The effect of the in-plane strain would then reduce and result in less change to the V_{OC} during bending. It is also expected that increased NWSC heights would result in greater optical absorption during bending at the expense of increased shunting due to higher interface states along the nanowire sidewalls (as discussed in Chapter 5). A compromise would be to use nanowires < 2 μm with densities between 2×10^{8} cm^{-2} and 4×10^{8} cm^{-2} in order to minimize the planar regions while increasing the optical absorption by bending the NWSCs in a concave-up configuration. Future work of systematic studies that verify these effects may help lead the field of hybrid NWSCs with increasing device performance through mechanical bending and is discussed further in Chapter 9.

To summarize, the optical and electrical effects of mechanically bending flexible 3-D a-Si:H nanowire solar cells were reported. An increase of 15% and decrease of 12% in J_{SC} were measured for NWSCs on PEN substrates that were flexed to a concave-up and concave-down orientation, respectively. The difference in J_{SC} was found to be a function of the change of the optical reflectivity due to the movement of the nanowire devices during mechanical bending. Orientations where the nanowires are effectively brought closer together by flexing the PEN substrate resulted in reduced reflectivity and higher optical absorption. The AZO/Ag NW composite top electrode showed enhanced flexibility over the sputter-coated AZO thin-film as the latter electrically degraded with increasing strain-induced cracking while the composite film minimized the effect down to a radius of curvature of 4 mm. The heterogeneous integration of flexible substrates with nanowire structures provides an alternative approach to manipulating the effective density and aspect ratio of the nanowire arrays in order to enhance the performance of NWSCs, demonstrating the efficacy of employing mechanical manipulation to alter the optical properties of nanowire arrays for solar energy conversion.

Chapter 8

Water-Resistant and Self-Cleaning Hybrid Nanowire Solar Cell Devices

When operating in outdoor environments, solar cell devices are likely to accumulate dust particles and other debris on their surfaces over-time, blocking incoming sun-light and potentially reducing their PCE values. Integrating water-resistant and self-cleaning surfaces on the solar cells could help mitigate this issue. This chapter discusses the fabrication of such self-cleaning hybrid NWSC arrays by forming super-hydrophobic top surfaces. By exploiting its 3-D disordered nanostructure, the surface can be altered to increase in hydrophobicity by modulating the surface energy of the nanowires. PDMS is a silicon-based polymer that is used in both biological and medical applications because of its superior elasticity, optical transparency, non-toxicity, and thermal stability from -50ºC to 200ºC; desired attributes, which differentiates itself from other polymeric materials. This elastomer can be easily molded to desired shapes, which is advantageous to conformally coat disordered 3-D NWSCs structures.

After an introduction to PDMS in Section 8.1, Section 8.1.1 discusses the experimental methods used to synthesize the PDMS films in this work. Section 8.1.2 analyzes the surface conditions that were coated with and without PDMS and their associated hydrophobicity. Mechanical strain induced to the NWSC arrays with the added PDMS layers are numerically simulated and discussed in Section 8.1.3. The chapter ends by demonstrating the electrical characteristics of the PDMS-coated hybrid NWSCs by using the wide bandgap polymer in Section 8.2.

8.1 Using PDMS as a Self-Cleaning Layer

PDMS has been used by many groups for enhanced device functionality and for device fabrication itself such as being an alternative flexible substrate [30], [38], [79], [119], mask or mold for nanowire growth [59], nanowire transfer and replication [37], [120], [121], and as a transparent protective/passivation layer [17], [30], [122]. Most reports that use PDMS as protective layers completely encapsulate the devices, which have included both planar and nanostructured surfaces, forming planarized surfaces with microns to millimeters thick coatings. Such thick PDMS coatings enable easy handling of the devices, especially if the PDMS film becomes the new substrate of the device. Its low elastic modulus (360 kPa) allows PDMS to be a suitable alternative flexible substrate, too (Figure 61 (a)).

Similar to grass and lotus leaves, the surface energy of 3-D device structures can be altered to increase the hydrophobicity of the top surface and harness a water-resisting surface where water droplets can roll-off the device as shown in Figure 61 (b). The methyl (CH_3) bonds of PDMS (Figure 61 (c)), which comprise of ~ 20 mN/m in surface energy, is comparable to that of a lotus leaf (30 mN/m) [123]. This characteristic together with a 3-D array surface can help lower surface energies and thereby, enable superhydrophobic surfaces.

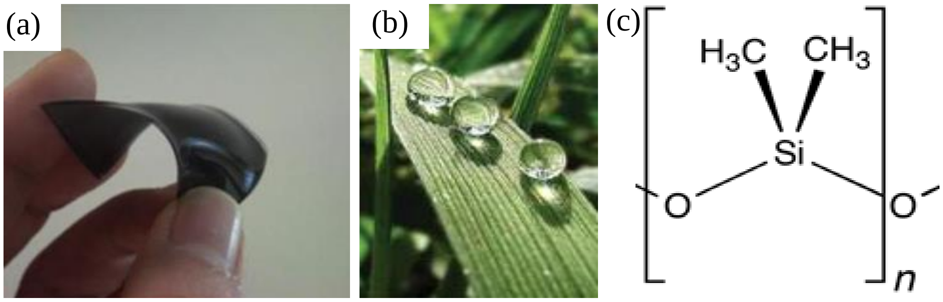

Figure 61. (a) Optical image of a flexible NWSC array embedded in PDMS [21]**. (b) Water droplets falling down grass** [124]**. (c) Unit molecular structure of PDMS.**

8.1.1 Forming PDMS Films

The PDMS films were synthesized and contact angles of water droplets were measured with the assistance of Mr. P. Gavirneni.

PDMS (Sylgard 184, Dow Corning) was mixed with toluene to dilute the solution before curing the mixture. Thus, decreasing the PDMS:toluene ratio helped bend the film more easily around the NWSCs. A PDMS curing agent was added to the mixture to help speed the cross-linking process of PDMS. Prior to spin-coating, the solution remained on the nanowire surface for approximately 2 minutes to allow for the PDMS to penetrate in between the nanowires. The solution was subsequently spun-coated and cured at 80ºC for 1 hour in an oven.

Different PDMS:toluene ratios (by weight%) and coating conditions were studied on the 3-D surfaces. A ~ 2 mm thick film was obtained after drop-casting a 1:1 ratio solution. The thick PDMS film resulted in encapsulating the NWSCs completely in the layer. Spin-coating the PDMS solution at 5000 rpm resulted in a uniform ~ 2.5 µm thick film that still completely encapsulated the nanowires underneath. However, as the toluene concentration increased, the viscosity of the solution was reduced and the PDMS film decreased in thickness. Figure 62 presents SEM micrographs of morphologies obtained when the coating conditions were altered from (a) 33% PDMS to (e) 7% PDMS in solution. Protruded nanowires underneath the PDMS film were observed after spin-coating the PDMS solution (Figure 62 (b)), which was uniformly dispersed, forming a rough surface across the sample compared to a bulk film coated on the nanowires (Figure 62 (a)). As the concentration of PDMS was further reduced to 20% (Figure 62 (c)), the underlying nanowires protruded through the thick film. As the PDMS concentration was again reduced to 10% (Figure 62 (d)) and 7% (Figure 62 (e)), the base of the hybrid NWSC array appeared and a thin-film of PDMS was conformally coated over the wires.

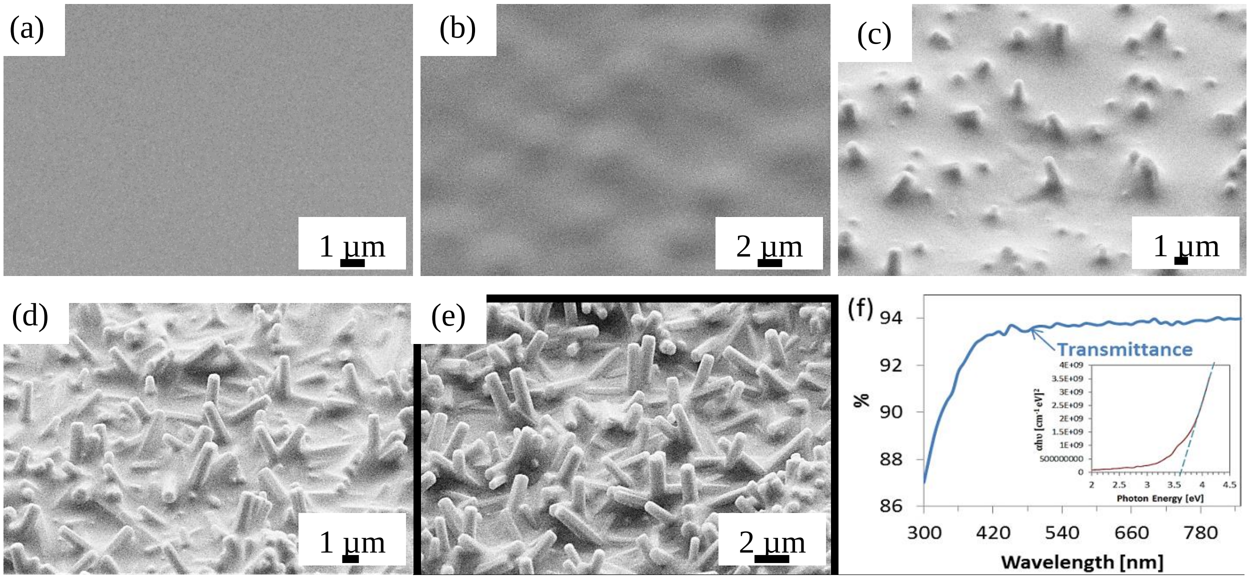

Figure 62. 45º tilted SEM micrographs of PDMS coated NWSCs with (a) 1:2 PDMS:toluene drop-casted (33% PDMS), (b) 1:2 PDMS:toluene spin-coated (33% PDMS), (c) 1:5 PDMS:toluene spin-coated (20% PDMS), (d) 1:10 PDMS:toluene spin-coated (10% PDMS), and (e) 1:15 PDMS:toluene spin-coated (7% PDMS). (f) Optical transmittance of the PDMS film spun-coated in (e); Inset: Bandgap calculation of synthesized PDMS film.

The conformal PDMS-film was ~ 40 nm and was > 92% transparent with ~ 7% reflectance between 400 nm to 850 nm (Figure 62 (f)) due to its low refractive index of ~ 1.4

[119]. Optical measurements obtained from the PDMS film coated in Figure 62 (e) show a bandgap of 3.6 eV, which corresponds to a band-edge near 344 nm.

8.1.2 Hydrophobicity of Hybrid Nanowire Structures

The hydrophobicity of the PDMS-coated NWSC arrays was assessed to determine the water resistant behaviour and self-cleaning properties of the device surfaces. Droplets of water were released through a syringe onto the NWSC arrays and their contact angles formed with the surface were measured using an Asymmetric Droplet Shape Analyzer (ADSA), which uses a charge-coupled device (CCD) camera to collect optical side-view images of the droplets on the surface (Figure 63). A post-processing image analyzer (ImageJ) was used to measure the contact angles formed by the droplets on the surface.

Flat a-Si:H thin-film obtained a contact angle, θ, of $\approx 65^{\circ}$, as depicted in the optical image shown in Figure 63 (a); in contrast, the NWSC array (without PDMS) formed a contact angle, θ, of $\sim 98^{\circ}$ (Figure 63 (b)) due to the rough 3-D surface underneath, which enables the droplet to de-wet the surface. When 40 nm of PDMS thin-film was conformally coated on the NWSC array (1:15 PDMS dilution), θ increased to $155 \pm 5.5^{\circ}$, creating near spherical droplets on the surface (Figure 63 (c)) and resulting in a superhydrophobic surface [120]. On this surface, the water droplets rolled-off to less hydrophobic areas as soon as they were dropped (i.e. very low roll-off contact angle), creating an ideal case to collect dust particles and debris on the surface as a self-cleaning solar cell.

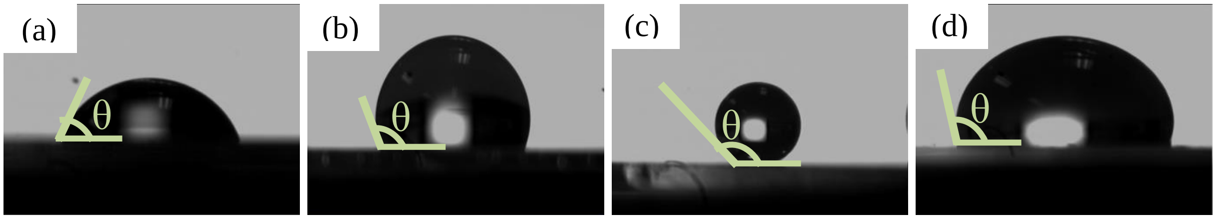

Figure 63. Contact angles (θ) from water droplets on different surfaces such as (a) flat a-Si:H thin-film, (b) NWSC array without PDMS coatings, (c)1:15 diluted PDMS coated conformally on NWSC array, and (d) NWSC array encapsulated in 2.5 µm thick PDMS.

The PDMS encapsulated NWSC sample showed θ of 112º (Figure 63 (d)) due to surface planarization, which resulted in a more hydrophilic surface. Similarly, the 1:5 diluted PDMS (Figure 62 (c)) had a contact angle of 120º, which is still lower than that obtained for the 1:15 PDMS conformally coated over the NWSC array. Here, the Wenzel model can be used to quantify the wetting properties,

$$\cos\theta_w = r\cos\theta_r \qquad (25)$$

where θ_w is the Wenzel contact angle formed on the surface with the NWSCs present, θ_r is the Young contact angle (= 65º) on the flat solar cell surface, and r is the roughness ratio (= $1+\frac{4\beta}{(1+\alpha)^2}$; $\beta = \frac{\mathrm{NW}_{\mathrm{pitch}}}{\mathrm{NW}_{\mathrm{diameter}}}$; $\alpha = \frac{\mathrm{NW}_{\mathrm{height}}}{\mathrm{NW}_{\mathrm{diameter}}}$). Decreased α (~ 2) and β (~1), as is the case here, results in a θ_w of ~ 52º, indicating a more hydrophilic surface. Thus, from this model, it is deduced that the PDMS-encapsulated NWSC arrays with reduced 3-D surfaces, possess high surface wettability.

The results presented thus far suggest that in order to form a hydrophobic surface, the surface geometry is important. Truly 3-D structures with a conformal coating of PDMS help enhance the hydrophobic behaviour of a surface because, the rough texturing from the 3-D structures create air-filled voids in the spaces between the nanowires, limiting the water droplet from wetting the regions and resulting in the large θ.

Another key criterion for superhydrophobic surfaces is the hysteresis, H, involved between the advancing angle, θ_A, and receding angle, θ_R, of a water droplet. This parameter determines the roll-off angle of the droplet on the wet surface. Ideally, the water droplets should roll-off immediately once released on the surface to collect dust and other debris that may block light from passing into the solar cell devices. A low H value ($< 15^o$) indicates that a small droplet roll-off angle would exist on the surface, indicating superhydrophobicity. To measure θ_A and θ_R, the syringe was moved parallel to the substrate surface, attempting to move the droplet on the surface. When the droplet stuck to the syringe and did not move with it but instead disconnected forming multiple droplets on the surface, the H was large ($> 15^o$), which was the case in the flat a-Si:H films. However, in the PDMS-coated NWSCs, H was calculated to be 12.5 ± 2^o, which is considered superhydrophobic.

Mechanically flexing the NWSC array did not show a large change in the original values of the contact angles as the 3-D effect was retained during bending. The contact angles varied within $\pm 3^o$ as the hybrid NWSC was bent to $R = 38$ mm (150^o), 22 mm (157^o), and 11 mm (160^o) in both concave-up and concave-down orientations, suggesting that bending the NWSC array does not affect the hydrophobicity of the device surface so long as the 3-D structure is intact and that the nanowires are conformally coated with PDMS to ensure a methyl-filled surface.

Additionally, the optical characteristics of the sample of NWSCs that was conformally-coated with PDMS were measured while the 3-D devices were mechanically bent. An average optical reflectivity of ~ 8% was measured when the devices were flat and increased to 9% when the substrate was bent concave-down while decreasing to ~ 6% when bent concave-up. These results are similar to the optical reflectance measurements achieved for the sample of NWSC arrays with no PDMS, indicating that the high optical transmittance (~ 91%) of the PDMS film does not adversely affect the optical characteristics of the devices.

8.1.3 Mechanical Strain in PDMS-Coated Hybrid NWSC Arrays

The numerical simulations were generated with the assistance of Mr. P. Gavirneni.

Numerical simulations (Figure 64) showed that a conformal coating of PDMS on the NWSCs induces no stress even when the devices are mechanically bent. As previously stated, an assumption made to simplify the numerical models and provide a general understanding of the 3-D network when mechanically bent was that the NWSCs are periodic and normal to the substrate. Changing the simulations to increase disorder in the mesh exponentially increases build time. Furthermore, the parameters for the p-i-n a-Si:H were grouped together as 400 nm of intrinsic a-Si:H film to further simplify computation.

The final simulations show that when the encapsulated NWSCs were mechanically bent concave-up from *R* = 38 mm to *R* = 4 mm, 0.01% to 1% of strain was observed, respectively, and was contained predominantly in the PDMS while the out-of-plane NWSCs showed no strain as shown in Figure 64 (a) (grey-purple regions of NWSCs). This is because the high ductility of PDMS (*E* ~ 360 kPa), allowed the encapsulate layer to easily compress (or “squish”) from the inward movement of the neighbouring nanowires when the substrate was bent, resulting in increasing compression away from the NWSC base in the regions of PDMS that coat the sidewalls of the NWSCs. Furthermore, the top region of the PDMS encapsulate conforms to create ~ 1% compression (bright blue region of Figure 64 (b)). Less than 0.25% strain in the a-Si:H film was observed parallel to the substrate due to the compressive plane-strain induced in breaking weak Si-Si bonds in the a-Si:H, confirming the strain calculations of 0.125% from this region as was discussed in Chapter 7. When the PDMS conformally coated the NWSCs as depicted in Figure 64 (c), only strain near the base of the NWSCs was observed while the out-of-plane NWSCs showed no strain. These results indicate that the mechanical properties of PDMS do not obstruct the movement of the NWSCs when the substrate is mechanically bent.

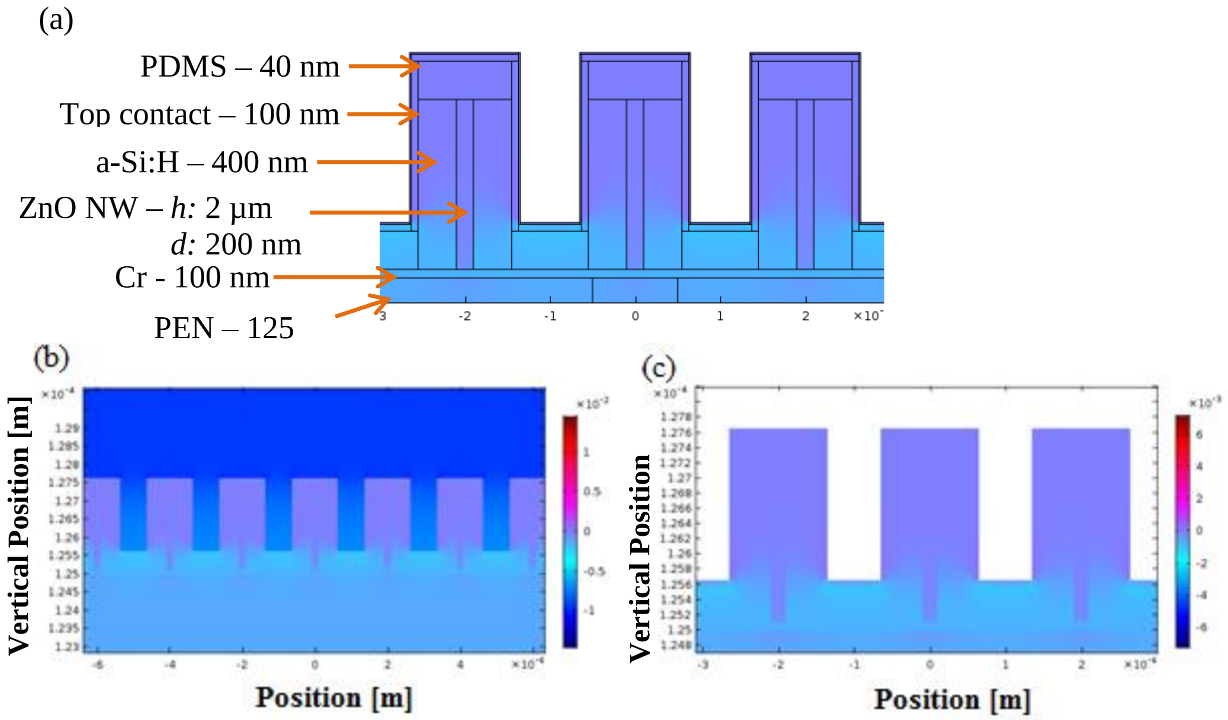

Figure 64. (a) Labeled schematic diagram of the simulated NWSCs. NWSCs bent concave-down to *R* = 4 mm that were (b) encapsulated with PDMS and (c) conformally coated with PDMS.

Similarly, when the 3-D hybrid devices were bent concave-down to *R* = 4 mm, the NWSC array that was encapsulated in PDMS showed < 0.5% tensile strain in the PDMS between the NWSCs (magenta region in Figure 65 (a)) due to the out-ward movement of the out-of-plane wires. This region of PDMS increases in strain away from the NWSC base as greater movement occurs in the top regions of the wires when the substrate is bent. The top surface consists of the most tension (~ 1%) as the substrate is bent concave-down. When the NWSC array was conformally coated with 40 nm of PDMS, the strain induced in the PDMS was negligible and only the film parallel to the substrate near the base of the nanowires showed tensile strain of up to ~ 1%. Since the strain induced in the NWSCs by incorporating the additional PDMS layer is negligible, the NWSCs can freely move according to the movement that is dictated by the mechanical bending movements of the substrate.

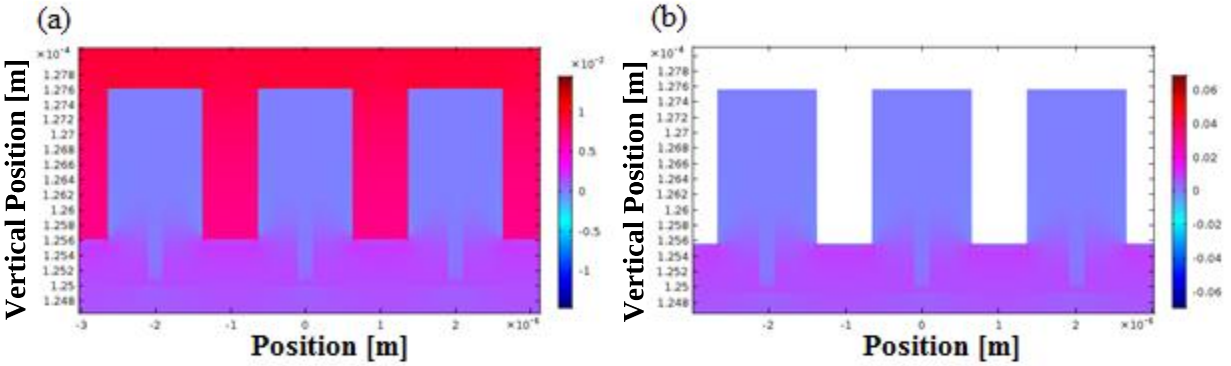

Figure 65. NWSCs that are (a) encapsulated with PDMS and (b) coated conformally with PDMS and bent concave-down at *R* = 4 mm.

8.2 Electrical Characterization of PDMS-Coated Hybrid NWSC Arrays

Experimental I-V characteristics of the PDMS coated NWSC arrays were measured. The electrical performances of the 3-D device before and after the PDMS coating are depicted in

Figure 66. A slight 2.2% decrease is noted in J_{SC} due to the additional film coated on the NWSCs while the V_{OC} (~ 613 mV) and FF (57%) remained relatively similar to before the PDMS coating and the PCE was constant at ~ 4.7% in both cases, suggesting that the PDMS coating does not impede device performance while adding hydrophobic surface functionality as a self-cleaning solar cell device.

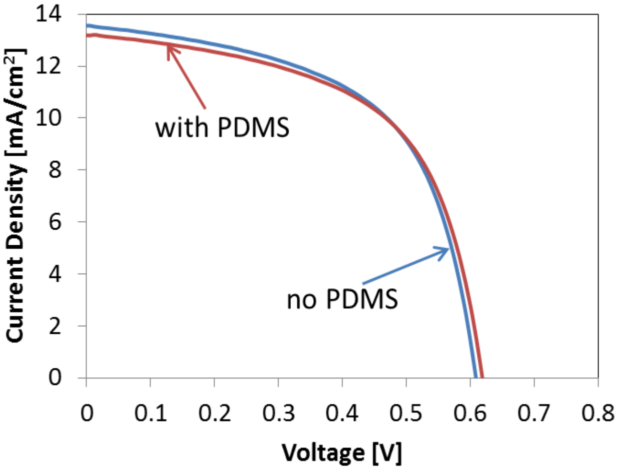

Figure 66. I-V characteristics of the NWSC before and after PDMS coating.

In summary, superhydrophobic surfaces were achieved by modifying the surfaces of the disordered NWSC array by using PDMS films. The contact angle was increased to 155º with a low hysteresis of 8º on the conformal PDMS-coated NWSC array. Therefore, the surface had very low wettability, which is ideal to collect dirt and dust debris with water droplets on the surfaces. The induced strain was negligible, indicating the ability of the NWSCs to effectively freely move with the additional PDMS layer as the substrate mechanically bends. Electrical characteristics of the PDMS-coated NWSCs do not show significant changes to the overall PCE by adding the transparent film; thus, enabling self-cleaning solar cell devices.

Chapter 9

Conclusion and Future Work

9.1 Conclusion and Contributions to Nanowire Solar Cells

The following is a list of summarized novel contributions of this PhD research to the field of 3-D photovoltaics:

1. Fabrication of conformal hybrid 3-D ZnO nanowire/a-Si:H p-i-n thin-film solar cell arrays
2. Direct fabrication of 3-D NWSC arrays on low melting-point flexible substrates
3. AZO/Ag NW composite top electrode formation for disordered 3-D devices
4. Optical and electrical enhancements by mechanically bending flexible 3-D devices
5. Formation of self-cleaning properties on 3-D devices

Conformal coatings of a-Si:H p-i-n thin-film were deposited on disordered ZnO nanowire arrays to form radial-junction 3-D NWSC devices. The process steps occurred at temperatures below 200ºC to enable 3-D device fabrication directly on flexible PEN substrates and thereby, minimize additional processing. The combination of enhanced light scattering due to the 3-D hybrid structures and the improved conformal coverage of the top transparent contact resulted in an overall highest PCE of 6.5% using 2 μm in height ZnO nanowires of a nanowire density of 2×10^{8} cm^{-2}. These results demonstrate the feasibility of integrating randomly ordered nanostructures with amorphous thin-films to form 3-D photovoltaic device structures.

Both the AZO/ITO nanoparticle composite layer and AZO/Ag NW composite coatings were used as top electrodes for the 3-D hybrid structures. Although good contact and efficient charge collection were detected using the former, the film cracked and delaminated due to its brittle nature upon mechanical bending. The AZO/Ag NW composite coating conformally covered the 3-D nanowire array at 200ºC, enabling efficient charge collection while staying intact during mechanical bending down to R = 4 mm. The results reported here demonstrate the efficacy of the disordered hybrid NWSC devices for enhancing light scattering and, combined with conformal top contacts, are an alternate approach to efficient power generation using flexible solar cells.

When the flexible NWSCs were mechanically bent concave-up to R = 38 mm, an 8% increase in J_{SC} was detected while a 12% decrease was detected in the same 3-D devices when bent concave-down. These 3-D devices showed an optical absorption enhancement by 4% and degradation by 8% when the substrate was bent concave-up and concave-down, respectively. These experimental results indicate that light trapping within the 3-D nanowire network can be altered by changing the period of neighbouring nanowires, resulting in changes to the amount of light rays absorbed by the NWSCs. A change to the device's V_{OC} resulted due to lateral strain of

0.132% along the a-Si:H thin-film that was parallel to the substrate surface, indicating a density of nanowires between 2×10^{8} cm^{-2} and 4×10^{8} cm^{-2} could reduce the contribution of lateral strain to the electrical performance of the 3-D devices. These results show the viability of enhancing the device's current collection through mechanical bending of 3-D devices.

An effect similar to that of an electronic lotus leaf with self-cleaning properties was achieved by coating the 3-D hybrid NWSCs with PDMS to alter the surface energy and create super-hydrophobic NWSCs. Incorporating a conformal PDMS layer on the NWSCs helped increase the contact angle of the wetting surface to increase up to 155º-160º. By encapsulating the NWSCs in PDMS and creating a planarized film, the contact angle was decreased to 112º. I-V characterization showed no major changes to the NWSCs with the PDMS coating due to the > 90% optical transparency in the visible spectrum. These results show the efficacy of fabricating high efficiency, self-cleaning NWSCs directly on flexible substrates.

9.2 The Future of Flexible 3-D Hybrid NWSCs

Areas for future study include:

1. Treatment of the ZnO/n^{+} interface to reduce localized interface states and increase conductivity to enhance the electrical characteristics of the hybrid nanowire devices
2. Improve the PCE of the solar cell by incorporating intrinsic nc-Si:H thin-films between the n^{+}/i and i/p^{+} interfaces
3. Mechanical bending of NWSC arrays (with improved interfaces) of varied lengths and densities

4. Mechanical bending of ordered NWSCs with controlled angles to the substrate

Point #1 above is two-fold: 1. Treatment of the ZnO/n$^+$ interface to reduce localized states could enhance collection of minority carriers that diffuse through the n$^+$ a-Si:H layer in the solar cell for collection at the Cr electrode and minimize the chances of losing the carriers to these localized trap states; 2. A treatment prior to depositing the n$^+$ a-Si:H film could also improve collection of the generated carriers by increasing the conductivity of the ZnO nanowires and reducing the total series resistance in the 3-D device. Currently, the conformal deposition of n+ a-Si:H is critical to ensure the carriers would have a path to the bottom Cr electrode while the ZnO nanowires act only as a pillar support to ensure a 3-D structure. But, by including the ZnO nanowires as an active part of the device, the collection of carriers could be more efficient. One possible method might be a pre-anneal treatment of the ZnO nanowires.

Point #2 may help reduce the shallow defect states at the n$^+$/i and i/p$^+$ interfaces, increasing the V_{OC} and R_{shunt} of the planar solar cell by expanding the quasi-fermi energy levels of the p$^+$ and n$^+$ films, and thereby increasing the built-in energy of the solar cell. Using these films to fabricate hybrid NWSCs would facilitate use of longer NWSCs and greater nanowire densities without compromising device performance.

Points #3 and #4 are follow-up studies to points #1 and #2; the NWSC array with reduced interface states should be characterized under applied bending to further assess the electrical enhancements that may be gained by increasing the heights and densities of the nanowire array. Bending NWSC arrays with increased densities from 2×10^8 cm^{-2} to 2.8×10^8 cm^{-2} at $R = 38$ mm, helped reduce the effect of ΔV_{OC} while enhancing the J_{SC} achieved through bending the substrate due to the reduced area of a-Si:H thin-film that is parallel to the substrate. Thus, the contribution of plane-strain from bending the NWSCs was reduced by increasing the density of NWSCs. More experiments at different radii would provide further insight to the 3-D device performances.

To ensure a systematic study, the ZnO nanowire arrays employed should be ordered upon growth and possess pre-determined tilts that each wire makes to the substrate to better assess and compare the improvements detected between the NWSCs and disordered NWSC arrays. The study can also use the analytical model that was presented in Chapter 5 of this dissertation to further assess the experimental results.

9.3 Published Articles and Conferences Presented

9.3.1 Journal Articles and Conference Proceedings

PEER REVIEWED JOURNALS

- **M. K. Pathirane** and W. S. Wong, "Optical and Electrical Characteristics of Nanowire Solar Cells under Applied Bending", *Small, just accepted*, **2016**
- N. Dhindsa, J. Walia, **M. Pathirane**, I. Khodadad, W. Wong and S. S. Saini, "Adjustable Optical Response of Amorphous Silicon Nanowires Integrated with Thin Films", *Nanotechnology, just accepted*, **2016**
- **M. Pathirane**, B. Iheanacho, A. Tamang, C.-H. Lee, R. Lujan, D. Knipp, and W. S. Wong, "Hybrid ZnO nanowire/a-Si:H thin-film radial junction solar cells using improved nanoparticle front contact", *Applied. Physics Letters*, **107**, 14, **2015**
- A. Tamang, **M. Pathirane**, R. Parsons, M. M. Schwarz, B. Iheanacho, V. Jovanov, V. Wagner, W. S. Wong, and D. Knipp, "Zinc oxide nanowire arrays for silicon core/shell solar cells", *Optics Express*, 22, **2014**, pp. A622-A632

- M. Moradi, **M. Pathirane**, A. Sazonov, R. Chaji, and A. Nathan, "TFTs with High Overlay Alignment for Integration of Flexible Display Backplanes", *Journal of Display Technology IEEE*, **8**, 2, **2012**, pp. 104-107

REFEREED CONFERENCES

- W. S. Wong, M. J. Chow, **M. Pathirane**, B. Iheanacho, and C.-H. Lee, "Heterogeneously integrated nanowires and thin films for flexible electronics", *IEEE AM-FPD*, **2014**, pp.37-40

MANUSCRIPTS UNDER REVIEW OR IN PROGRESS

- **M. K. Pathirane**, H. Hosseinzadeh-Kaligh, I. A. Goldthorpe, and W. S. Wong, "Conformal and Transparent Silver Nanowire Electrodes for 3-Dimensional Solar Cells on Flexible Substrates", *in submission*, **2016**

9.3.2 Oral and Poster Presentations

ORAL

- **Pathirane M.**, Hosseinzadeh H., Goldthorpe I., and Wong W. S., (2015) "Transparent Ag Nanowire Electrodes for 3D Structured Solar Cells", Electronics Materials Conference (EMC), Columbus, OH (International conference)
- **Pathirane M.**, Iheanacho B., Lee C-H., and Wong W. S., (2015) "Amorphous Silicon Nanowire Solar Cells on Flexible Substrates", TechConnect World Innovation, Washington, DC (International conference)
- **Pathirane M.**, (2014) "Hybrid Nanowire/Thin-Film Solar Cells", Waterloo Institute for Nanotechnology, Waterloo, ON (Invited talk)
- Iheanacho B.*, **Pathirane M.**, Lee C-H., Hamadani B., and Wong W. S., (2014) "A-Si:H Thin-Film – Nanowire Hybrid Structure for Infrared Sensor Applications", Materials Research Society (MRS), San Francisco, CA (International conference)

- **Pathirane M.,** Iheanacho B., Tamang A., Jovanov V., Knipp D., and Wong W. S., (2013) "Hybrid ZnO Nanowire/a-Si:H Thin-Film Solar Cells on Flexible Substrates", International Semiconductor Device Research Symposium, Bethesda, MD (International conference)
- **Pathirane M.**, Iheanacho B., Tamang A., Jovanov V., Knipp D., and Wong W. S., (2013) "Hybrid ZnO Nanowire/a-Si:H Thin-Film Solar Cells on Flexible Substrates", Electronics Materials Conference (EMC), Notre Dame, IN (International conference)
- Moradi M.*, **Pathirane M.**, Sazonov A., Chaji R., and Nathan A. (2010) "A-Si:H TFT backplanes with reduced overlay misalignment on flexible substrates at low temperatures", Engineering Conferences International, Spain (International conference)

POSTER

- **Pathirane M.**, Gavirneni P., and Wong W. S., (2016) "Mechanical Manipulation of Flexible Nanowire Solar Cells", Materials Research Society (MRS), Phoenix, AZ (International conference)
- **Pathirane M.**, Iheanacho B., Hosseinzadeh H., Tamang A, Lee C-H., Goldthorpe I., Knipp D., and Wong W. S., (2015) "Hydrogenated Amorphous Silicon-based Flexible Nanowire Solar Cells", Materials Research Society (MRS), San Francisco, CA (International conference)
- **Pathirane M.**, Hosseinzadeh H., Iheanacho B., Tamang A, Lee C-H., Goldthorpe I., Knipp D., and Wong W. S., (2014) "Influence of Top Electrodes on Amorphous Silicon Nanowire Solar Cells", Waterloo Engineering Innovate, Waterloo, ON (Local conference)
- **Pathirane M.**, Papadopoulos N., Lee C-H., and Wong W. S., (2014) "Heterogeneous Integration for Flexible Electronics, Devices and Sensors", Waterloo, ON (Local conference)
- Iheanacho B.*, **Pathirane M.**, and Wong W. S., (2013) "Infrared Absorption of Thin Film – Nanowire Hybrid Structures", International Semiconductor Device Research Symposium, Bethesda, MD (International conference)

- Parsons R.*, **Pathirane M.,** Iheanacho B., Jovanov V., Schwarz M., Wagner V., Wong W. S., and Knipp D., (2013) “Zinc Oxide Nanowire Arrays for Silicon Rod Solar Cells: Wire Design and Experimental Realization”, Materials Research Society (MRS), San Francisco, CA (International conference)
- **Pathirane M.**, Iheanacho B, Tamang A, Jovanov V., Knipp D., and Wong W. S., (2013) “Novel Hybrid Nanowire/Thin-Film Core-Shell Structures for Solar Cells on Flexible Platforms”, Waterloo Engineering Innovate, Waterloo, ON (Local conference)
- Iheanacho B.*, **Pathirane M.**, and Wong W. S., (2013) “Towards Hybrid Thin Film – Nanowire Structures”, Waterloo Engineering Innovate, Waterloo, ON (Local conference)
- **Pathirane M.,** Iheanacho B., Patchett S., Saini S., and Wong W. S. (2012) “Optical Characteristics of Solution-Grown ZnO Nanowires”, NanoOntario, Waterloo, ON (Provincial conference)
- Moradi M., **Pathirane M.**, Sazonov A., Chaji R., and Nathan A. (2010) “Lithographic misalignment reduction for TFT backplane fabrication on transparent plastic substrates”, Materials Research Society (MRS), San Francisco, CA (International conference)

Appendix I

Material Properties

PEN substrate

Glass transition temperature: 260ºC

Young's modulus: 5 GPa

Poisson's ratio: 0.35 [125]

Glass (Corning) substrate

Glass transition temperature: 600ºC

Young's modulus: 70 – 80 GPa [126]

Cr thin-film

Glass transition temperature: 600ºC

Young's modulus: 279 GPa

AZO thin-film

Young's modulus: 106.7 GPa

Poisson's ratio:~ 0.3

PDMS

Young's modulus: 360 kPa [127]

Poisson's ratio: 0.5

Appendix II

Geometric Model of Nanowire Displacement

The distance from the substrate center (assuming a nanowire exists in this location) for each nanowire after bending, x', was found using geometric analysis. The solid blue line in the figure below represents a nanowire and the dotted line indicates the substrate center when the substrate is flat and bent concave up.

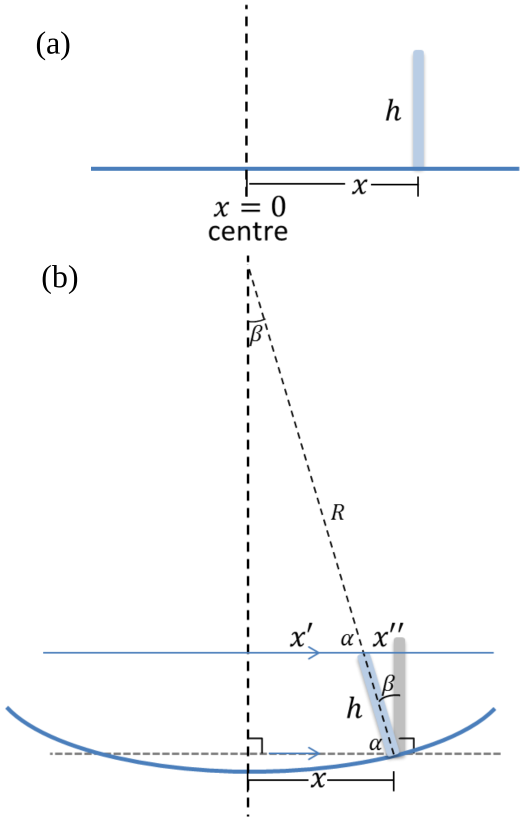

h: height of the nanowire; *R*: radius of curvature

x: distance of the nanowire from the center of the device where *x* = 0

D: Device length

β: Resulting nanowire tilt from its original position upon substrate bending

θ: Degree of curvature

Limits:

At $x = 0,\ \beta = 0.$

At $x = {}^{D}/_{2},\ \beta = {}^{\theta}/_{2}.$

At all other points of x, $\beta = \sin^{-1}\left(\frac{x}{R}\right)$.

Figure A67. (a) A nanowire of height *h* and distance *x* from the substrate center; (b) The nanowire (in blue) moved toward the substrate center as the substrate (blue) is bent concave-up with respect to its original form (in grey).

When the device is bent concave-up:

$$x = x' + x''$$

$$x' = x - hsin(\beta + \gamma)$$

where γ is the original angle of the nanowire with respect to the substrate surface (shown oriented $\perp$ to substrate in the figure above). Similarly, when the device is bent concave-down:

$$x' = x + hsin(\beta - \gamma).$$

References

[1] J. Zhu and Y. Cui, “Photovoltaics: More solar cells for less.,” *Nat. Mater.*, vol. 9, no. 3, pp. 183–4, Mar. 2010.

[2] N. S. Lewis, “Toward Cost-Effective Solar Energy Use,” *Science (80-.).*, vol. 315, no. 5813, pp. 798–802, 2007.

[3] B. Tian, X. Zheng, T. J. Kempa, Y. Fang, N. Yu, G. Yu, J. Huang, and C. M. Lieber, “Coaxial silicon nanowires as solar cells and nanoelectronic power sources.,” *Nature*, vol. 449, no. 7164, pp. 885–9, Oct. 2007.

[4] L. J. Lauhon, M. S. Gudiksen, D. Wang, and C. M. Lieber, “Epitaxial core-shell and core-multishell nanowire heterostructures.,” *Nature*, vol. 420, no. 6911, pp. 57–61, Nov. 2002.

[5] R. A. Street, W. S. Wong, and C. Paulson, “Analytic model for diffuse reflectivity of silicon nanowire mats.,” *Nano Lett.*, vol. 9, no. 10, pp. 3494–7, Oct. 2009.

[6] V. E. Ferry, M. a. Verschuuren, H. B. T. Li, R. E. I. Schropp, H. A. Atwater, and A. Polman, “Improved red-response in thin film a-Si:H solar cells with soft-imprinted plasmonic back reflectors,” *Appl. Phys. Lett.*, vol. 95, no. 18, p. 183503, 2009.

[7] L. Tsakalakos, J. Balch, J. Fronheiser, B. a. Korevaar, O. Sulima, and J. Rand, “Silicon nanowire solar cells,” *Appl. Phys. Lett.*, vol. 91, no. 23, p. 233117, 2007.

[8] M. D. Kelzenberg, S. W. Boettcher, J. A. Petykiewicz, D. B. Turner-Evans, M. C. Putnam, E. L. Warren, J. M. Spurgeon, R. M. Briggs, N. S. Lewis, and H. A. Atwater, “Enhanced absorption and carrier collection in Si wire arrays for photovoltaic applications.,” *Nat. Mater.*, vol. 9, no. 3, pp. 239–44, Mar. 2010.

[9] T. J. Kempa, R. W. Day, S.-K. Kim, H.-G. Park, and C. M. Lieber, “Semiconductor nanowires: a platform for exploring limits and concepts for nano-enabled solar cells,” *Energy Environ. Sci.*, vol. 6, no. 3, p. 719, 2013.

[10] J. Zhu, Z. Yu, G. F. Burkhard, C.-M. Hsu, S. T. Connor, Y. Xu, Q. Wang, M. McGehee, S. Fan, and Y. Cui, “Optical absorption enhancement in amorphous silicon nanowire and nanocone arrays.,” *Nano Lett.*, vol. 9, no. 1, pp. 279–82, Jan. 2009.

[11] L. Hu and G. Chen, “Analysis of optical absorption in silicon nanowire arrays for photovoltaic applications.,” *Nano Lett.*, vol. 7, no. 11, pp. 3249–52, Nov. 2007.

[12] O. L. Muskens, J. G. Rivas, R. E. Algra, E. P. A. M. Bakkers, and A. Lagendijk, “Design of Light Scattering in Nanowire Materials for Photovoltaic Applications 2008,” *Nano Lett.*, vol. 8, no. 9, pp. 2638–2642, 2008.

[13] R. A. Street, P. Qi, R. Lujan, and W. S. Wong, “Reflectivity of disordered silicon nanowires,” *Appl. Phys. Lett.*, vol. 93, no. 16, p. 163109, 2008.

[14] A. Polman and H. a Atwater, “Photonic design principles for ultrahigh-efficiency photovoltaics.,” *Nat. Mater.*, vol. 11, no. 3, pp. 174–7, Mar. 2012.

[15] S. Misra, L. Yu, M. Foldyna, and P. Roca i Cabarrocas, “High efficiency and stable hydrogenated amorphous silicon radial junction solar cells built on VLS-grown silicon nanowires,” *Sol. Energy Mater. Sol. Cells*, vol. 118, pp. 90–95, Nov. 2013.

[16] A. Tamang, M. Pathirane, N. Yumnam, B. Iheanacho, D.-J. Amankwah, M. Schwarz, V. Jovanov, V. Wagner, W. Wong, and D. Knipp, “On the conversion efficiency of core/shell nanowire solar cells,” *Submitted*, 2014.

[17] Z. Fan, H. Razavi, J. Do, A. Moriwaki, O. Ergen, Y.-L. Chueh, P. W. Leu, J. C. Ho, T. Takahashi, L. A. Reichertz, S. Neale, K. Yu, M. Wu, J. W. Ager, and A. Javey, “Three-dimensional nanopillar-array photovoltaics on low-cost and flexible substrates.,” *Nat. Mater.*, vol. 8, no. 8, pp. 648–53, Aug. 2009.

[18] M. Khorasaninejad, N. Abedzadeh, A. Singh Jawanda, N. O, M. P. Anantram, and S. Singh Saini, “Bunching characteristics of silicon nanowire arrays,” *J. Appl. Phys.*, vol. 111, no. 4, p. 044328, 2012.

[19] J. Kim, C. Battaglia, M. Charrière, A. Hong, W. Jung, H. Park, C. Ballif, and D. Sadana, “9.4% Efficient Amorphous Silicon Solar Cell on High Aspect-Ratio Glass Microcones,” *Adv. Mater.*, vol. 26, no. 24, pp. 4082–4086, 2014.

[20] K. E. Plass, M. a. Filler, J. M. Spurgeon, B. M. Kayes, S. Maldonado, B. S. Brunschwig, H. a. Atwater, and N. S. Lewis, “Flexible Polymer-Embedded Si Wire Arrays,” *Adv. Mater.*, vol. 21, no. 3, pp. 325–328, Jan. 2009.

[21] K.-T. Park, Z. Guo, H.-D. Um, J.-Y. Jung, J. M. Yang, S. K. Lim, Y. S. Kim, and J.-H. Lee, “Optical properties of Si microwires combined with nanoneedles for flexible thin film photovoltaics.,” *Opt. Express*, vol. 19 Suppl 1, no. January, pp. A41–A50, 2011.

[22] C. L. Pint, K. Takei, R. Kapadia, M. Zheng, A. C. Ford, J. Zhang, A. Jamshidi, R. Bardhan, J. J. Urban, M. Wu, J. W. Ager, M. M. Oye, and A. Javey, “Rationally designed, three-dimensional carbon nanotube back-contacts for efficient solar devices,” *Adv. Energy Mater.*, vol. 1, no. 6, pp. 1040–1045, 2011.

[23] M. M. Adachi, M. P. Anantram, and K. S. Karim, “Core-shell silicon nanowire solar cells,” *Sci. Rep.*, vol. 3, p. 1546, Jan. 2013.

[24] F. Roca, G. Sinno, G. Di Francia, P. Prosini, G. Fameli, P. Grillo, a. Citarella, F. Pascarella, and D. della Sala, “Process development of amorphous silicon/crystalline silicon solar cells,” *Sol. Energy Mater. Sol. Cells*, vol. 48, no. 1–4, pp. 15–24, Nov. 1997.

[25] S. Misra, L. Yu, M. Foldyna, and P. Roca, “New Approaches to Improve the Performance of Thin-Film Radial Junction Solar Cells Built Over Silicon Nanowire Arrays,” vol. 5, no. 1, pp. 40–45, 2015.

[26] L. Yu, S. Misra, J. Wang, S. Qian, M. Foldyna, J. Xu, Y. Shi, E. Johnson, and P. R. I. Cabarrocas, “Understanding light harvesting in radial junction amorphous silicon thin film solar cells.,” *Sci. Rep.*, vol. 4, p. 4357, 2014.

[27] J. Y. Shin, K. Pi, S. Jung, and D.-I. D. Cho, “Silicon-nanowire field-effect transistors on a flexible substrate using top-down MEMS processes,” in *IEEE MEMS*, 2016, vol. 5, no. January, pp. 469–472.

[28] N. Han, Z. X. Yang, F. Wang, G. Dong, S. Yip, X. Liang, T. F. Hung, Y. Chen, and J. C. Ho, “High-performance GaAs nanowire solar cells for flexible and transparent photovoltaics,” *ACS Appl. Mater. Interfaces*, vol. 7, no. 36, pp. 20454–20459, 2015.

[29] J. M. Spurgeon, S. W. Boettcher, M. D. Kelzenberg, B. S. Brunschwig, H. a. Atwater, and N.

S. Lewis, “Flexible, polymer-supported, si wire array photoelectrodes,” *Adv. Mater.*, vol. 22, no. 30, pp. 3277–3281, 2010.

[30] M. K. Kim, D. K. Yi, and U. Paik, “Tunable, flexible antireflection layer of ZnO nanowires embedded in PDMS,” *Langmuir*, vol. 26, no. 10, pp. 7552–7554, 2010.

[31] E. Garnett and P. Yang, “Light trapping in silicon nanowire solar cells.,” *Nano Lett.*, vol. 10, no. 3, pp. 1082–7, Mar. 2010.

[32] A. Tamang, M. Pathirane, R. Parsons, M. M. Schwarz, B. Iheanacho, V. Jovanov, V. Wagner, W. S. Wong, and D. Knipp, “Zinc oxide nanowire arrays for silicon core/shell solar cells,” *Opt. Express*, vol. 22, no. S3, p. A622, Mar. 2014.

[33] M. Pathirane, B. Iheanacho, A. Tamang, C.-H. Lee, R. Lujan, D. Knipp, and W. S. Wong, “Hybrid ZnO nanowire/a-Si:H thin-film radial junction solar cells using nanoparticle front contacts,” *Appl. Phys. Lett.*, vol. 107, no. 14, pp. 1–5, 2015.

[34] P. K. Mohseni, G. Lawson, C. Couteau, G. Weihs, A. Adronov, and R. R. LaPierre, “Growth and characterization of GaAs nanowires on carbon nanotube composite films: toward flexible nanodevices.,” *Nano Lett.*, vol. 8, no. 11, pp. 4075–80, Nov. 2008.

[35] Y. Wang, X. Zhang, P. Gao, Z. Shao, X. Zhang, Y. Han, and J. Jie, “Air heating approach for multilayer etching and roll-to-roll transfer of silicon nanowire arrays as SERS substrates for high sensitivity molecule detection,” *ACS Appl. Mater. Interfaces*, vol. 6, no. 2, pp. 977–984, 2014.

[36] D. B. Turner-Evans, H. Emmer, C. T. Chen, and H. A. Atwater, “Flexible, transparent contacts for inorganic nanostructures and thin films,” *Adv. Mater.*, vol. 25, no. 29, pp. 4018–4022, 2013.

[37] S. Zhang, Y. Shen, H. Fang, S. Xu, J. Song, and Z. L. Wang, “Growth and replication of ordered ZnO nanowire arrays on general flexible substrates,” *J. Mater. Chem.*, vol. 20, no. 47, p. 10606, 2010.

[38] K. E. Plass, M. a. Filler, J. M. Spurgeon, B. M. Kayes, S. Maldonado, B. S. Brunschwig, H. a. Atwater, and N. S. Lewis, “Flexible Polymer-Embedded Si Wire Arrays,” *Adv. Mater.*, vol. 21, no. 3, pp. 325–328, Jan. 2009.

[39] M. M. Adachi and K. S. Karim, “Fabrication of PECVD grown n-i-p silicon nanowire solar cells,” *2010 35th IEEE Photovolt. Spec. Conf.*, pp. 003302–003305, Jun. 2010.

[40] A. J. Standing, S. Assali, J. E. M. Haverkort, and E. P. A. M. Bakkers, “High yield transfer of ordered nanowire arrays into transparent flexible polymer films.,” *Nanotechnology*, vol. 23, no. 49, p. 495305, 2012.

[41] X. Xie, X. Zeng, P. Yang, H. Li, J. Li, X. Zhang, and Q. Wang, “Radial n-i-p structure SiNW-based microcrystalline silicon thin-film solar cells on flexible stainless steel.,” *Nanoscale Res. Lett.*, vol. 7, no. 1, p. 621, Jan. 2012.

[42] X. Xie, X. Zeng, P. Yang, H. Li, J. Li, X. Zhang, and Q. Wang, “Radial n-i-p structure silicon nanowire-based solar cells on flexible stainless steel substrates,” *Phys. Status Solidi Appl. Mater. Sci.*, vol. 210, no. 2, pp. 341–344, 2013.

[43] W. Spear and P. LeComber, “No Title,” *Solid State Comm.*, vol. 17, pp. 1193–1196, 1975.

[44] U.S. Department of Energy, “Energy Basics,” *Energy Efficiency and Renewable Energy*, 2013. [Online]. Available: http://www.eere.energy.gov/basics/renewable_energy/types_silicon.html.

[45] R. A. Street, W. S. Wong, and R. Lujan, “Low-temperature amorphous silicon p-i-n photodiodes,” *Phys. Status Solidi*, vol. 246, no. 8, pp. 1854–1857, Aug. 2009.

[46] R. A. Street, P. Qi, R. Lujan, and W. S. Wong, “Reflectivity of disordered silicon nanowires,” *Appl. Phys. Lett.*, vol. 93, no. 16, pp. 1–3, 2008.

[47] O. Gunawan and K. Wang, “High performance wire-array silicon solar cells,” *Prog. Photovolt Res. Appl.*, vol. 19, no. August 2010, pp. 307–312, 2011.

[48] O. Gunawan and S. Guha, “Characteristics of vapor–liquid–solid grown silicon nanowire solar cells,” *Sol. Energy Mater. Sol. Cells*, vol. 93, no. 8, pp. 1388–1393, Aug. 2009.

[49] L. Yu, B. O’Donnell, M. Foldyna, and P. Roca i Cabarrocas, “Radial junction amorphous silicon solar cells on PECVD-grown silicon nanowires,” *Nanotechnology*, vol. 23, no. 19, p. 194011, 2012.

[50] C. Chen, R. Jia, H. Yue, H. Li, X. Liu, D. Wu, W. Ding, T. Ye, S. Kasai, H. Tamotsu, J. Chu, and S. Wang, “Silicon nanowire-array-textured solar cells for photovoltaic application,” *J. Appl. Phys.*, vol. 108, no. 9, p. 094318, 2010.

[51] C. L. Cheung, R. J. Nikolić, C. E. Reinhardt, and T. F. Wang, “Fabrication of nanopillars by nanosphere lithography,” *Nanotechnology*, vol. 17, no. 5, pp. 1339–1343, Mar. 2006.

[52] J. Zhu, Y. Xu, Q. Wang, and Y. Cui, “Amorphous silicon core-shell nanowire solar cells,” in *Proceedings of the 35th Photovoltaic Specialist Conference*, 2010, pp. 2–5.

[53] J.-Y. Jung, Z. Guo, S.-W. Jee, H.-D. Um, K.-T. Park, and J.-H. Lee, “A strong antireflective solar cell prepared by tapering silicon nanowires.,” *Opt. Express*, vol. 18 Suppl 3, no. May, pp. A286–92, Sep. 2010.

[54] M. Khorasaninejad, N. Abedzadeh, A. Singh Jawanda, N. O, M. P. Anantram, and S. Singh Saini, “Bunching characteristics of silicon nanowire arrays,” *J. Appl. Phys.*, vol. 111, no. 4, p. 044328, 2012.

[55] L. He, C. Jiang, H. Wang, D. Lai, Y. Heng Tan, and C. Seng Tan, “Effects of nanowire texturing on the performance of Si/organic hybrid solar cells fabricated with a 2.2 μm thin-film Si absorber,” *Appl. Phys. Lett.*, vol. 100, no. 10, p. 103104, 2012.

[56] H. Bao and X. Ruan, “Optical absorption enhancement in disordered vertical silicon nanowire arrays for photovoltaic applications.,” *Opt. Lett.*, vol. 35, no. 20, pp. 3378–80, Oct. 2010.

[57] B. O’Donnell, L. Yu, M. Foldyna, and P. Roca I Cabarrocas, “Silicon nanowire solar cells grown by PECVD,” *J. Non. Cryst. Solids*, vol. 358, no. 17, pp. 2299–2302, 2012.

[58] J. Cho, B. O. Donnell, L. Yu, K. Kim, I. Ngo, and P. R. Cabarrocas, “Sn-catalyzed silicon nanowire solar cells with 4 . 9 % efficiency grown on glass,” *Prog. Photovolt Res. Appl.*, vol. 21, pp. 77–81, 2013.

[59] M. D. Kelzenberg, D. B. Turner-Evans, M. C. Putnam, S. W. Boettcher, R. M. Briggs, J. Y. Baek, N. S. Lewis, and H. A. Atwater, “High-performance Si microwire photovoltaics,” *Energy Environ. Sci.*, vol. 4, no. 3, p. 866, 2011.

[60] M. Pathirane, H. K. Hosseinzadeh, I. A. Goldthorpe, and W. S. Wong, “Transparent and Conformal Electrodes on 3-Dimensional Nanowire Solar Cells,” 2015.

[61] J. Allen, E. Hemesath, D. Perea, J. Lensch-Falk, Z. Li, F. Yin, M. Gass, P. Wang, A. Bleloch, R. Palmer, and L. Lauhon, “High-resolution detection of Au catalyst atoms in Si nanowires,” *Nat. Nanotechnol.*, vol. 3, pp. 168 – 173, 2008.

[62] E. Fathi and A. Sazonov, “Protocrystalline silicon solar cells on transparent plastic substrates,” *2009 34th IEEE Photovolt. Spec. Conf.*, pp. 001785–001788, Jun. 2009.

[63] L. Dupré, D. Buttard, C. Leclere, H. Renevier, and P. Gentile, “Gold Contamination in VLS-Grown Si Nanowires: Multiwavelength Anomalous Diffraction Investigations,” *Chem. Mater.*, vol. 24, no. 23, pp. 4511–4516, Dec. 2012.

[64] J. B. Hannon, S. Kodambaka, F. M. Ross, and R. M. Tromp, “The influence of the surface migration of gold on the growth of silicon nanowires.,” *Nature*, vol. 440, no. 7080, pp. 69–71, Mar. 2006.

[65] B. M. Kayes, M. A. Filler, M. C. Putnam, M. D. Kelzenberg, N. S. Lewis, and H. A. Atwater, “Growth of vertically aligned Si wire arrays over large areas (>1 cm2) with Au and Cu catalysts,” *Appl. Phys. Lett.*, vol. 91, no. 10, pp. 1–4, 2007.

[66] G. Bemski, “Recombination Properties of Gold in Silicon,” *Phys. Rev. B*, vol. 111, no. 6, pp. 1515–1518, 1958.

[67] J. Oh, H.-C. Yuan, and H. M. Branz, “An 18.2%-efficient black-silicon solar cell achieved through control of carrier recombination in nanostructures,” *Nat. Nanotechnol.*, vol. 7, no. September, pp. 2–5, 2012.

[68] Y. Kuang, K. H. M. van der Werf, Z. S. Houweling, and R. E. I. Schropp, “Nanorod solar cell with an ultrathin a-Si:H absorber layer,” *Appl. Phys. Lett.*, vol. 98, no. 11, p. 113111, 2011.

[69] H. H. Li, P.-Y. Yang, S.-M. Chiou, H.-W. Liu, and H.-C. Cheng, “A Novel Coaxial-Structured Amorphous-Silicon p-i-n Solar Cell With Al-Doped ZnO Nanowires,” *IEEE Electron Device Lett.*, vol. 32, no. 7, pp. 928–930, 2011.

[70] C. I. Ho, W. C. Liang, D. J. Yeh, V. C. Su, P. C. Yang, S. Y. Chen, T. T. Yang, J. H. Lee, C. H. Kuan, I. C. Cheng, and S. C. Lee, “Influence of the absorber layer thickness and rod length on the performance of three-dimensional nanorods thin film hydrogenated amorphous silicon solar cells,” *J. Appl. Phys.*, vol. 113, no. 16, pp. 0–4, 2013.

[71] Y. Kuang, K. H. M. Van Der Werf, Z. S. Houweling, M. Di Vece, and R. E. I. Schropp, “Fabrication and characterization of nanorod solar cells with an ultrathin a-Si:H absorber layer,” *J. Non. Cryst. Solids*, vol. 358, no. 17, pp. 2209–2213, 2012.

[72] R. Dewan, J. I. Owen, D. Madzharov, V. Jovanov, J. Hüpkes, and D. Knipp, “Analyzing nanotextured transparent conductive oxides for efficient light trapping in silicon thin film solar cells,” *Appl. Phys. Lett.*, vol. 101, no. 10, p. 103903, 2012.

[73] R. Dewan, I. Vasilev, V. Jovanov, and D. Knipp, “Optical enhancement and losses of pyramid textured thin-film silicon solar cells,” *J. Appl. Phys.*, vol. 110, no. 1, p. 013101, 2011.

[74] C. Haase, U. Rau, and H. Stiebig, “Efficient light trapping scheme by periodic and quasi-random light trapping structures,” in *33rd IEEE Photovoltaic Specialists Conference*, 2008, pp. 697–701.

[75] C. Lin and M. L. Povinelli, “Optimal design of aperiodic, vertical silicon nanowire structures for photovoltaics.,” *Opt. Express*, vol. 19 Suppl 5, no. May, pp. A1148–54, Sep. 2011.

[76] L. E. Greene, M. Law, D. H. Tan, M. Montano, J. Goldberger, G. Somorjai, and P. Yang, “General route to vertical ZnO nanowire arrays using textured ZnO seeds.,” *Nano Lett.*, vol. 5, no. 7, pp. 1231–6, Jul. 2005.

[77] L. E. Greene, B. D. Yuhas, M. Law, D. Zitoun, and P. Yang, “Solution-grown zinc oxide nanowires.,” *Inorg. Chem.*, vol. 45, no. 19, pp. 7535–43, Sep. 2006.

[78] L. Vayssieres, K. Keis, A. Hagfeldt, and S.-E. Lindquist, “Three-Dimensional Array of Highly Oriented Crystalline ZnO Microtubes,” *Chem. Mater.*, vol. 13, no. 12, pp. 4395–4398, Dec. 2001.

[79] L. E. Greene, M. Law, J. Goldberger, F. Kim, J. C. Johnson, Y. Zhang, R. J. Saykally, and P. Yang, “Low-temperature wafer-scale production of ZnO nanowire arrays.,” *Angew. Chem. Int. Ed. Engl.*, vol. 42, no. 26, pp. 3031–4, Jul. 2003.

[80] S. Baruah and J. Dutta, “Effect of seeded substrates on hydrothermally grown ZnO nanorods,” *J. Sol-Gel Sci. Technol.*, vol. 50, no. 3, pp. 456–464, Feb. 2009.

[81] L. Vayssieres, “Designing ordered nanoarrays from aqueous solutions,” *Pure Appl. Chem.*, vol. 78, no. 9, pp. 1741–1747, 2006.

[82] E. Hosono, S. Fujihara, I. Honma, and H. Zhou, “The Fabrication of an Upright-Standing Zinc Oxide Nanosheet for Use in Dye-Sensitized Solar Cells,” *Adv. Mater.*, vol. 17, no. 17, pp. 2091–2094, Sep. 2005.

[83] G. D. Yuan, W. J. Zhang, J. S. Jie, X. Fan, J. a Zapien, Y. H. Leung, L. B. Luo, P. F. Wang, C. S. Lee, and S. T. Lee, “p-Type ZnO nanowire arrays.,” *Nano Lett.*, vol. 8, no. 8, pp. 2591–7, Aug. 2008.

[84] S. Yamabi and H. Imai, “Growth conditions for wurtzite zinc oxide films in aqueous solutions,” *J. Mater. Chem.*, vol. 12, no. 12, pp. 3773–3778, Nov. 2002.

[85] C. Hsieh, “Spherical Zinc Oxide Nano Particles from Zinc Acetate in the Precipitation Method,” no. 4, pp. 31–34, 2007.

[86] T. Ma, M. Guo, M. Zhang, Y. Zhang, and X. Wang, “Density-controlled hydrothermal growth of well-aligned ZnO nanorod arrays.,” *Nanotechnology*, vol. 18, no. 3, p. 035605, Jan. 2007.

[87] L. Vayssieres, K. Keis, S. Lindquist, and A. Hagfeldt, “Purpose-Built Anisotropic Metal Oxide Material : 3D Highly Oriented Microrod Array of ZnO,” vol. 28, pp. 3350–3352, 2001.

[88] Corning, “Eagle 2000 Material Information,” *Mater. Inf.*, no. April, 2005.

[89] K. M. McPeak, T. P. Le, N. G. Britton, Z. S. Nickolov, Y. a Elabd, and J. B. Baxter, “Chemical bath deposition of ZnO nanowires at near-neutral pH conditions without hexamethylenetetramine (HMTA): understanding the role of HMTA in ZnO nanowire growth.,” *Langmuir*, vol. 27, no. 7, pp. 3672–7, Apr. 2011.

[90] H. Strauven, a. Stesmans, J. Winters, J. Spinnewijn, and O. B. Verbeke, “a-Si:H prepared by ion bombardment activated hydrogen incorporation during Si evaporation,” *J. Appl. Phys.*, vol. 62, no. 7, p. 2836, 1987.

[91] R. E. I. Schropp and M. Zeman, *Amorphous and Microcrystalline Silicon Solar Cells:*

Modeling, Materials and Device Technology. Kluwer Academic Publishers, 1998.

[92] H. K. Kim, D. G. Kim, K. S. Lee, M. S. Huh, S. H. Jeong, K. I. Kim, and T. Y. Seong, "Plasma damage-free sputtering of indium tin oxide cathode layers for top-emitting organic light-emitting diodes," *Appl. Phys. Lett.*, vol. 86, no. 18, pp. 1–3, 2005.

[93] L. Li, Y. Zhang, and Z. Chew, "A Cu / ZnO Nanowire / Cu Resistive Switching Device," *Nano-Micro Lett.*, vol. 3, no. 5, pp. 159–162, 2013.

[94] R. A. Street, *Hydrogenated Amorphous Silicon*. 2005.

[95] J. Y. Lee, S. T. Connor, Y. Cui, and P. Peumans, "Solution-processed metal nanowire mesh transparent electrodes," *Nano Lett.*, vol. 8, no. 2, pp. 689–692, 2008.

[96] J. Van De Groep, P. Spinelli, and A. Polman, "Transparent conducting silver nanowire networks," *Nano Lett.*, vol. 12, no. 6, pp. 3138–3144, 2012.

[97] E. C. Garnett, W. Cai, J. J. Cha, F. Mahmood, S. T. Connor, M. Greyson Christoforo, Y. Cui, M. D. McGehee, and M. L. Brongersma, "Self-limited plasmonic welding of silver nanowire junctions," *Nat. Mater.*, vol. 11, no. 3, pp. 241–249, 2012.

[98] F. Xu and Y. Zhu, "Highly conductive and stretchable silver nanowire conductors," *Adv. Mater.*, vol. 24, no. 37, pp. 5117–5122, 2012.

[99] H. Lu, D. Zhang, X. Ren, J. Liu, W. C. H. Choy, and L. U. E. T. Al, "Selective Growth and Integration of Silver Nanoparticles on Silver Nanowires at Room Conditions for Transparent Nano-Network Electrode," *ACS Nano*, vol. 8, no. 10, pp. 10980–10987, 2014.

[100] S. Nam, M. Song, D.-H. Kim, B. Cho, H. M. Lee, J.-D. Kwon, S.-G. Park, K.-S. Nam, Y. Jeong, S.-H. Kwon, Y. C. Park, S.-H. Jin, J.-W. Kang, S. Jo, and C. S. Kim, "Ultrasmooth, extremely deformable and shape recoverable Ag nanowire embedded transparent electrode.," *Sci. Rep.*, vol. 4, p. 4788, 2014.

[101] C. H. Chung, T. Bin Song, B. Bob, R. Zhu, H. S. Duan, and Y. Yang, "Silver nanowire composite window layers for fully solution-deposited thin-film photovoltaic devices," *Adv. Mater.*, vol. 24, no. 40, pp. 5499–5504, 2012.

[102] L. Yang, X. Yu, W. Hu, X. Wu, Y. Zhao, and D. Yang, "An 8.68% Efficiency Chemically-Doped-Free Graphene–Silicon Solar Cell Using Silver Nanowires Network Buried Contacts," *ACS Appl. Mater. Interfaces*, p. 150210153736004, 2015.

[103] B. Dan, G. C. Irvin, and M. Pasquali, "Continuous and Scalable Fabrication of Nanotube Films," *ACS Nano*, vol. 3, no. 4, pp. 835–843, 2009.

[104] X. Yu, R. Rajamani, K. a Stelson, and T. Cui, "Carbon nanotube based transparent conductive thin films.," *J. Nanosci. Nanotechnol.*, vol. 6, no. 7, pp. 1939–1944, 2006.

[105] C.-H. Liu and X. Yu, "Silver nanowire-based transparent, flexible, and conductive thin film.," *Nanoscale Res. Lett.*, vol. 6, no. 1, p. 75, 2011.

[106] S. De, T. M. Higgins, P. E. Lyons, E. M. Doherty, P. N. Nirmalraj, W. J. Blau, J. J. Boland, and J. N. Coleman, "Silver Nanowire Networks as Flexible,Transparent, Conducting Films: Extremely High DC to Optical Conductivity Ratios," *ACS Nano*, vol. 3, no. 7, pp. 1767–1774, 2009.

[107] H. H. Khaligh and I. a Goldthorpe, "Failure of silver nanowire transparent electrodes under

current flow.," *Nanoscale Res. Lett.*, vol. 8, no. 1, p. 235, 2013.

[108] E. Marzbanrad, G. Rivers, P. Peng, B. Zhao, and N. Y. Zhou, "How morphology and surface crystal texture affect thermal stability of a metallic nanoparticle: the case of silver nanobelts and pentagonal silver nanowires," *Phys. Chem. Chem. Phys.*, vol. 17, no. 1, pp. 315–324, 2015.

[109] H. Gleskova, I. C. Cheng, S. Wagner, J. C. Sturm, and Z. Suo, "Mechanics of thin-film transistors and solar cells on flexible substrates," *Sol. Energy*, vol. 80, no. 6, pp. 687–693, 2006.

[110] W. S. Wong and A. Salleo, *Flexible Electronics Materials and Applications*. 2009.

[111] M. Ohring, *The Materials Science of Thin Films*, vol. 1. 1992.

[112] S. Kumar Selvaraja, M. Schaekers, W. Bogaerts, and D. Van Thourhout, "Deposited amorphous silicon-on-insulator technology for nano-photonic integrated circuits," *Opt. Commun.*, vol. 313, pp. 210–216, 2014.

[113] S. K. Park, J. I. Han, D. G. Moon, and W. K. Kim, "Mechanical stability of externally deformed indium-tin-oxide films on polymer substrates," *Japanese J. Appl. Physics, Part 1 Regul. Pap. Short Notes Rev. Pap.*, vol. 42, no. 2 A, pp. 623–629, 2003.

[114] J. Lewis, "Material challenge for flexible organic devices," *Mater. Today*, vol. 9, no. 4, pp. 38–45, 2006.

[115] M. Pathirane and W. S. Wong, "Optical and Electrical Characteristics of Radial Junction Nanowire Solar Cells under Applied Mechanical Bending," 2015.

[116] Y. Zhu, Q. Qin, F. Xu, F. Fan, Y. Ding, T. Zhang, B. J. Wiley, and Z. L. Wang, "Size effects on elasticity, yielding, and fracture of silver nanowires: In situ experiments," *Phys. Rev. B - Condens. Matter Mater. Phys.*, vol. 85, no. 4, pp. 1–7, 2012.

[117] T. N. Ng, W. S. Wong, M. L. Chabinyc, S. Sambandan, and R. A. Street, "Flexible image sensor array with bulk heterojunction organic photodiode," *Appl. Phys. Lett.*, vol. 92, no. 21, p. 213303, 2008.

[118] M. J. Chow, A. A. Fomani, M. Moradi, G. Chaji, R. A. Lujan, and W. S. Wong, "Effects of mechanical strain on amorphous silicon thin-film transistor electrical stability," *Appl. Phys. Lett.*, vol. 102, no. 23, p. 233509, 2013.

[119] N. Anttu, A. Abrand, D. Asoli, M. Heurlin, I. ??berg, L. Samuelson, and M. Borgstr??m, "Absorption of light in InP nanowire arrays," *Nano Res.*, vol. 7, no. 6, pp. 816–823, 2014.

[120] M. Sun, C. Luo, L. Xu, H. Ji, Q. Ouyang, D. Yu, and Y. Chen, "Artificial lotus leaf by nanocasting," *Langmuir*, vol. 21, no. 19, pp. 8978–8981, 2005.

[121] J. M. K. Ng, A. D. Stroock, and G. M. Whitesides, "Components for integrated poly (dimethylsiloxane) microfluidic systems," pp. 3461–3473, 2010.

[122] M.-C. Lim, M.-H. Lee, K.-B. Kim, T.-J. Jeon, and Y.-R. Kim, "A Mask-Free Passivation Process for Low Noise Nanopore Devices," *J. Nanosci. Nanotechnol.*, vol. 15, no. 8, pp. 5971–5977, 2015.

[123] M. Ma and R. M. Hill, "Superhydrophobic surfaces," *Curr. Opin. Colloid Interface Sci.*, vol. 11, no. 4, pp. 193–202, 2006.

[124] J. Genzer and A. Marmur, “B iological and Synthetic Self- Cleaning Surfaces,” *MRS Bull.*, vol. 33, no. August, pp. 742–746, 2008.

[125] T. Ma, B. Bhushan, H. Murooka, I. Kobayashi, and T. Osawa, “A novel technique to measure the Poisson’s ratio and submicron lateral dimensional changes of ultrathin polymeric films,” *Rev. Sci. Instrum.*, vol. 73, no. 4, p. 1813, 2002.

[126] P. Information, “Corning ® Thin Sheet Glass Products,” no. mm.

[127] “Material Property Database: PDMS,” *MIT*. [Online]. Available: http://www.mit.edu/~6.777/matprops/pdms.htm.